Magnet Characterization and Beam Profile Monitor Development for a Spectrometer at the ARES Linac

von
Sonja Meike Jaster-Merz
aus Hamburg

Master-Arbeit im Studiengang Physik
Universität Hamburg
2019

1. Gutachter: Prof. Dr. Wolfgang Hillert
2. Gutachter: Dr. Florian Burkart

Abstract

The aim for size and cost reduction of particle accelerators has generated great interest in the development of novel acceleration techniques beyond the current radio frequency based technology. Those techniques are, for example, dielectric laser accelerators (DLAs) and have the potential to reduce the size and costs, due to their high field gradients and small acceleration periods. DLAs consist of structures which are characterized by apertures in the μm range, leading to electron-bunch charges in the pC range. At the SINBAD (Short and INnovative Bunches and Accelerators at DESY) facility at DESY, various techniques are foreseen to be investigated using the ARES (Accelerator Research Experiment at SINBAD) linear accelerator. To prove that an energy gain was achieved with these techniques, the electron energy needs to be measured downstream of the novel acceleration structures. This is done using a spectrometer, consisting of a dipole magnet and a beam profile monitor. Based on the accelerator design, electron beam parameters and operational mode, the spectrometer components need to fulfil various requirements. The dipole current, for example, needs to be adjustable to different electron beam energies with a reproducible and sufficient field quality. The beam profile monitor needs to be able to detect charge densities below 1.2 aC per μm^2 with a spatial resolution in the 100 μm range.

In the frame of this work, two dipoles were measured, their suitability for the spectrometer discussed, and a dipole for installation at ARES was chosen. The requirements on the beam profile monitor are challenging to fulfil with conventional screens, due to the expected low-charge densities. Therefore, a dedicated detector called STRIDENAS (STRIp DEtector for Novel Accelerators at SINBAD), able to resolve these low-charge beam densities, has been developed and is presented in this work. This project was realised as an internal DESY collaboration, combining the resources and expertise of the MPY-1 and FH-ATLAS groups, various manufacturing groups, as well as the detector development group of the University of Hamburg. The design, development and tests of different components like the sensors or readout electronics, and the commissioning of a detector prototype, are presented. This includes the characterization of several sensors, as well as an estimation of the produced charge in the sensor and its spatial resolution based on simulations, which was found to fulfil the requirements. The detector components were tested individually at the DESY II Test Beam with a low electron intensity. Tests of the readout electronics, as well as tests of the sensor with an additional amplifier, were performed, and the results are presented and discussed in this work.

Zusammenfassung

Das Vorhaben, die Größe und Kosten konventioneller, radio-frequenz-basierter Beschleuniger zu reduzieren, hat das Interesse an der Entwicklung neuartiger Beschleunigertechnologien geweckt. Sie haben das Potential, aufgrund von hohen Feldgradienten und kleinen Beschleunigerperioden im Vergleich zu konventionellen Beschleunigern das Ziel zu erreichen und sind Bestandteil der Beschleuniger-Forschung und -Entwicklung. Zu diesen neuartigen Beschleunigern zählen z.B. Laser-Plasma-Beschleuniger oder Dielektische Laser-Beschleuniger. Letztere bestehen aus Strukturen die durch Aperturen im µm-Bereich gekennzeichnet sind, was Elektronenstrahlen mit Ladungen im pC-Bereich zur Folge hat. In der SINBAD (Short and INnovative Bunches and Accelerators at DESY) Einrichtung am DESY sollen solche Techniken mit Hilfe des ARES (Accelerator Research Experiment at SINBAD) Elektronen-Linearbeschleunigers untersucht und ein Energiegewinn demonstriert werden. Dafür ist die Energiemessung der Elektronen nach dem Durchqueren der neuartigen Beschleunigerstrukturen notwendig. Bei ARES soll dies mit einem Spektrometer, bestehend aus einem Dipol und einem Strahlprofilmonitor, durchgeführt werden. Basierend auf dem Beschleunigerlayout, den Elektronenstrahlparametern und unterschiedlichen Betriebsmodi, werden verschiedene Ansprüche an die Spektrometerkomponenten gestellt. So muss z.B. der Dipolstrom reproduzierbar mit einer ausreichenden resultierenden Feldqualität an die jeweilige Elektronenstrahlenergie angepasst werden können. Der Strahlprofilmonitor muss in der Lage sein, Elektronenverteilungen mit Ladungsdichten unterhalb von 1.2 aC pro μm^2 mit einer örtlichen Auflösung im 100 µm Bereich zu messen.

Im Rahmen dieser Arbeit wurden zwei Dipole vermessen, ihre Eignung für das Spektrometer diskutiert und ein Dipol zum Einbau bei ARES ausgewählt. Aufgrund der geringen Strahlladungen ist es eine Herausforderung, die Anforderungen an den Strahlprofilmonitor mit konventionellen Schirmen zu erfüllen. In dieser Arbeit wird daher ein hierfür speziell entwickelter Detektor namens STRIDENAS (STRIp DEtector for Novel Accelerators at SINBAD) vorgestellt, der die Messung dieser Strahlen mit ausreichender räumlicher Auflösung ermöglichen soll. Das Projekt wurde als interne DESY Kollaboration zwischen den MPY-1 und FH-ATLAS Gruppen realisiert und vereint die Ressourcen und Kompetenzen dieser, sowie der Detektor Gruppe der Universität Hamburg und Fertigungsgruppen am DESY. Das Design, die Entwicklung, die Tests verschiedener Komponenten, wie der Sensoren und der Ausleseelektronik, und die Inbetriebnahme eines Prototypen werden vorgestellt. Hierzu gehört die Charakterisierung der verwendeten Sensoren sowie die Abschätzung der produzierten Ladung und der örtlichen Auflösung, basierend auf Simulationen, welche die Anforderungen erfüllen. Die Detektorkomponenten wurden einzeln am DESY II Test Beam unter niedriger Elektronenintensität getestet. Tests der Ausleseelektronik sowie eines Sensors mit Verstärker wurden durchgeführt, und die Ergebnisse werden in dieser Arbeit diskutiert.

Contents

Chapter 1

Introduction

Particle accelerators are key tools for scientific research and have a wide range of industrial and medical applications [1]. They are, however, typically big and expensive particularly in the fields of particle physics or photon science [2,3], which limits their availability and applications. Therefore, strong interest of accelerator research lies in the development of novel acceleration concepts such as plasma acceleration or dielectric laser acceleration (DLA), which promise a significant reduction in the size and cost with respect to conventional radio frequency based technology.

At DESY, accelerator research and development is done for example at the SINBAD (Short and INnovative Bunches and Accelerators at DESY) facility. It hosts the ARES (Accelerator Research Experiment at SINBAD) linear accelerator, which is currently under commissioning and has been designed to produce ultrashort bunches with fs to sub-fs duration for a variety of applications, including injection into novel accelerators. In order to measure the beam energy at ARES and to determine the performance of the novel acceleration techniques under study, a spectrometer is needed. This device consists of a dipole magnet, which needs to fulfil certain conditions on the field strength and quality, and a beam profile monitor with sufficient sensitivity to spatially resolve the beam. This is a critical point for certain acceleration setups such as DLAs, where the produced beams typically feature a low, sub-pC charge and are therefore challenging to measure with conventional techniques used in multi-pC accelerators.

To overcome this challenge, the development of a dedicated detector setup called STRIDENAS (STRIp DEtector for Novel Accelerators at SINBAD), able to resolve these low-charge beams, is presented in this work. The STRIDENAS project was realised as an internal DESY collaboration, combining the resources and expertise of the MPY-1 and FH-ATLAS groups, various manufacturing groups, as well as the detector development group of the University of Hamburg. The implemented sensors have been characterized, the detector setup has been designed, and functionality tests with the readout system have been performed. Possible challenges due to the high electron rate compared to the usual applications of these type of sensors are discussed and explored limits are presented. Steps to an implementation in the beamline are discussed. In addition, characterization measurements of magnet candidates for the spectrome-

ter dipole were performed and the data analysed.

This thesis consists of a theoretical background on spectrometers and silicon detectors. It is followed by an overview of the SINBAD facility and a chapter on the measurements of the spectrometer dipoles. The following chapters focus on the STRIDENAS detector with one chapter describing the design of the device, the sensor property measurements and one chapter focussing on the measurements performed at the DESY II Test Beam facility. Finally a conclusion on the spectrometer dipole as well as a conclusion and an outlook on the STRIDENAS detector is presented.

Chapter 2

Theoretical Background

As previously mentioned, the work of this thesis is structured in two main parts: the characterization of dipole magnets for a spectrometer and the development of a beam profile monitor based on silicon strip sensors. In this chapter, the underlying theoretical background of the physics of beam energy spectrum measurements as well as the physics of silicon strip sensors is presented.

2.1 Physics of Beam Energy Spectrum Measurements

The energy and energy spread of particle distributions produced in accelerators are of key interest when the beams are used for applications like colliders, free-electron lasers or research and development. These quantities can be measured with the help of a spectrometer setup. Various designs for spectrometers using different beam optics exist and are for example discussed in more detail in [4]. For this work, the design described in Section 3 consists of one dipole, four quadrupoles for optics matching, and a beam profile monitor placed downstream of the magnet.

2.1.1 Spectrometer

In a spectrometer, particles are bent in a dipole with a bending angle according to their momentum, resulting in a spatial separation. The induced separation between these particles can be measured on a calibrated screen in order to determine their energy. In the following, the underlying physics of this process is explained in more detail.

The trajectory of charged particles can be changed by electric and magnetic fields through the Lorentz force [5]

$$\boldsymbol{F}_L = q(\boldsymbol{E} + \boldsymbol{v} \times \boldsymbol{B}), \tag{2.1}$$

where q is the particle charge, $\boldsymbol{E}$ the electric field, $\boldsymbol{v}$ the particle velocity and $\boldsymbol{B}$ the magnetic field.

In the following, a coordinate system with an orientation as shown in Figure 2.1 is used. The direction of the reference particle trajectory is called s with x and y perpendicular to it.

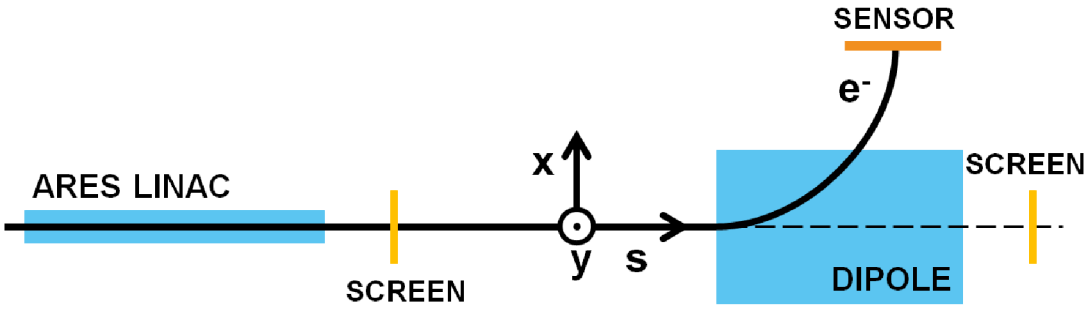

Figure 2.1: Orientation of the coordinate system with respect to the ARES spectrometer layout.

If an electron passes through a magnetic field, it is bent on a circular trajectory with a bending radius ρ. Assuming a particle velocity $\boldsymbol{v}$ perpendicular to the magnetic field $\boldsymbol{B}$, this leads to

$$|B\rho| = \frac{p}{e}, \tag{2.2}$$

where p is the particle momentum, e the elementary charge and $|B\rho|$ is called the beam rigidity. The deflection angle $d\theta = \frac{ds}{\rho}$ for particles in the x-s plane after travelling a distance ds is then given by

$$d\theta(\boldsymbol{r}) = \frac{e}{p} B_y(\boldsymbol{r}) ds, \tag{2.3}$$

where B_y is the magnetic field component in y direction. The total bending angle θ of a finite section is obtained by integrating Equation 2.3 along the particle's path

$$\theta = \frac{e}{p} \int_{path} B_y(s) ds. \tag{2.4}$$

The deflecting magnetic field is created by a dipole. A dipole introduces a correlation between the momentum and the transverse position of the beam particles called dispersion. In a sector dipole (where the dipole edges are perpendicular to the particle trajectory) the dispersion is given by [5]

$$D(s) = \rho(1 - \cos\frac{L}{\rho}), \tag{2.5}$$

where ρ is the bending radius, L the dipole length and $\frac{L}{\rho}$ the bending angle θ. The transverse offset of a particle with momentum p with respect to a reference particle with momentum p_0 is then given by

$$x(s) = D(s) \cdot \frac{\Delta p}{p_0}, \tag{2.6}$$

with $\Delta p = p - p_0$.

The dispersion has therefore an impact on the beam size σ_x, which can be written as

$$\sigma_x = \sqrt{E_b(s)^2 + D(s)^2 \frac{\Delta p^2}{p_0^2}}, \tag{2.7}$$

and where two components can be identified. One component is given by the dispersion and appears whenever $D(s) \neq 0$ and $\Delta p \neq 0$. The other component is the beam envelope, defined as

$$E_b = \sqrt{\beta(s) \cdot \varepsilon}, \tag{2.8}$$

where $\beta(s)$ is the so-called beta function, which can be derived by solving the differential equation of motion of a particle in a beamline with only focussing fields (no dispersion) and is for example shown in [5] and [6]. $\beta(s)$ is a position-dependent function given by the focussing fields which, as seen in Equation 2.8, determines the beam envelope for a given emittance ε. In this case, ε corresponds to the root mean square (RMS) emittance defined as

$$\varepsilon = \sqrt{\langle x^2 \rangle \langle x'^2 \rangle - \langle x x' \rangle^2}. \tag{2.9}$$

This quantity is a measure for the area of the distribution in trace space $(x - x')$, where $x' = \frac{p_x}{p_z}$ and $\langle\ \rangle$ represents the second central moment of the particle distribution [7].

The resolution of the spectrometer depends on the ratio of the beam size without dispersive effects to the beam size with dispersive effects. In order to distinguish two beams with different energies, the separation on the screen has to be greater than their beam envelopes. Following [5], a factor of two times the beam envelope for the minimum required separation is assumed here. The separation on the screen is given by Equation 2.6. The dispersion at the screen is given by the induced dispersion due to the dipole and the drift. In a drift after a dipole the dispersion is given by

$$D(s) = \sin(\theta) \cdot s, \tag{2.10}$$

where θ is the total bending angle of the dipole.

To resolve two beams with different energies, the minimum relative beam energy difference has to be

$$\Delta E_{min} \geq \frac{2E_b}{D} = \frac{2\sqrt{\varepsilon\beta}}{D}. \tag{2.11}$$

Thus, for a good resolution ($\mathcal{O}(10^{-4}\ \Delta E_{\text{min}})$) at the screen position s_s, a large dispersion $D(s_s)$ and a small $\beta(s_s)$ is needed in order to minimize the ratio of $\frac{\sqrt{\beta}}{D}$.

Figure 2.1 shows a basic sketch of the ARES spectrometer layout. To measure ΔE, the angle of the incoming beam with respect to the magnet entrance must be well known in order to measure the energy correctly. At the ARES spectrometer this is achieved by a screen in front of the last matching quadrupole and a screen behind the dipole.

2.1.2 Magnet Specific Properties

The dipole magnets considered within this thesis are iron dominated electromagnets. The advantage compared to permanent magnets is the flexibility to adjust the magnet current and therefore allow different beam energies to go through a static beam pipe. The fields of these magnets

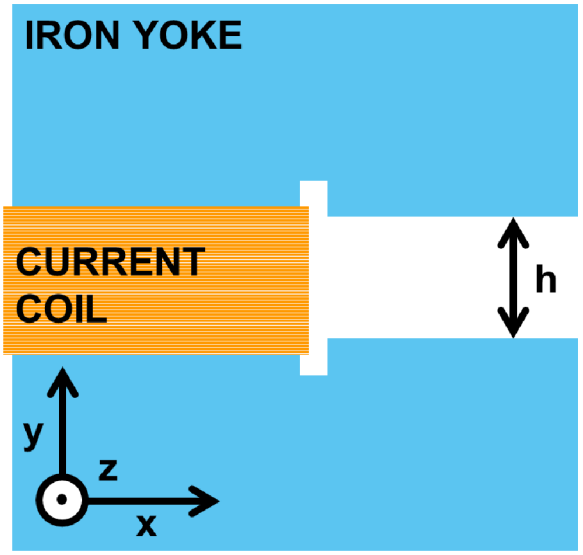

Figure 2.2: Sketch of a C-shaped dipole.

are determined by the shape of the ferromagnetic iron pole faces, as they form surfaces of constant magnetic potential [5].

Dipoles consist of two parallel iron poles which are separated by a gap of size h as indicated in Figure 2.2. The current coils are formed by windings around the iron yoke, which provides a return path for the magnetic flux. The magnetic field $\boldsymbol{B}$ of the dipole is created by current flowing through the coils and can be determined by Ampère's law [5] as

$$\nabla \times \frac{\boldsymbol{B}}{\mu_r} = \mu_0 \cdot \boldsymbol{J}, \tag{2.12}$$

where μ_r is the relative permeability, μ_0 the magnetic constant and $\boldsymbol{J}$ is the current density in the coils. Applying Stoke's theorem and integrating along a closed path in the dipole leads to

$$\oint_{\text{gap}} \frac{\boldsymbol{B}}{\mu_r^{\text{air}}} d\boldsymbol{s} + \oint_{\text{yoke}} \frac{\boldsymbol{B}}{\mu_r^{\text{iron}}} d\boldsymbol{s} = \mu_0 \cdot I_{\text{tot}}, \tag{2.13}$$

where μ_r^{air} and μ_r^{iron} are the relative permeabilities in air and iron respectively. Assuming an infinite relative permeability in the iron yoke this expression leads to

$$h \cdot B_0 = \mu_0 \cdot I_{\text{tot}}, \tag{2.14}$$

where B_0 is the magnetic field in the gap and I_{tot} is the total current. For a coil with n windings, the total current is given by $I_{\text{tot}} = n \cdot I$ with I being the current going through the coil. The magnetic field in the gap of a dipole is therefore given by

$$B_0 = \mu_0 \frac{n \cdot I}{h}. \tag{2.15}$$

In reality, deviations from this ideal homogeneous field arise, for example, due to the finite

magnet length or iron pole imperfections. This leads to non homogeneous magnetic fields and the appearance of so called fringe fields. Fringe fields occur beyond a certain distance from the magnet centre and are the smooth transition from the maximal field strength in the gap middle to zero field strength outside of the dipole [5]. Individually powered corrector coils on the iron yoke can be used to partially correct for these imperfections.

Another effect on the magnetic field for ferromagnets is saturation. For low field strengths below 1 T, the relation between the current and the magnetic field is linear as shown in Equation 2.15. However, above a certain value, the field no longer increases linearly with the current but lags behind [8]. This effect can be explained by looking at the magnetization of ferromagnetic material, in which a magnetic field is created by an externally applied magnetizing field. This external field aligns the electron spins in the material, which results in a net magnetic field. Once all spins are aligned, an increase of the magnetizing field no longer results in an increase of the magnetic field and hence the material saturates. If the external field is switched off, the material remains partially magnetized. This results in different magnetic field values depending on the direction of change of the applied current, an effect referred to as hysteresis. The material can however be demagnetized by applying a field in the opposite direction. Thus, to avoid hysteresis effects during magnet operation, the magnet needs to be cycled [9]. This is of particular importance at ARES since the beam should also be able to go straight through the dipole as indicated in Figure 2.1.

2.2 Physics of Silicon Strip Detectors

Silicon strip detectors are commonly used for particle tracking in high energy physics experiments like ATLAS [10] and CMS [11] at the Large Hadron Collider [2]. The designed STRIp DEtector for Novel Accelerators at SINBAD (STRIDENAS) presented in this thesis is using two silicon strip sensors, which were originally developed for ATLAS. The underlying physics of particle matter interaction, the working principle of a semiconductor sensor and the signal formation and behaviour based on the books Teilchendetektoren by Kolanoski and Wermes [12] and Semiconductor Detector Systems by Spieler [13] are presented in this section.

2.2.1 Silicon Properties

Silicon is a commonly used material for solid-state detectors and available in the form of wafers [13]. It is a semiconductor of atomic number 14 which crystallizes in a diamond lattice structure. In a lattice structure electron energy levels of single atoms overlap and form so-called energy bands. At 0 K, the outermost occupied band (called valence band) is completely filled whereas the next band (conduction band) is completely empty. The valence and conduction bands in silicon are separated by a bandgap of 1.12 eV at 300 K [13]. Above 0 K, lattice vibrations create phonon quanta which enable the excitation of valence electrons to the conduction band. The excited electrons leave vacant states (called holes) in the valance band behind. If an external electric field is applied, electrons and holes can move through the conduction and valence bands and contribute to the current. With rising temperature the lattice vibration and hence the electron excitation probability increases and therefore leads to a higher conductivity. Conductivity can also be increased by doping the material. Silicon has four valence electrons and can be doped by inserting atoms with either five valence electrons (n-type) or three valence electrons (p-type). This procedure introduces occupied states close to the conduction band and free states close to the valence band with an energy gap of around 0.045 eV. These states are easily excited at room temperature and contribute to the conductivity. Frequently used materials are phosphor or arsenic for n-type doping and boron or aluminium for p-type doping.

Silicon has a density of 2.33 g/cm^3, which is relatively high compared to gas detectors and enables a large energy loss of incoming particles in a short distance. Incoming particles deposit an energy E in the sensor, creating electron-hole pairs which can be read out as an electrical signal. The number of produced electron-hole pairs N depends on the deposited energy and the ionization energy E_{ion} of the material. For silicon, the ionization energy is E_{ion}^{Si} = 3.6 eV. The average number of produced signal quanta is then $N = E/E_{ion}$ with a statistical fluctuation of $\sigma_N = \sqrt{FN}$. The Fano factor F applies because, in addition to the charge signal, phonon excitation with smaller (meV) excitation energy occurs, which reduces the statistical fluctuations. The Fano factor is 0.1 for silicon and is explained in more detail in [13].

2.2.2 Interaction of Charged Particles with Silicon

The energy loss of charged particles when passing through matter can be described by the Bethe-Bloch formula. For particles with muon mass or greater, energy loss mainly occurs due to ionization and excitation. At high energies, radiation effects have to be taken into account. The mass stopping power $-dE/dx$ depends on the traversed material as well as the mass and velocity $\beta = v/c$ of the particle, and is usually indicated in MeV·cm^2/g as the energy loss normalized to the density [12]. The detailed formula and its explanations can be found in [14]. As an example, the mass stopping power for μ^+ on copper is shown in Figure 2.3. Particles close to the minimum energy loss rate are called minimum ionizing particles (MIPs). In silicon detectors, MIPs have a stopping power of 1.66 MeV·cm^2/g [12] and produce around 80 electron-hole pairs per traversed µm [13].

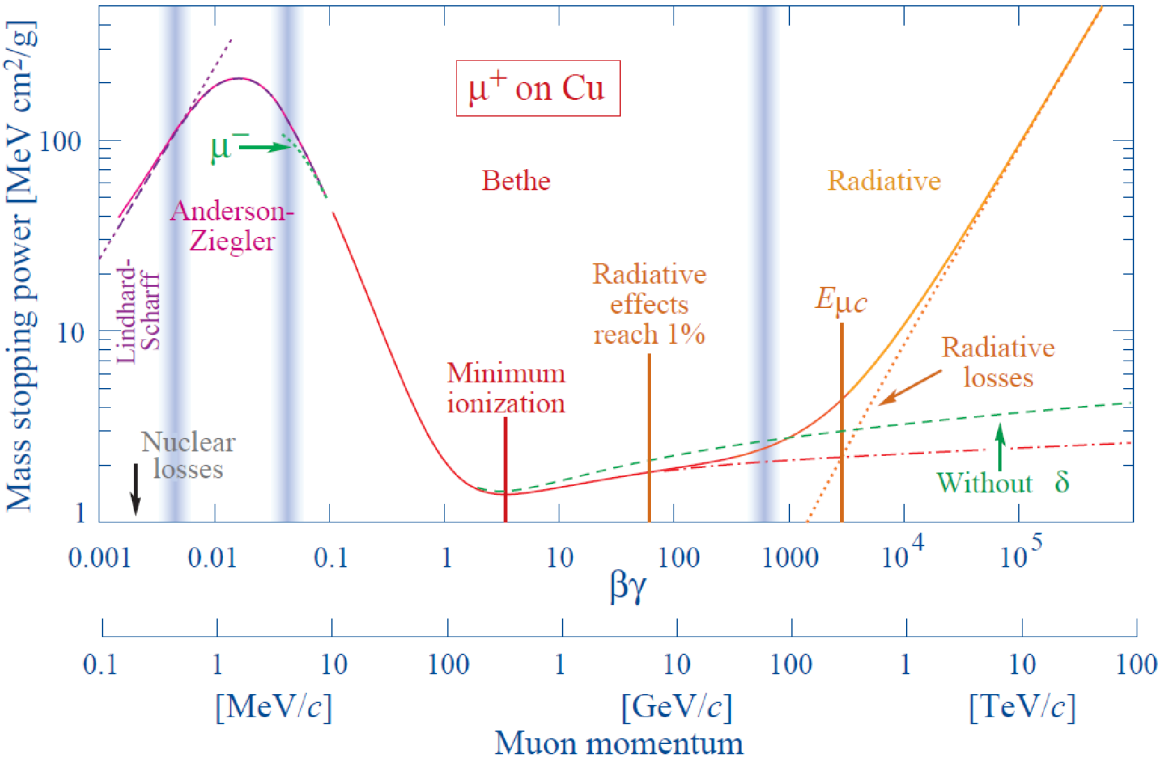

Figure 2.3: Example for a mass stopping power of a μ^+ on copper [14].

For incoming electrons, the Bethe-Bloch formula has to be modified since the target electrons and scattering electrons have the same mass and are therefore undistinguishable. At energies below 10 MeV, electrons primarily lose energy by ionization. Other processes like Møller scattering, Bhabha scattering and positron annihilation also contribute. For electron energies E_e > 10 - 30 MeV, the dominating process for energy deposition is bremsstrahlung. Bremsstrahlung can be explained as the photon emission by an electron which was accelerated in the Coulomb field of a nucleus. The proportionalities of the energy deposition per traversed

length for ionization and bremsstrahlung are shown below:

$$-\left\langle \frac{dE}{dx} \right\rangle_{Ionization} \propto ln(E_e), \tag{2.16}$$

$$-\left\langle \frac{dE}{dx} \right\rangle_{Bremsstrahlung} \propto \frac{E_e}{m^2}, \tag{2.17}$$

where $-\left\langle \frac{dE}{dx} \right\rangle$ is the mean deposited energy per traversed length, E_e is the energy of the incoming electron and m the electron mass. As an example, the fractional energy loss per radiation length X_0 of an electron in lead is shown in Figure 2.4, where X_0 is the characteristic amount of traversed matter for which the energy of the incoming particle is reduces to 1/e of its original value. The total energy loss of electrons in silicon per traversed distance is shown in Figure 2.5.

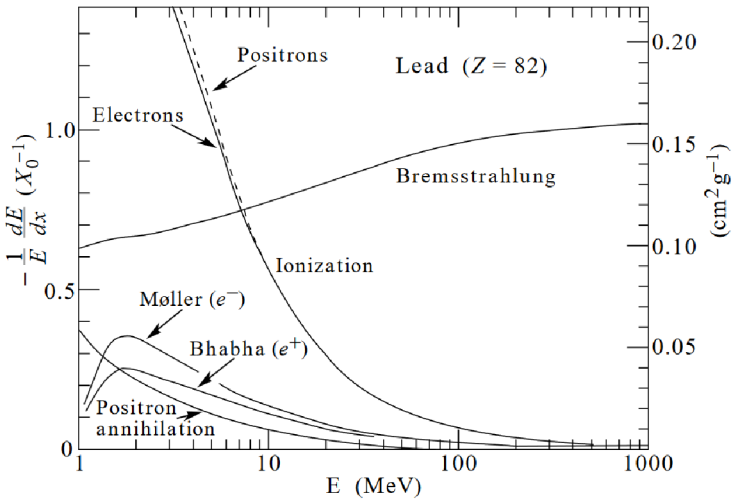

Figure 2.4: Fractional energy loss in units per radiation length X_0 in lead as a function of electron or positron energy [15].

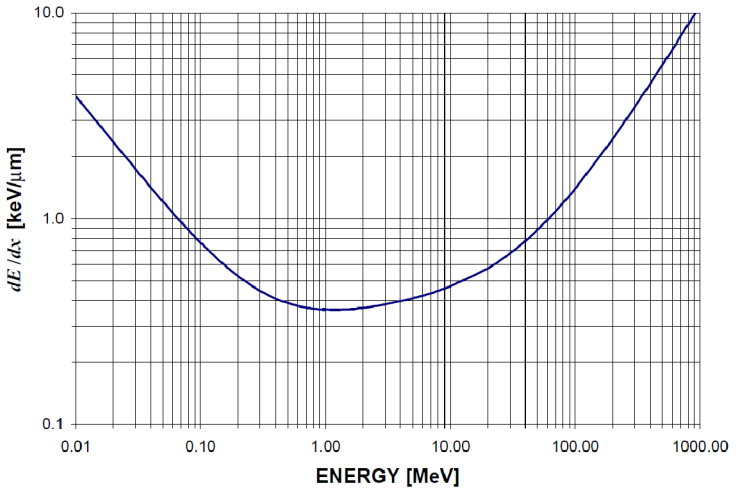

Figure 2.5: Mass stopping power of electrons in silicon in keV/µm [16].

For a MIP, the deposited energy follows a Landau-Vavilov distribution. The Landau-Vavilov distribution describes the asymmetry of the energy deposition and is composed of a Gaussian part corresponding to a high number of ionization processes and a tail towards high energy deposition corresponding to delta rays [12]. The Landau distribution is defined as a definite integral [12]

$$f_L(\lambda) = \frac{1}{\pi}\int_0^\infty e^{-tln(t)-\lambda t}\sin(\pi t)dt, \tag{2.18}$$

where the relationship between λ, the deposited energy E and the most probable value for the deposited energy E_{MPV} is given by

$$\lambda(E_{\mathrm{MPV}},\zeta) = \frac{E - E_{\mathrm{MPV}}}{\zeta} - 0.22278, \tag{2.19}$$

and where ζ is a characteristic of the width of the Landau distribution.

2.2.3 Photon Silicon Interaction and Attenuation

In addition to the production of electron-hole pairs due to ionizing particles, photon interaction with silicon can also produce electron-hole pairs. Photons at low energies in the optical (1.6 eV - 3.2 eV) or near infrared (0.8 eV - 1.6 eV) range mainly interact with material via the photoelectric effect [14]. The photoelectric effect describes the process where a photon transfers all its energy to an atom which emits a shell electron if the absorbed energy exceeds the binding energy. In the case of silicon, the material has an indirect bandgap of 1.12 eV at 300 K. At photon energies below 2.2 eV, independently of the photon energy, one electron-hole pair is produced [17]. For these photon energies, due to momentum conservation at indirect bandgaps, excitations of electrons are only allowed if additional phonon interactions take place. For direct transitions higher photon energies are required. For photons above 50 eV the mean required energy to produce one electron-hole pair is 3.66 eV [17]. If phonons are involved in the excitation process, these phonons introduce a strong temperature dependence on the absorption probability of photons as mentioned in Section 2.2.1. The absorption of light in silicon can be described by [14]

$$I(l) = I_0 e^{-\alpha l}, \tag{2.20}$$

where I_0 is the initial light intensity, α is the attenuation coefficient and l the length passed by the light. The attenuation coefficient depends on the wavelength of the light. At 300 K, for photons with a wavelength of 660 nm ($\sim$1.9 eV), the attenuation coefficient is 2570 cm^{-1} [18]. Using a linear interpolation between the data given in [18] the attenuation coefficient for light with 1015 nm ($\sim$1.2 eV) is approximately 45.5 cm^{-1}.

For photon energies between 60 keV and 15 MeV, the Compton effect dominates [12]. The Compton effect is the elastic scattering of a photon on a shell electron. For photon energies above 1.022 MeV, pair production occurs. Pair production is the conversion process of a photon to an electron-positron pair in the coulomb field of a nucleus. In Figure 2.6, cross sections for

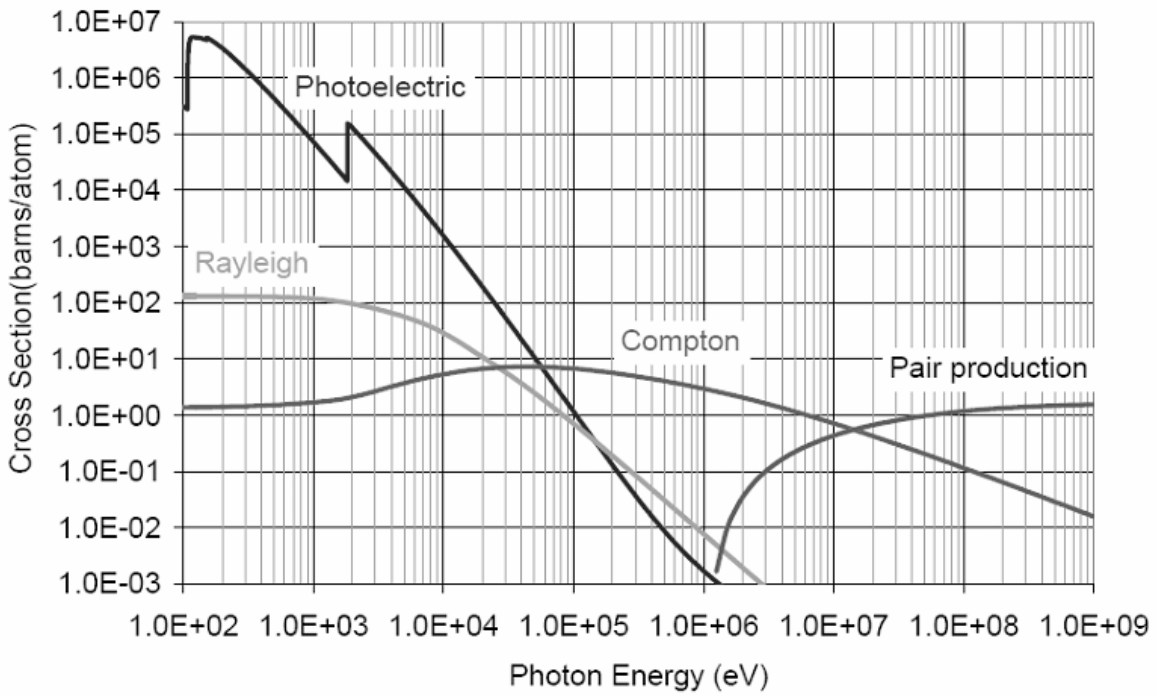

Figure 2.6: Cross sections for different photon-matter interactions in silicon taken from [19].

different absorption processes of photons in silicon are shown. Rayleigh scattering is coherent scattering of the photon on the atoms. This process does not excite or ionize the atoms and is therefore not relevant for particle detection [12].

2.2.4 Working Principle of Silicon Sensors

For an intrinsic (un-doped) semiconductor, the number of thermally created electron-hole pairs exceeds the particle signal by several orders of magnitude. Particle detectors therefore use extrinsic (doped) semiconductors, forming a pn-junction. A pn-junction is formed when p-type and n-type doped material is brought together. Initially the n-type and p-type material is electrically neutral but due to thermal diffusion the loosely bound electrons and holes diffuse across the junction. This process creates a net negative charge in the p-type material and a net positive charge in the n-type material. As a result, a built-in potential arises between the n-type and p-type regions. The resulting force acts opposed to the diffusion of the charge carriers and therefore limits the diffusion depth resulting in thermal equilibrium. The doping concentrations determine the magnitude of the potential barrier. Typically, asymmetrically doped structures with one thin highly doped ($\sim 10^{19}$ cm^{-3} [12]) region (called implants) and one lightly doped ($\sim 2.3 \cdot 10^{12}$ cm^{-3} [12]) region (called bulk material) are used. The region across the pn-junction is free of mobile charge carriers and is called the depletion region, bounded by conductive regions of p-type and n-type material. A sketch of p-type and n-type doped silicon and a pn-junction can be seen in Figure 2.7.

Thermal equilibrium no longer holds once an external field is applied. A positive potential

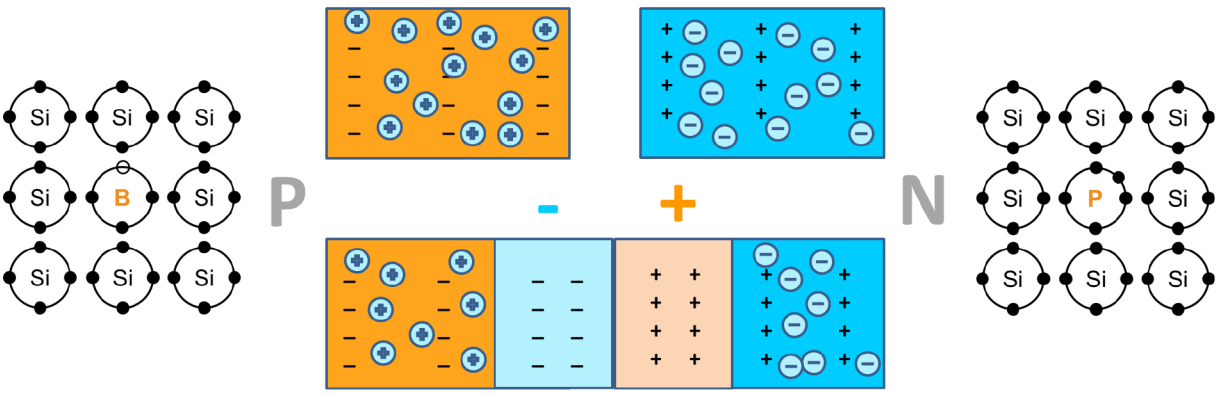

Figure 2.7: Sketch of p-doped and n-doped silicon and the resulting pn-junction. Electrons and holes diffuse across the junction leaving behind a region free of charge carriers.

on the p-region and a negative potential on the n-region is called forward bias and results in an increased current flow across the pn-junction. If the opposite polarity (called reverse bias) is applied the depletion region increases. The pn-junction is a diode with an asymmetric current flow which can be described by the Shockley equation [13]

$$I = I_0(e^{eV/kT} - 1), \tag{2.21}$$

where I_0 is the saturation current, e the elementary charge, V the applied bias voltage, k the Boltzmann constant and T the temperature. The exponential term dominates when a forward bias (positive voltage V) is applied. When a large reversed bias (negative voltage) is applied, the current saturates at $-I_0$ until a critical voltage is reached. Fields exceeding 10 V/µm [13] lead to a so called breakdown where electrons and holes have enough energy to create secondary electron-hole pairs and cause an avalanche. Curves showing the current vs. voltage of a silicon diode are called IV curves and were measured in Section 6.1 for the sensors used within this thesis. The current I_0 is also called the leakage current and depends on temperature and on the defects and impurities of the material. It increases with increasing depletion depth of the material. The depletion region of a reversed biased silicon diode can be seen as a capacitor since it is a region without free charge carriers. The undepleted p- and n-regions form the electrodes with an area A, and the depletion region forms the dielectric ε. The capacitance is given by

$$C = \varepsilon\frac{A}{\omega} = A\sqrt{\frac{\varepsilon eN}{2(V_b + V_{bi})}}, \tag{2.22}$$

where $\omega = \sqrt{\frac{2\varepsilon(V_b+V_{bi})}{eN}}$ is the depletion width for an asymmetrically doped diode, e the elementary charge, N the doping of the bulk material, V_b the bias voltage and V_{bi} the built in voltage. The depletion width increases with the square root of the applied bias voltage for $V_b \gg V_{bi}$ until the diode is fully depleted. Therefore, the capacitance depends on the bias voltage in the following way:

$$C \sim \frac{1}{\sqrt{V_b}}. \tag{2.23}$$

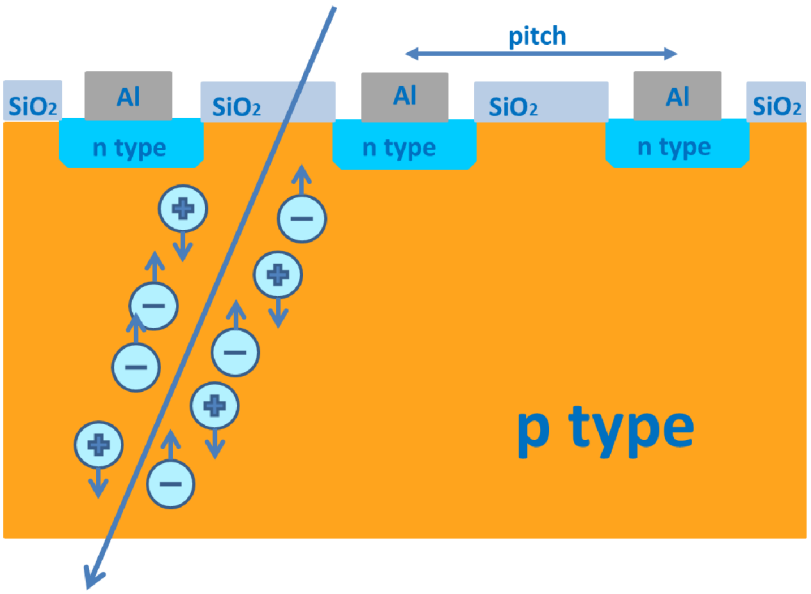

Figure 2.8: Sketch of a cross section of a p-type strip detector. Electron-hole pairs drift towards the electrodes once a reversed bias is applied.

By plotting V_b vs. $\frac{1}{C^2}$ (CV-curve) the depletion voltage of the diode can be determined. The depletion voltage is given by the voltage at which the the curve bends.

Strip Detectors and Signal Formation

In order to gain spatial resolution, the electrodes on the silicon can be segmented. The distance between the centre of one electrode to the centre of the neighbouring one is called pitch. The cross-section of a p-type strip detector with n-type implants is shown in Figure 2.8. Each strip forms a pn-junction and has an aluminium layer on top of the strip implants to form a low-resistance contact to the readout electronics. Adjacent strips are isolated by an oxide layer. The strips can be directly (DC) or capacitively (AC) coupled to the readout. In the case of DC coupling also the leakage current is read out and needs to be compensated for. In addition, DC readout signals undergo pedestal shifts [12] which can saturate the readout electronics. In the case of AC coupling, a thin SiO_2 layer is grown between the strip implant and the aluminium layer acting like a capacitor. As a result, only the changing current reaches the readout electronics whereas the leakage current is dissipated via the power supply [12]. A drawback of AC coupling is the risk of micro damages in the SiO_2 layer which are called pin holes. Pin holes short-circuit the read-out contact and put it on DC potential.

Electrons or photons interact with the sensor material as described in Sections 2.2.2 and 2.2.3. Once radiation is absorbed in the depleted region of the sensor, electron-hole pairs are produced. If a reversed bias is applied, these charge carriers drift towards the electrodes due to the resulting electric field. This movement starts the signal current which lasts until all charge carriers are collected [13]. Electrons and holes contribute with the same polarity to the signal current since they move in opposite direction as indicated in Figure 2.8. The induced current I

by a charge carrier with charge q on a specific electrode can be described by the Shockley-Ramo theorem [12, 13, 20]

$$I = q\boldsymbol{E}_w\boldsymbol{v}, \tag{2.24}$$

where $\boldsymbol{E}_w$ is the weighting field of the considered electrode and $\boldsymbol{v}$ the drift velocity of the electron or hole. The weighting field depends only on the electrode's geometry and determines how a charge motion couples to a specific electrode. It can be derived from the weighting potential Φ_w as $\boldsymbol{E}_w = -\boldsymbol{\nabla}\Phi_w$. The weighting potential is obtained by applying unit potential to one electrode while setting all other potentials to zero. The drift velocity of the charge is given by $\boldsymbol{v} = \mu\boldsymbol{E}$ where μ is the charge carrier mobility and $\boldsymbol{E}$ is the electric field. The total induced current is the sum of all individual currents on each electrodes. The induced charge is obtained by integrating the current over the charge collection time t_c, which is defined as the time a charge carrier needs to traverse the sensitive volume. It depends on the electric field and the charge carrier mobility, which at 300 K in silicon is 1350 V/cm·s^2 for electrons and 450 V/cm·s^2 for holes [13]. For a parallel plate geometry with large overbias, the electric field E can be approximated by a uniform field which goes perpendicular to the plates [13]

$$E = \frac{V_b}{d}, \tag{2.25}$$

where d is the traversed distance and V_b the applied bias voltage. The velocity v of a charge carrier is given by

$$v = \mu E = \mu\frac{V_b}{d}, \tag{2.26}$$

and the collection time can be approximated by

$$t_c = \frac{d}{v} = \frac{d}{\mu E} = \frac{d}{\mu\frac{V_b}{d}} = \frac{d^2}{\mu V_b}, \tag{2.27}$$

where μ is the charge carrier mobility.

It has to be noted that the charge collection time only depends on the doping concentration and not on the applied bias voltage once the sensor is operated partially depleted [13].

2.2.5 Geometric Resolution and Charge Sharing in a Strip Detector

To first approximation, the position resolution of a strip detector is given by its geometry. Electric field lines go parallel with respect to each other in the detector until they bend closely to the surface ending at the electrodes. The electrical segmentation is determined by the pitch p [13]. The probability distribution for a particle passage is given by a box-like response function $f(x) = \frac{1}{p}$. The position resolution is commonly defined as the standard deviation of the distribution of the measurement errors, i.e. the distances between the reconstructed values and

the real values. [12]. For a box-like response function this results in:

$$\sigma = \sqrt{\int_{-p/2}^{p/2} x^2 \cdot f(x)dx} = \sqrt{\int_{-p/2}^{p/2} \frac{x^2}{p} dx} = \frac{p}{\sqrt{12}}. \tag{2.28}$$

In an ideal detector, the produced electron-hole pairs follow the field lines at the origin of their production and end up at the according electrode. In reality, thermal diffusion occurs and spreads the charge carriers transversely in the sensor. The standard deviation of the thermal diffusion is given by [13]

$$\sigma_y = \sqrt{2Dt_c} \tag{2.29}$$

where D is the diffusion constant and t_c the collecting time. The transverse diffusion for electrons and holes is the same, since D is proportional to the charge carrier mobility μ and t_c is inverse proportional to the carrier mobility. With $D = \frac{kT}{e}\mu$ and Equation 2.27, the transverse diffusion is given by [13]

$$\sigma_y = \sqrt{2Dt_c} \sim \sqrt{2\frac{kT}{e}\frac{d^2}{V_b}}. \tag{2.30}$$

For $d = 300$ µm, $T = 300$ K and $V_b = 280$ V, the transverse diffusion results in $\sigma_y \sim 4$ µm. The process of charge being spread to the neighbouring strips due to transverse diffusion is called charge sharing. When the detector is used for single particle detection this process can be used to improve the geometric resolution. An illustration of the charge sharing is shown in Figure 2.9.

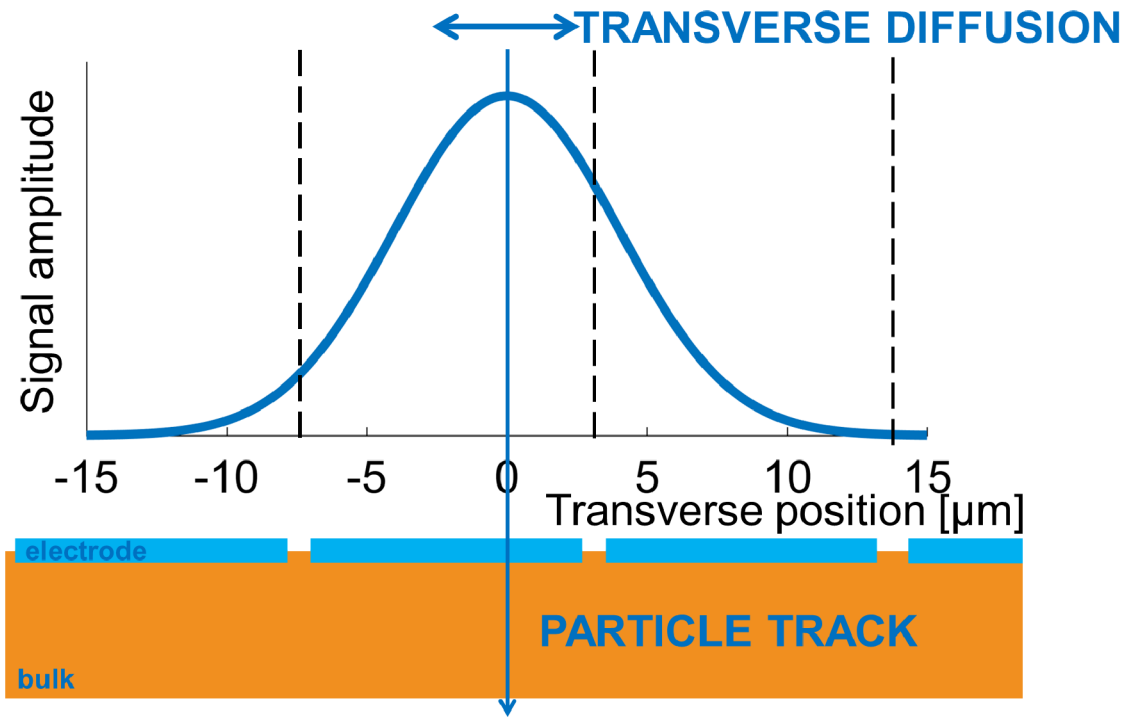

Figure 2.9: Charge sharing on multiple strip electrodes for a transverse diffusion of $\sigma_y = 4$ µm. The charge division boundaries are illustrated by dashed lines.

2.2.6 Plasma Effect in Silicon Sensors

If inside the sensor the electron-hole pair density is high enough to significantly modify the electric field, the behaviour of the produced signals changes. This effect is known as the plasma effect and has been studied for example in [21] for heavily charged particles and in [22, 23] for incoming photons.

The electrons and holes in the sensor form a so-called plasma. Its boundaries shield the inner region from the outer applied electric field and increase the collection time as well as the recombination of electrons and holes [24]. The transverse spread of the signal increases due to the time dependence of the thermal diffusion as shown in Equation 2.29. Once the electrons and holes are separated, electrostatic repulsion effects contribute to the transverse spread. The plasma effect decreases with an increasing electric field and hence a bigger bias voltage at the sensor [25]. If the breakdown voltage of a sensor is sufficiently high, a high operation voltage can therefore minimize the impact of the plasma effect on the sensor signals. The effect of different bias voltages on the signal shape was studied for one STRIDENAS sensor and is discussed in Section 6.3.

Chapter 3

The SINBAD Facility at DESY

SINBAD (Short and INnovative Bunches and Accelerators at DESY) [26] is a dedicated R&D facility at DESY which hosts several experiments: The ARES (Accelerator Research Experiment at SINBAD) linac, including its future upgrade ATHENA-e [27], and the AXSIS (Attosecond X-ray Science: Imaging and Spectroscopy) [28] experiment. In addition, it will host the future KALDERA (Kilowatt Lasers at DESY for Revolutionary Accelerators) laser laboratory. An overview of the SINBAD facility as well as the location of the experiments is shown in Figure 3.1.

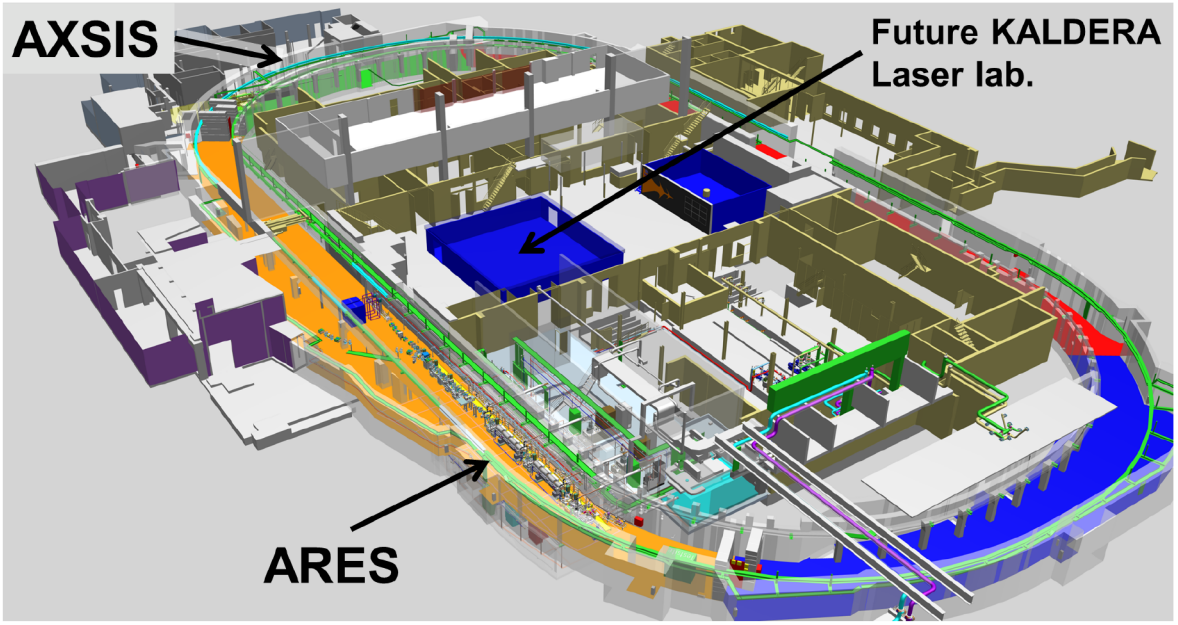

Figure 3.1: Overview of the SINBAD facility and its experiments.

ARES

The ARES linac, currently under commissioning at DESY, is an S-band (2.998 GHz) electron linear accelerator with an energy between 52 MeV and 155 MeV running in single bunch mode with a repetition rate up to 50 Hz [26]. It aims at producing ultrashort bunches with (sub-) fs duration, low charge (0.3-30 pC) [26] and an arrival time jitter of $\sim$ 10 fs [29]. It is therefore

ideally suited to test advanced accelerator concepts like dielectric laser accelerators (DLAs) or external injection into plasma accelerators. DLAs consists of structures which are characterized by µm-scale apertures, hundreds of µm length and acceleration gradients of several 100 MV/m. Those acceleration gradients are achieved by the illumination of microstructured dielectrics with a laser pulse.
Injection into a plasma cell and acceleration to 1 GeV is planned downstream of the ARES beamline within the ATHENA-e upgrade [30].

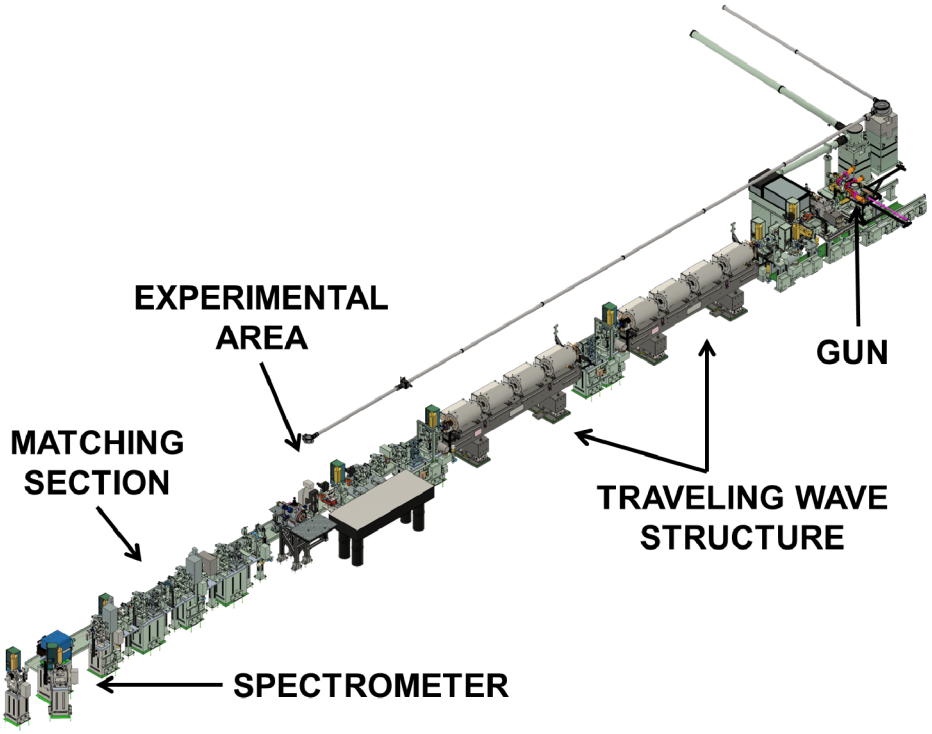

Figure 3.2: CAD model of the ARES linac. Courtesy: F. Mayet (DESY, University of Hamburg)

A CAD model of the ARES linac is shown in Figure 3.2. The rendering shows the RF gun where the electrons are accelerated to 5 MeV as well as the diagnostics elements. It is followed by two traveling wave structures which, for emittance compensation, are surrounded by 2×4 solenoids. The phase of the accelerating wave in the structure can be varied in order to achieve different energy gains of the electrons. If operated on-crest (maximal energy gain), each traveling wave structure provides an energy gain of 75 MeV [26]. In order to compress the bunch length, the traveling wave structures will however be operated off-crest. This process is called velocity bunching and is studied in more detail in [30]. The traveling wave structures are followed by a drift space. This space is foreseen for a future upgrade with a third traveling wave structure and will in the first ARES stages host the experimental area (e.g. for DLA experiments). This section is followed by a matching section hosting four quadrupoles and elements for beam diagnostics like screens for beam position and profile measurements as well as a spectrometer dipole.

The ARES spectrometer is shown in more detail in Figure 3.3. Two diagnostic stations (one

before and one downstream in a straight line of the dipole) are available and can be used to determine the beam entrance angle to the dipole when it is switched off. Another diagnostic station is installed on the spectrometer arm. The STRIDENAS detector (Section 5) will be installed as an add-on to this diagnostic station. The spectrometer dipole is a C-shaped iron dominated magnet of type PDE04. The specifications and the reasons for choosing this dipole are described in Section 4.

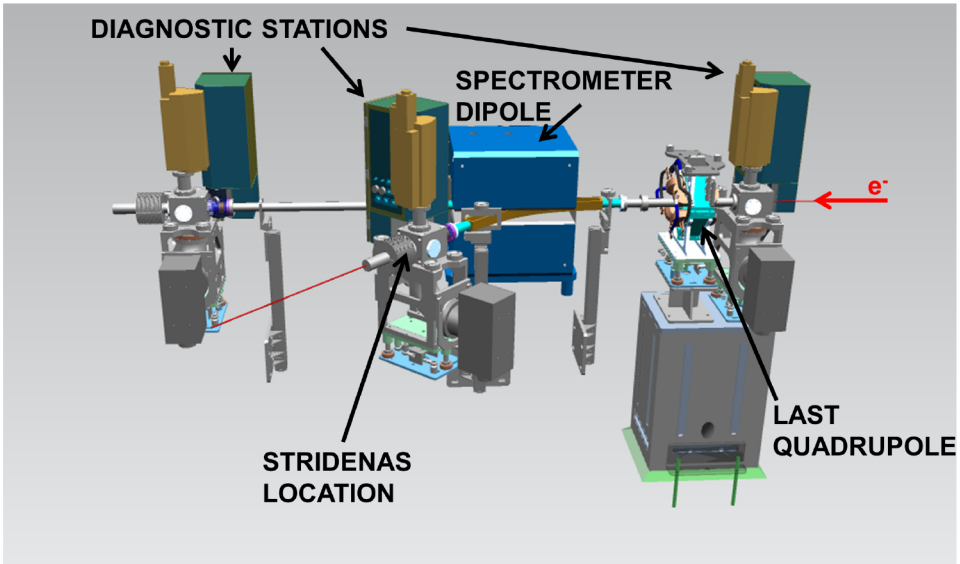

Figure 3.3: CAD model of the ARES spectrometer section. Courtesy: J. Hauser (DESY MVS)

First experiments at ARES include studies of novel acceleration techniques in the scope of the ACHIP (Accelerator on a Chip International Program) [31] collaboration. At the ARES linac, ACHIP plans to use dual grating type DLA structures to accelerate electrons. These structures have an aperture in the µm range and transmit electron bunches in the pC range [32]. The shortness of the ARES bunches allows electron injection to a limited accelerating phase range in the dielectric, resulting in net acceleration. In addition, experiments using a microbunched beam generated by an undulator and a chicane are planned, and promise an enhancement of the accelerated electron fraction [33]. For these experiments at ARES, one working point for injection to the DLA with a 52 MeV and 0.5 pC charge electron beam is foreseen. The minimum expected energy gain is 450 keV [32]. The beam energy spectrum after the DLA has to be measured with the ARES spectrometer which spatially spreads out the distribution. On a screen, charge distributions with locally less than 7 electrons per μm^2 area are expected. A good spatial resolution of these low charge distributions is challenging to achieve with conventional screens [34]. As an R&D project, a detector based on silicon strip sensors called STRIDENAS (STRIp DEtector for Novel Accelerators at SINBAD) is being developed and foreseen at the ARES spectrometer (Sections 5 - 7 of this thesis).

Chapter 4

Characterization and Analysis of the Spectrometer Dipoles for ARES

In order to build the ARES spectrometer, it was decided to use already existing dipoles at DESY. This procedure allowed for a faster implementation at the beamline. Two types of dipoles were chosen and measured in order to validate their suitability for this task. A DORIS III dipole [35] and a PETRA III Extension dipole (PDE) [36]. The B_x, B_y and B_z components of the magnetic field were measured to test their field qualities. Fieldmaps at different vertical positions as well as the trajectories of a simulated beam and the hysteresis for both dipoles were measured. A SENIS 3D Hall sensor [37] was used for the measurements.
The main requirements on the dipole were:

- Adjustability of the dipole current to the ARES electron beam energy.
- Reproducibility of the magnetic field strength corresponding to the applied magnet current.
- No remaining magnetic field when the dipole is switched off so the electron beam can go straight through the dipole.
- A sufficient bending angle to enable energy measurement of the electron beam.

4.1 Specifications of the DORIS and PDE Dipoles

DORIS Dipole

The DORIS III dipole is a C-shaped water-cooled dipole which was used at the former DORIS storage ring [38] and is therefore slightly bend along the DORIS beam trajectory. An overview of its specifications can be found in Table 4.1. The magnet is equipped with corrector coils, which were not used for the following measurements.
A sketch of the dipole and the coordinate system at the test stand can be seen in Figure 4.1, and a picture of the dipole at the test site is shown in Figure 4.3.

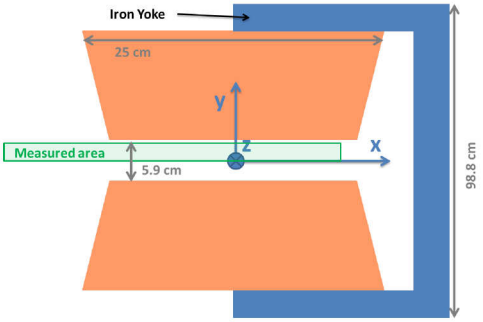

Figure 4.1: Sketch of the measured area of the DORIS dipole (front view).

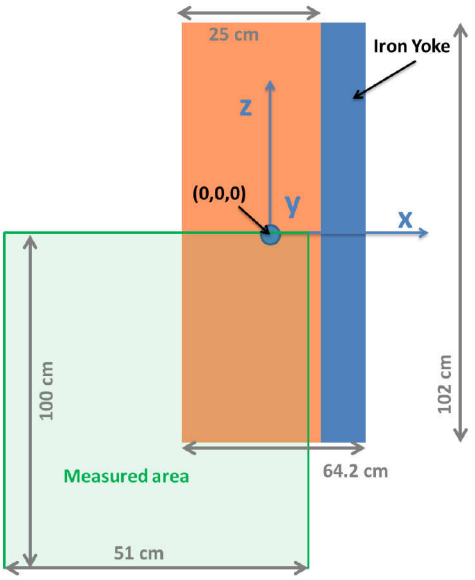

Figure 4.2: Sketch of the measured area of the DORIS dipole (top view).

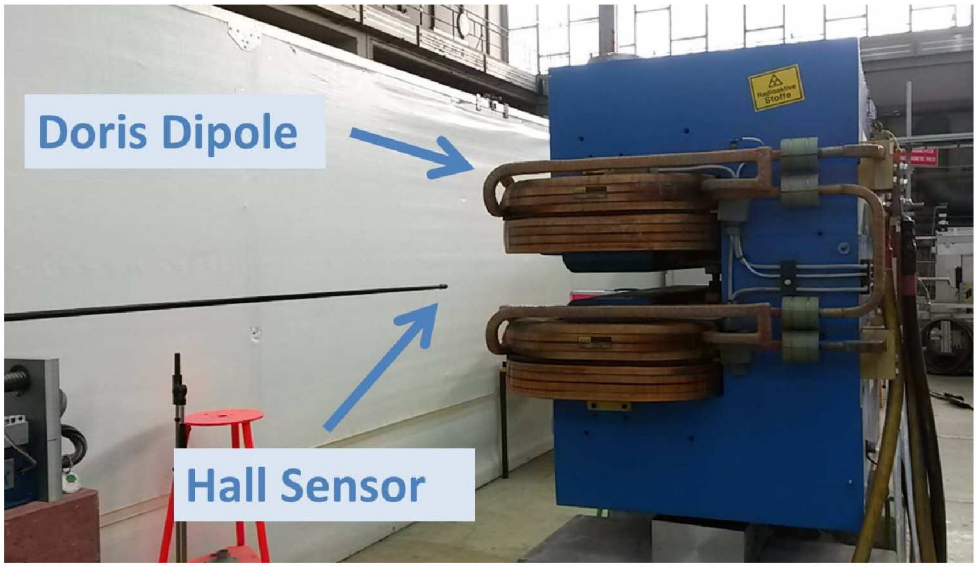

Figure 4.3: Picture of the DORIS dipole at the test site.

Table 4.1: DORIS III dipole parameters [35].

Parameter	**Unit**	**Value**
Magnetic field integral, $B_0 \cdot L$	Tm	1.4
Magnetic field	T	1.4
Nominal current in main coil	A	940
Air gap	mm	60
Length of iron yoke	mm	1020
Total water flow rate	l/min	5.6
Overall weight	kg	5200

Table 4.2: PDE dipole parameters [36].

Parameter	Unit	Value
Magnetic field integral, $B_0 \cdot L$	Tm	0.4
Magnetic field	T	0.8
Current in main coil	A	550
Air gap	mm	48
Length of iron yoke	mm	500
Total water flow rate	l/min	14
Overall weight	kg	1050

PDE

The PETRA dipole type PDE #04 [36] is a C-shaped straight magnet with corrector coils. It was produced for PETRA III and is a spare part. For the following measurements, the corrector coils were not used. A picture of the magnet can be seen in Figure 4.4. An overview of the PDE specifications is shown in Table 4.2.

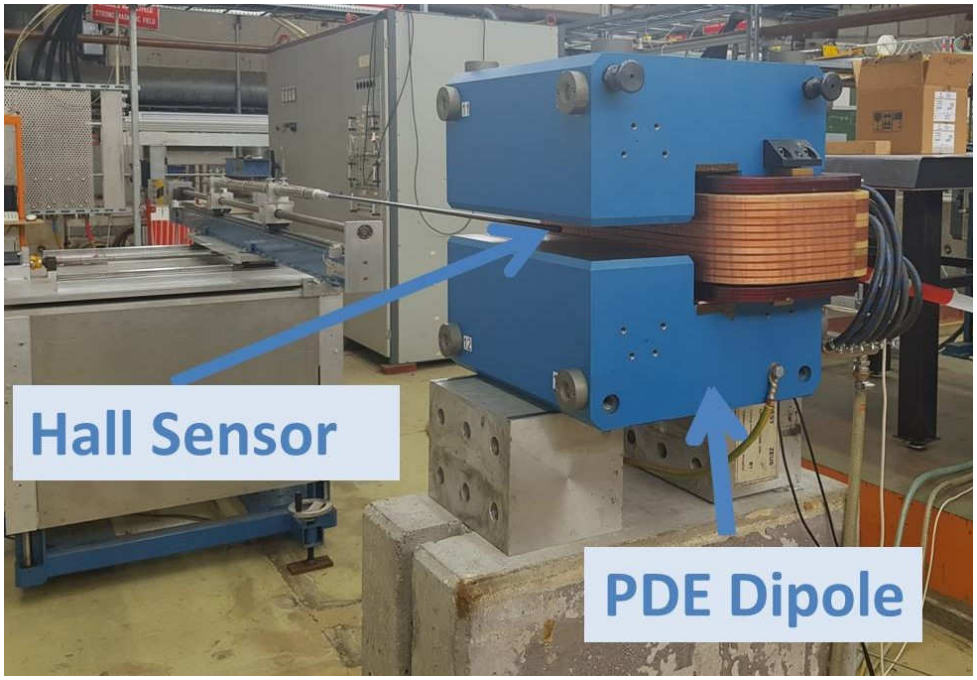

Figure 4.4: Picture of the PDE #04 magnet at test site.

4.2 Measurement Setup

The magnetic fields of the dipoles were measured at the magnet test stand at DESY. To obtain values of the magnetic field in all x, y and z directions, a 3D SENIS Hall sensor [37] was chosen. The sensor was mounted at the end of a lance, which was attached to a linear stage system. The position of the stages could be remotely controlled in all three dimensions. A

grid with desired measurement points in all three dimensions was predefined and fed into the controlling computer. The zero point (0,0,0) of the stages was aligned such that the Hall sensor was positioned in the middle of the magnet. Since the DORIS dipole is slightly bent, its middle was determined by going in parallel to the dipole edge in z direction. Uncertainties on the zero point are $\pm$ 1 mm in x, y and z direction. The Hall sensor was calibrated with a zero-Gauss chamber made from mu-metal [39]. Before starting the measurements, the magnet was cycled four times with a ramping speed of 1 kA per second, in order to get the same starting conditions for each measurement. The grid step size for the DORIS dipole and PDE dipole measurements were set to 10 mm in x direction and 20 mm in z direction. Fieldmaps for the DORIS dipole and PDE dipole were taken at the measurement areas listed in Table 4.3.

Table 4.3: Measurement areas for the DORIS dipole and PDE dipole.

	DORIS dipole @ - 940 A	**PDE dipole @ 600 A**
z range	-1000 mm to 0 mm	-500 mm to 500 mm
x range	-400 mm to 110 mm	-465 mm to 80 mm
y values	0 mm, 5 mm, 10 mm, 15 mm	0 mm, 15 mm, -15 mm

The measured areas of the DORIS dipole are also sketched in Figure 4.1 and Figure 4.2. These areas were chosen because the dipole field was assumed to be symmetric in y and z direction. This is for example not exactly the case for the asymmetric assembly of the corrector coils (Figure 4.3). For the field measurements of the PDE dipole, symmetric y and z values were chosen to avoid these problems. Using the measured fieldmaps, the trajectory of a beam from ARES was tracked through the dipole and another field measurement with smaller grid size around the trajectory points was taken for different currents.
A hysteresis measurement was done at point (0,0,0), ramping the current between $+600$ A and -600 A for the PDE and between $+1200$ A and -1200 A for the DORIS dipole. In both cases, the current was ramped with a speed of 16 A per second.

SENIS Hall Probe System and Measurement Uncertainties

The SENIS's C-H3A-10m [37] is an integrated Hall Probe System based on a single chip. The device consists of a silicon sensor chip including Hall elements, biasing circuits, amplifiers and a temperature sensor. These components give an analogue voltage output for each of the three components of the magnetic flux as well as an output for the chip temperature [37]. A photo of the SENIS 3D and the dimensions of the sensor's sensitive point can be seen in Figure 4.4 and Figure 4.5 respectively. Relevant quantities are listed in Table 4.4.
Measurement uncertainties arise due to the Hall probe measurement accuracy, uncertainties of the temperature correction, uncertainties due to elongation of the dipole due to temperature change, uncertainties of the alignment of the (0,0,0) point, uncertainties due to the bending of the lance and a tilt in the SENIS sensor, uncertainties of the zero setting of the SENIS sensor

and the uncertainty of the stepper motor.

To estimate the error on a possible deviation of 1 mm from the zero point, an interpolation for measurements in the x plane between $-20 < x < 40$ and in the z plane between $-80 < z < 80$ was performed. The change of the B_y component of the PDE dipole along the x plane agrees well with the measured data from the PDE certificate sheet and therefore might arise due to imperfections of the magnet surface. All measured points of the fieldmaps were approached from the same direction and therefore uncertainties of the stepper motor should only affect the first outer measured points. The temperature at the test site varied around 23 °C ± 3°C leading to a maximal uncertainty of ± 0.15 mT.

A list of possible sources for uncertainties and an estimation of their quantity is shown in Table 4.5. All values are negligible compared to the measurement accuracy given by the Hall sensor itself. The overall measurement uncertainty is therefore estimated with ± 2 mT.

Table 4.4: SENIS Hall Probe device properties. The presented values apply for T = 23 °C [37].

Parameter	**Unit**	**Value**
Maximum (full scale) magnetic flux density	T	± 3
Linear range of magnetic flux density (B_{LR})	T	± 2
Accuracy	%	0.1 of B_{LR}
Offset (B = 0 T) $V_{\text{off}}(B_{\text{off}})$	mV (mT)	< ± 3 (0.6)
Temperature coefficient of the offset	mV/°C (mT/°C)	< 0.25 (0.05)

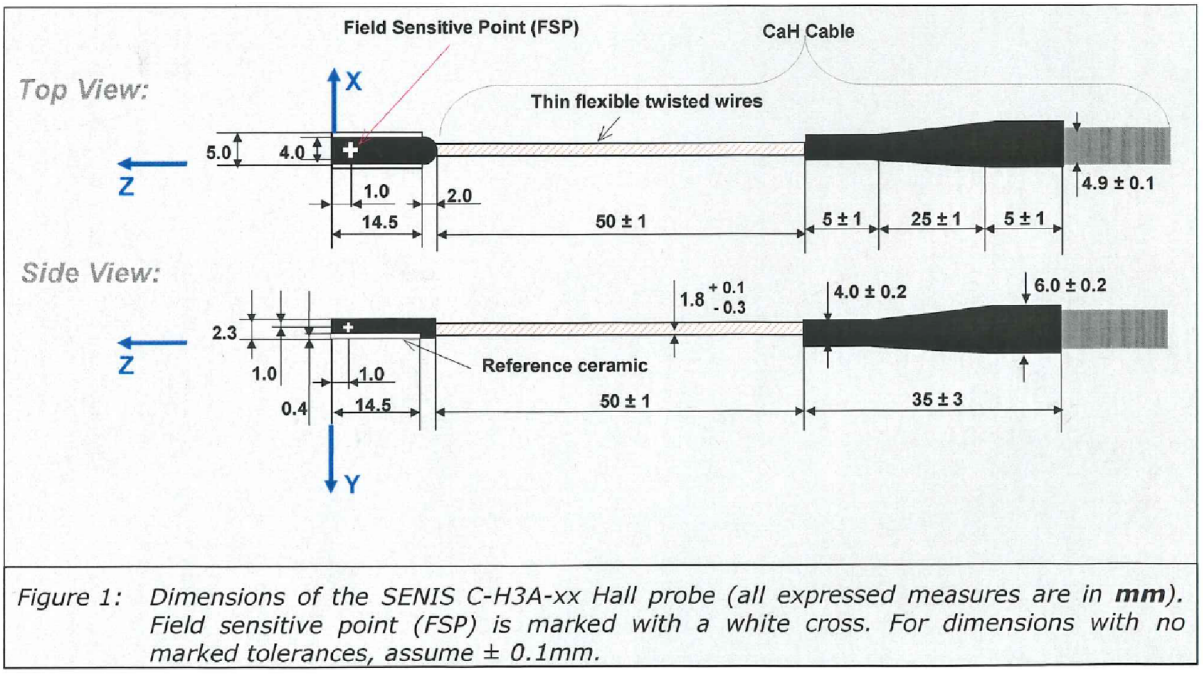

Figure 4.5: Dimensions of the SENIS Hall Probe. The field sensitive point is marked with a white cross [37].

Table 4.5: Magnetic field measurement uncertainties of the SENIS Hall Probe device [37].

Parameter	**Unit**	**Uncertainty**
Offset from zero point (0,0,0)	mm	$\pm$ 1
Uncertainty of B_x due to deviation in x direction from zero point	mT/mm	0.002
Uncertainty of B_y due to deviation in x direction from zero point	mT/mm	0.1
Uncertainty of B_z due to deviation in x direction from zero point	mT/mm	0.0005
Uncertainty of B_x due to deviation in z direction from zero point	mT/mm	0.00004
Uncertainty of B_y due to deviation in z direction from zero point	mT/mm	0.0009
Uncertainty of B_z due to deviation in z direction from zero point	mT/mm	0.0002
Bending of the lance	$^\circ$	1
Temperature change	mT	$\pm$ 0.15
Measurement uncertainty	mT	$\pm$ 2

Data Correction for the Tilt of the SENIS Hall Probe Sensor

During the measurements, the Hall sensor was slightly tilted. The measured data was corrected for that tilt in the following way. The magnetic field at point (0,0,0) consists only of the B_y component. Therefore the tilt was approximated at this point by taking the fraction of the B_x on B_y as well as the B_z on B_y component in this point. A rotation of the coordinate system was performed and the corrected components obtained as

$$B_x^{\text{corr}} = B_x \cdot \cos(\frac{B_x^0}{B_y^0}) - B_y \cdot \sin(\frac{B_x^0}{B_y^0}), \tag{4.1}$$

$$B_z^{\text{corr}} = B_z \cdot \cos(\frac{B_z^0}{B_y^0}) - B_y \cdot \sin(\frac{B_z^0}{B_y^0}). \tag{4.2}$$

The tilt angle was found to be less than 1° in all directions. For small angles the following approximations are valid:

$$\sin(\text{x}) \approx \text{x},\ \cos(\text{x}) \approx 1 \text{ and } \tan(\text{x}) \approx \text{x}.$$

Equations 4.1 and 4.2 can therefore be approximated by

$$B_x^{\text{corr, approx}} = B_x - B_y \cdot \frac{B_x^0}{B_y^0}, \tag{4.3}$$

and

$$B_z^{\text{corr, approx}} = B_z - B_y \cdot \frac{B_z^0}{B_y^0}. \tag{4.4}$$

For the B_y component, the tilt in the x plane as well as the tilt in the z plane has to be taken into account. The correction was performed in the following way:

$$B_y^{\text{corr, approx}} = B_y + B_x \cdot \frac{B_x^0}{B_y^0} + B_z \cdot \frac{B_z^0}{B_y^0}. \tag{4.5}$$

Due to the design and mounting of the SENIS Hall probe device, no tilt between the x and z plane was assumed at the measurement setup.

4.3 Measurement Results

DORIS Dipole

The fieldmap for one half of the DORIS dipole at y = 0 mm is shown in Figure 4.6 for the B_x, B_y and B_z component. The maximal absolute measured values for the three components of the magnetic field are $|B_x|_{\max} = (0.022 \pm 0.002)$ T, $|B_y|_{\max} = (1.428 \pm 0.002)$ T and $|B_z|_{\max} = (0.015 \pm 0.002)$ T. The magnetic field along a simulated beam trajectory was measured and the field integral calculated numerically. This value was used to obtain the bending angle θ. By using Equation 2.3, for a 155 MeV electron beam and a magnet current of -940 A, this results in a bending angle of

$$\theta \approx (57.2 \pm 0.3)^\circ.$$

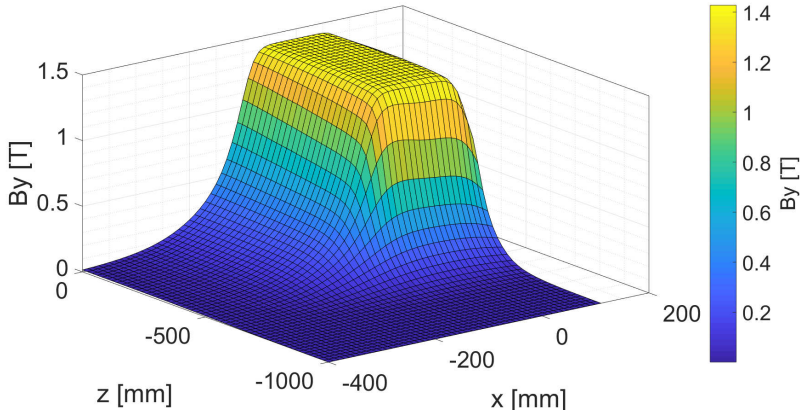

(a) Fieldmap of the B_y component [T] of the DORIS dipole.

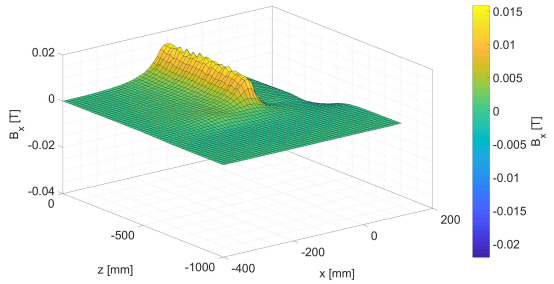

(b) Fieldmap of the B_x component [T] of the DORIS dipole.

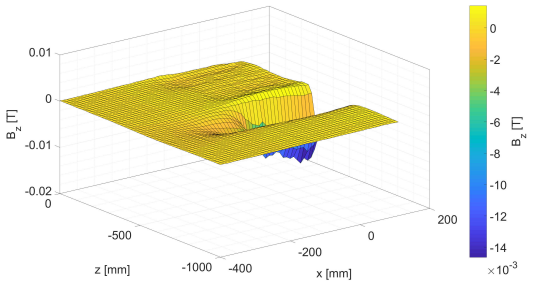

(c) Fieldmap of the B_z component [T] of the DORIS dipole.

Figure 4.6: DORIS dipole fieldmaps measured at -940 A and y = 0 mm.

PDE

The PDE dipole was measured at 600 A. Since the applied current had the opposite sign to the applied current for the DORIS dipole measurements, the orientation of the B_y field was inverted. This enabled a better comparison of the two dipoles. The complete fieldmaps for the B_x, B_y and B_z component at $y = 0$ mm are shown in Figure 4.7. The maximal absolute measured values at $y = 0$ mm for the three components of the magnetic field are $|B_x|_{\max} = (0.004 \pm 0.002)$ T, $|B_y|_{\max} = (0.872 \pm 0.002)$ T and $|B_z|_{\max} = (0.003 \pm 0.002)$ T. The bending angle for the PDE dipole was obtained in the same way as for the DORIS dipole. For a 155 MeV electron beam and a magnet current of 600 A this leads to a bending angle of

$$\theta \approx (46.4 \pm 0.3)^\circ.$$

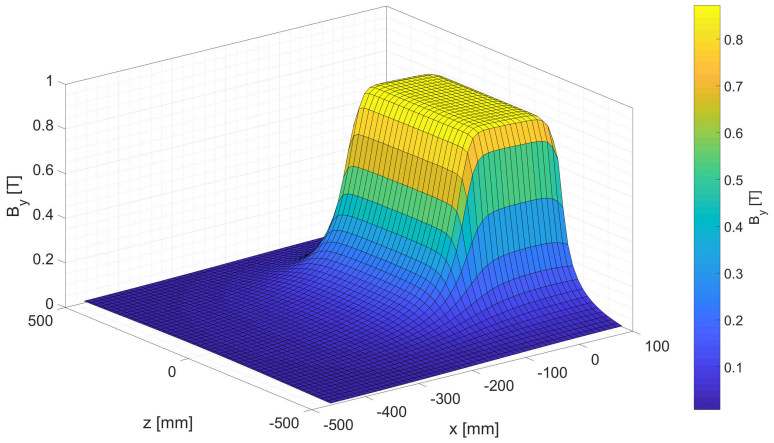

(a) Fieldmap of the B_y component [T] of the PDE dipole.

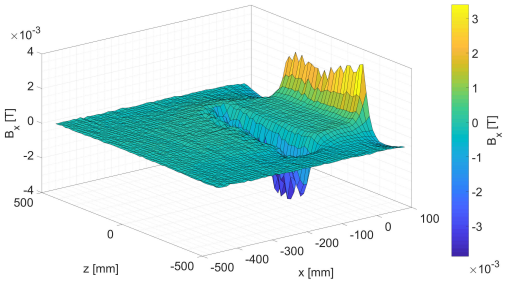

(b) Fieldmap of the B_x component [T] of the PDE dipole.

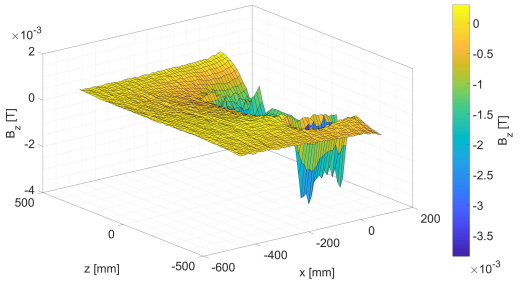

(c) Fieldmap of the B_z component [T] of the PDE dipole.

Figure 4.7: PDE dipole fieldmaps measured at 600 A and $y = 0$ mm.

In an ideal dipole, the magnetic field only consists of a B_y component. However, due to the dipole edges and imperfections, a B_x and B_z component of the magnetic field also exists (see Section 2.1.2). The ratio of the B_x component with respect to the maximum B_y component is shown in Figure 4.8, where it can be seen that it is in the order of 0.4 %. The same was done

for the B_z component and is shown in Figure 4.9, where it can be seen that it is in the order of 0.3 %.

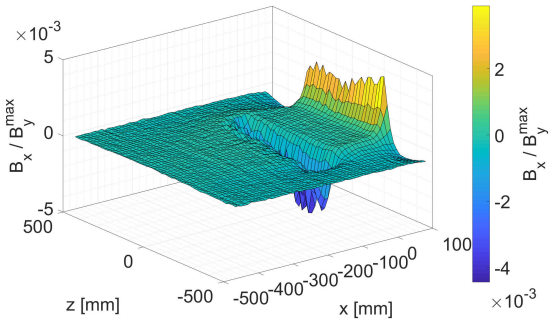

Figure 4.8: The fraction of the B_x component on the maximal B_y component for the PDE dipole is shown for y = 0 mm and a current of 600 A.

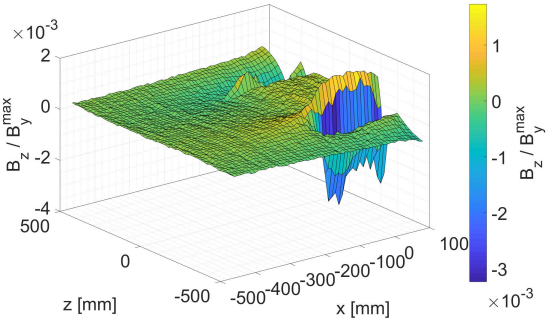

Figure 4.9: The fraction of the B_z component on the maximal B_y component for the PDE dipole is shown for y = 0 mm and a current of 600 A.

Since electron beams of different energy need to always pass through a static beam pipe with an aperture of 32 mm, the magnetic field of the dipole needs to be adjusted accordingly. This is done by changing the applied magnet current. The dependence of the B_y field on the current was measured for an area around the beam pipe. Its trajectory was determined by tracking a 155 MeV beam in the expected magnet field for a 600 A current. The B_y field along the pathlength s of the beam at y = 0 mm (as sketched in Figure 4.10) is shown in Figure 4.11 for different currents. Neglecting saturation effects and fringe fields, the magnetic field was found to be proportional to the applied magnet current, which was one of the requirements on the spectrometer dipole. In Figure 4.12, the relation between the beam momentum and the necessary applied magnet current, such that the beam can go through the beam pipe, is shown. In addition, the field integral for a fixed bending angle (i.e. static beampipe) of the dipole is included. The momentum values were obtained by using Equation 2.3. The field integral along the particle trajectory was calculated numerically from the measured data shown in Figure 4.11. The dashed lines in Figure 4.12 represent an upper and lower momentum limit assuming a 2 mT uncertainty on the measured magnetic field values.

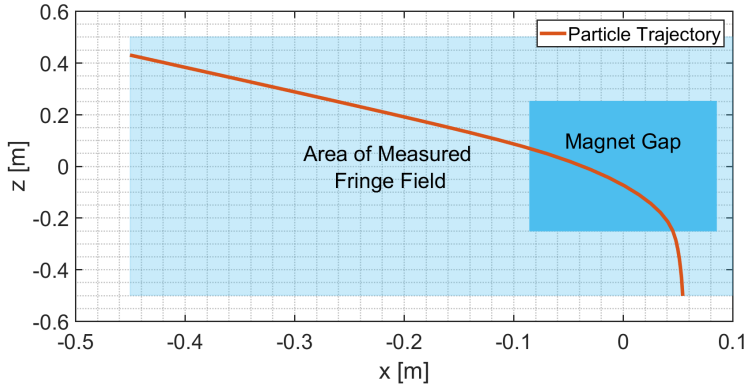

Figure 4.10: Sketch of the electron trajectory through the PDE dipole at y = 0 mm.

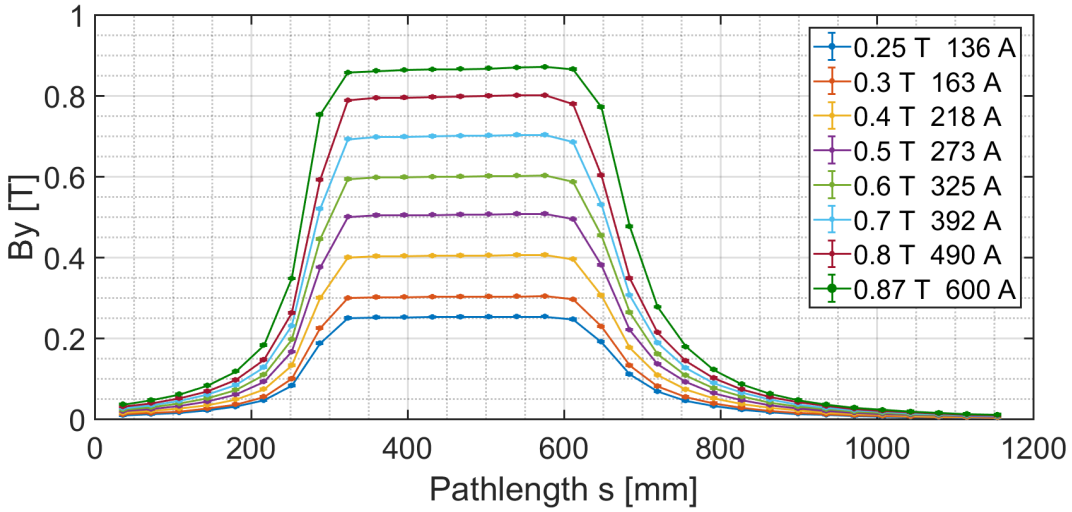

Figure 4.11: B_y [T] along the pathlength s [mm] of the predicted trajectory of a beam at $y = 0$ mm.

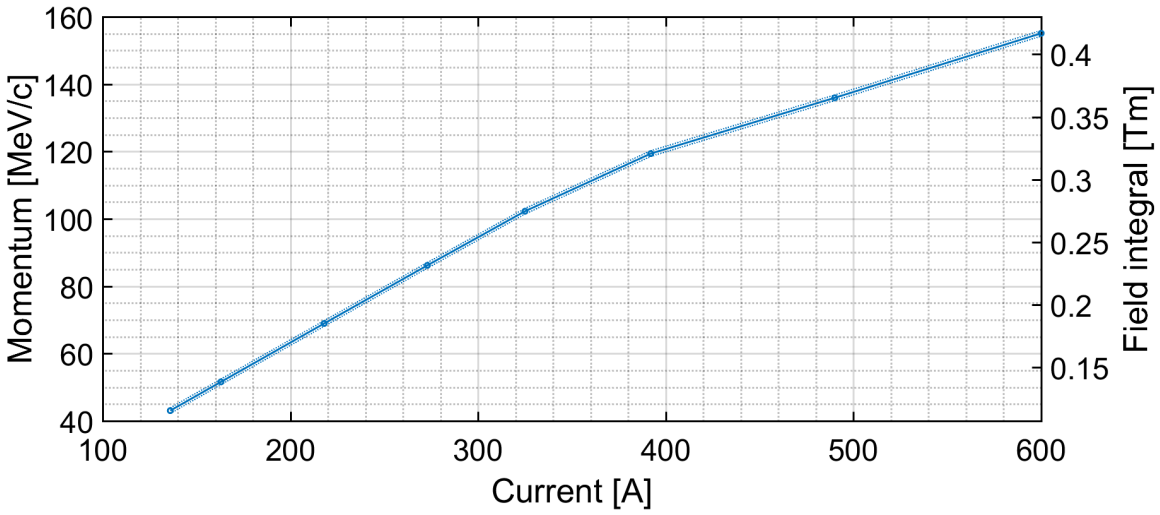

Figure 4.12: Relation between the applied magnet current and the corresponding particle momentum as well as the field integral for a fixed bending angle of the PDE dipole.

To check for saturation effects as well as deviations in the magnetic field due to up and down ramping of the magnet current, the hysteresis curve at the (0,0,0) point of the PDE was measured and is shown in Figure 4.13. The difference between the up and down ramp of the current is 5 mT and therefore hardly visible in the plot. A zoom at a magnet current of 0 A shows a deviation of ± 2.2 mT from the zero point which deviates from the measurement accuracy of the Hall sensor by only 0.2 mT. A zoom at a magnet current of -500 A shows a difference of 1.8 mT between up and down ramp. Therefore no problems for the operation due to cycling of the magnet are expected. This is of interest since, in addition to spectrometer operation, an option for the beam to go straight through the dipole exists. In this mode, the dipole will be switched off and no magnetic field on the beam axis must remain. In addition, the measured hysteresis curve was implemented in the magnet control system.

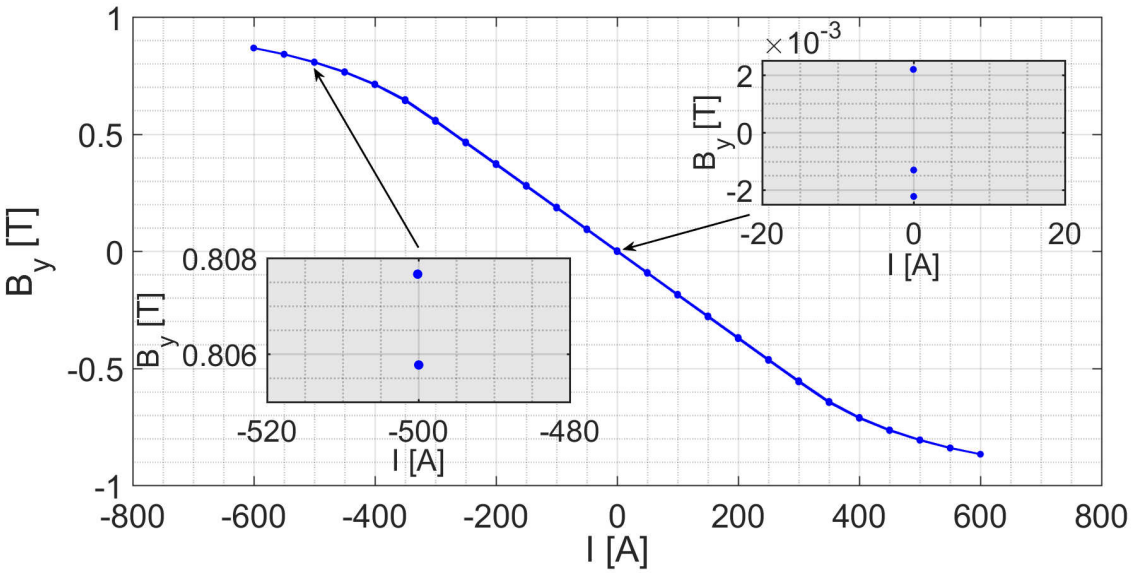

Figure 4.13: Measured hysteresis curve of the PDE dipole between 0 A and ± 600 A.

Comparison of Both Dipoles

To illustrate the differences of the magnetic fields of the DORIS dipole and PDE dipole, comparison plots are presented. When performing simulations of the electron beam through the dipoles using the measured fieldmaps, the B_x component was found to be the most critical one. The normalized B_x values for the DORIS dipole and the PDE dipole are shown in Figure 4.14 and 4.15 respectively. Cuts through the z plane as indicated in these plots, are shown in Figure 4.16 for both dipoles. A clear reduction of the normalized B_x value from $\sim$ 1.5 % of B_y^{DORIS} for the DORIS dipole to $\sim$ 0.4 % of B_y^{PDE} for the PDE dipole is visible. The normalized B_y values for the DORIS dipole and the PDE dipole are shown in Figures 4.17, 4.18 and 4.19 to illustrate a sufficient field quality and a fast reduction of the magnetic field strength after the dipole edge.

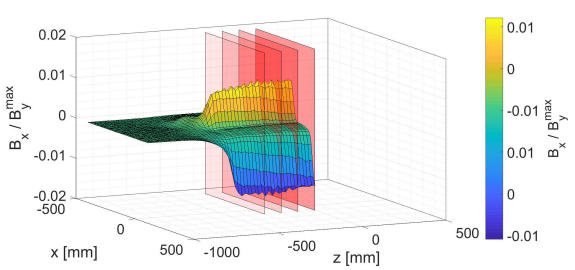

Figure 4.14: Indication of cutting planes for the DORIS dipole. The fraction of the B_x component on the maximal B_y component is shown for $y = 0$ mm.

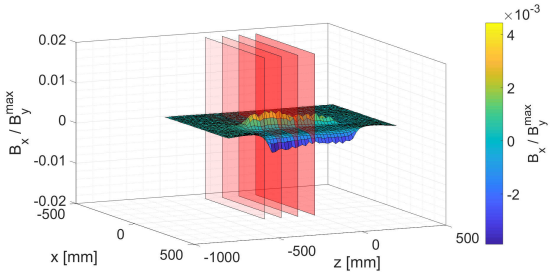

Figure 4.15: Indication of cutting planes for the PDE dipole. The fraction of the B_x component on the maximal B_y component is shown for $y = 0$ mm.

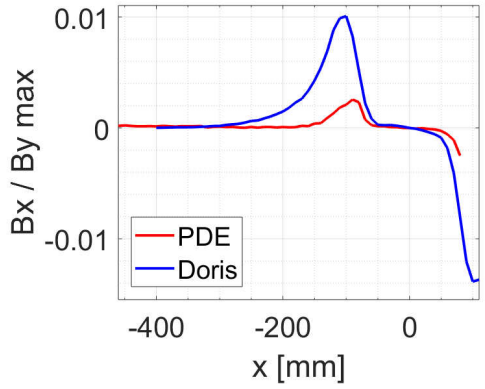

(a) The fraction of the B_x component on the maximal B_y component is shown for $z = 0$ mm and $y = 0$ mm.

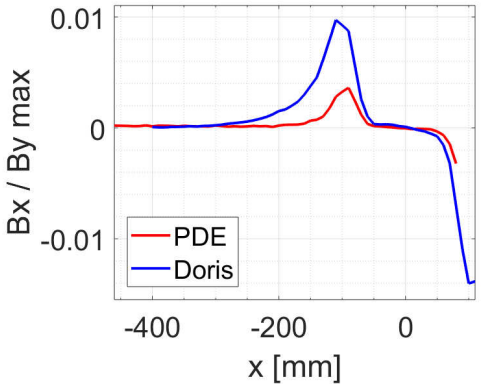

(b) The fraction of the B_x component on the maximal B_y component is shown for $z = -100$ mm and $y = 0$ mm.

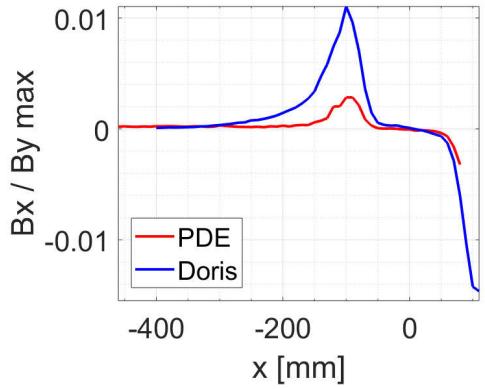

(c) The fraction of the B_x component on the maximal B_y component is shown for $z = -200$ mm and $y = 0$ mm.

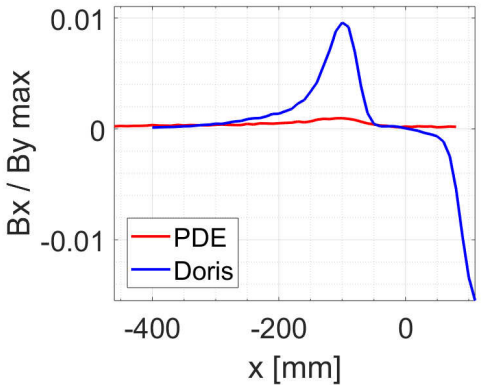

(d) The fraction of the B_x component on the maximal B_y component is shown for $z = -300$ mm and $y = 0$ mm.

Figure 4.16: Comparison of the B_x component of the DORIS dipole and the PDE dipole magnetic field measurements at different z values.

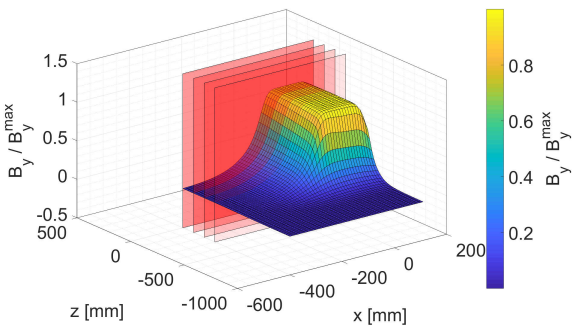

Figure 4.17: Indication of cutting planes for the DORIS dipole. The fraction of the B_y component on the maximal B_y component is shown for $y = 0$ mm.

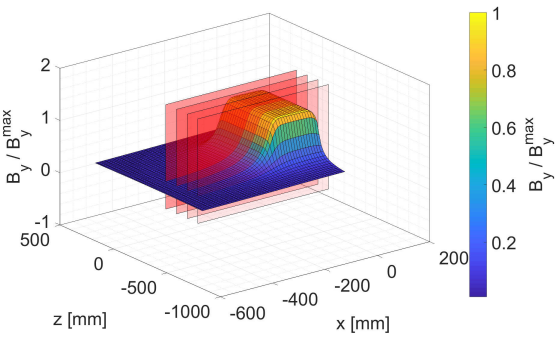

Figure 4.18: Indication of cutting planes for the PDE dipole. The fraction of the B_y component on the maximal B_y component is shown for $y = 0$ mm.

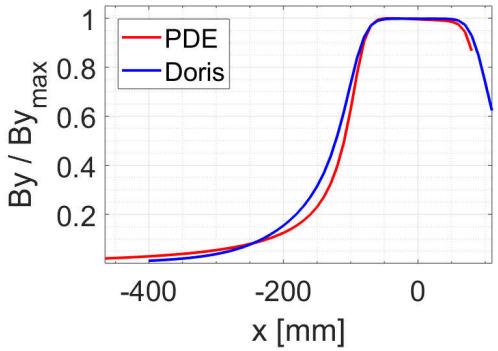

(a) The fraction of the B_y component on the maximal B_y component is shown for $z = 0$ mm and $y = 0$ mm.

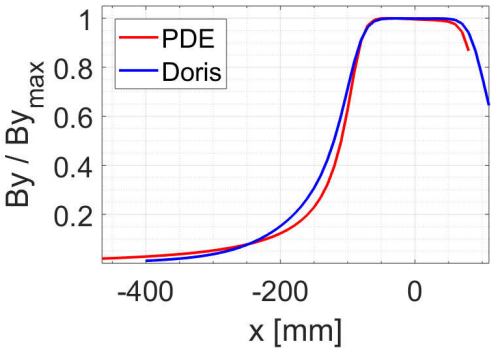

(b) The fraction of the B_y component on the maximal B_y component is shown for $z = -100$ mm and $y = 0$ mm.

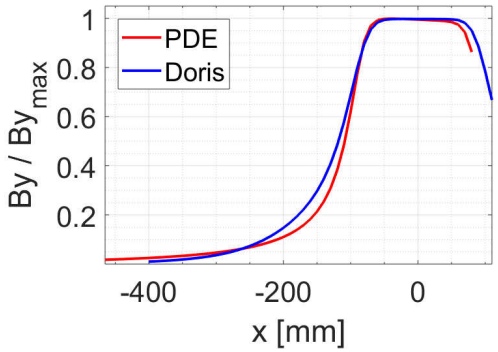

(c) The fraction of the B_y component on the maximal B_y component is shown for $z = -200$ mm and $y = 0$ mm.

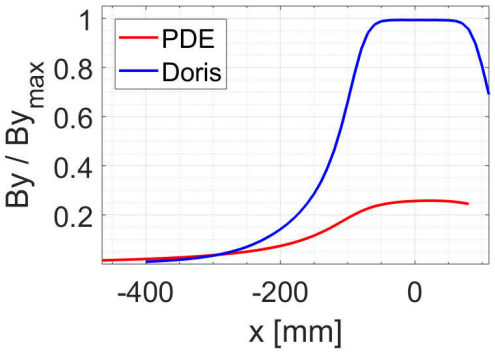

(d) The fraction of the B_y component on the maximal B_y component is shown for $z = -300$ mm and $y = 0$ mm.

Figure 4.19: Comparison of the B_y component of the the DORIS dipole and the PDE dipole magnetic field measurements at different z values.

4.4 Conclusion

The magnetic fields of two available dipoles at DESY were measured with a 3D SENIS Hall sensor. The here presented fieldmaps were used for beam tracking simulations of electron beams passing through the dipole. These beam tracking simulation showed that the B_x component of the DORIS dipole caused a kick of the beam in y direction and therefore the beam to deviate from the desired beam trajectory. Furthermore, a non linear behaviour between the magnet current and resulting B_y did not allow for adjusting the magnet strength for different beam energies without measuring the field for every possible current. However, beam tracking simulation showed that the field quality of the PDE satisfies the requirements for the spectrometer dipole at ARES. Adjustments of the magnet current allow for different particle energies to go through the static beam pipe. The measurement of the hysteresis curve showed that no problems due to hysteresis effects are expected. The PDE dipole was therefore chosen for installation at the ARES spectrometer beamline. The installation of the dipole is currently under preparation.

Chapter 5

STRIDENAS - A Silicon Strip Detector for Novel Accelerators at SINBAD

A beam profile monitor capable of measuring sub-pC beam distributions is needed downstream of the spectrometer dipole, where electron distributions below 7 electrons per μm^2 area are expected. For this purpose, a Silicon STRIp DEtector for Novel Accelerators at SINBAD (STRIDENAS) has been designed, developed and commissioned in the frame of this master thesis. It uses two silicon strip sensors from the ATLAS12EC series. These sensors are mounted and bonded to a printed circuit board (PCB). The readout is done by four charge-to-digital converters with 16 channels, which can be connected to a computer.
The requirements on the STRIDENAS detector are:

- A spatial resolution in the 100 µm range to resolve the beam features of interest.
- To be able to detect electron distributions with a dynamic charge range after the spectrometer dipole between $\sim$ 1 fC and $\sim$ 40 fC per readout channel (as expected for example at the ACHIP experiment).
- The survival of the setup under the incoming electron rate ($\sim 10^6$ electrons per shot).
- To be as compact as possible and designed to be easily placed in electron beams for example to perform functionality tests.
- To be shielded from the ambient light.
- The possibility to remotely control the readout of the detector.
- Ultra-high vacuum compatibility ($< 10^{-9}$ mbar) of the final setup.

These requirements impose certain challenges on the STRIDENAS design. Silicon sensors for example are usually used to detect single particles. The detected signal is then directly amplified as close to the sensor as possible to reduce the impact of noise. For the STRIDENAS detector at ARES, an electron intensity $\sim 10^5$ times higher per readout channel is expected.

The behaviour of silicon sensors under such an intensity is not well studied and needs to be explored. Furthermore, the integration of the detector in ultra-high vacuum poses an additional challenge to place any amplifier close to it. This is because the amplifiers need to be cooled during operation, which can be more difficult in vacuum.

In the following, the different parts of the STRIDENAS design are presented.

5.1 Sensor Specifications

The ATLAS12EC sensors [40] were developed for the High Luminosity LHC ATLAS inner tracker upgrade [10]. They were fabricated by Hamamatsu Photonics [41] and are designed for high radiation environments with a fluence up to 10^{15} neutron equivalent per cm^2 [42]. For the ATLAS inner tracker upgrade, large area sensors (97×97 mm^2) will be used. In addition to the production of these large area sensors, each produced wafer also contains several test structures and miniature sensors to perform irradiation studies. A layout of the wafer structure can be seen in Figure 5.1. The miniature sensors are fully-equipped 1×1 cm^2 miniature versions of the large area sensors. The baseline material of the sensors is float zoning p-type silicon in 150 mm wafers with a thickness of 310 ± 25 µm. Each miniature sensor has 103 n-type AC couples strips with a pitch of 74.5 µm. The sensors used for this work are ATLAS12 End Cap (EC) miniature sensors from two different wafers (in the following referred to as W + the wafer number). Different miniature sensors from the same wafer are distinguished by their position on the wafer (P + number) as also indicated in the wafer structure in Figure 5.1. The sensors are

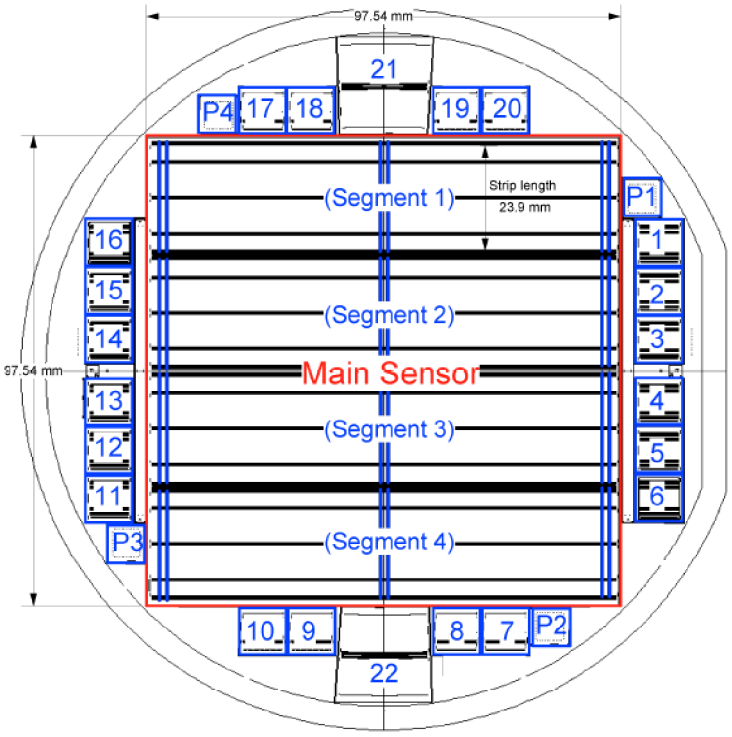

Figure 5.1: Example of a wafer structure [43].

equipped with a punch-through protection, which prevents large voltages on the strip implants in case of a high number of charge carriers in the bulk material of the sensor. The survival of the ATLAS miniature sensors under 10^{11} protons in a 2 mm radius beam was studied in [44]. The observed damage by up to 10^{11} protons in a 2 mm radius proton beam was considered acceptable [45]. For the beam charges at ARES ($2 \times 10^6 - 2 \times 10^8$ electrons), no damages of the sensor are expected. All sensors used in the following studies are listed in Table 5.1. Further details of the design values of the sensors are presented in Table 5.2.

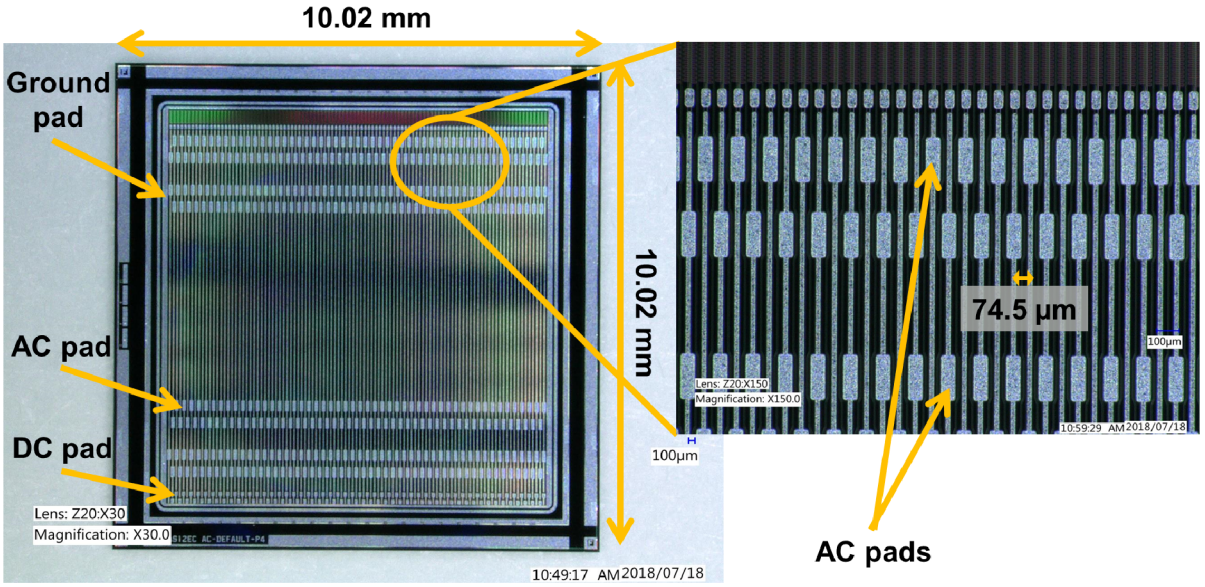

Figure 5.2: Microscopic picture of the ATLAS12EC W012-P4 sensor.

The size of the sensor, the pitch and their n-on-p structure (corresponding to a negative current on the strips) match well the requirements of the STRIDENAS detector. Their suitability for the tasks of the STRIDENAS detector has been tested in Chapter 6 and 7.

A picture of one of the ATLAS12EC miniature sensor is shown in Figure 5.2. The high voltage supply for these sensors is given on the backside, while the ground can be set on the ground pad. On each side of each strip two AC bonding pads are available.

Table 5.1: List of investigated ATLAS12 miniature sensors fabricated by Hamamatsu Photonics.

Type	Serial Number	Chip Name	Name
ATLAS12EC-P-SSSD	VPX22728 - W012	BABY (AC default P4)	W012 - P4
ATLAS12EC-P-SSSD	VPX22728 - W012	BABY (AC default P5)	W012 - P5
ATLAS12EC-P-SSSD	VPX22728 - W013	BABY (AC default P2)	W013 - P2
ATLAS12EC-P-SSSD	VPX22728 - W013	BABY (AC default P3)	W013 - P3

Table 5.2: Design specifications of the ATLAS12EC miniature sensors [40].

Parameter	**Unit**	**Value**
Maximum operation voltage	V	600
Wafer size ⌀	mm	150
Thickness	µm	310 ± 25
Outer dimension	mm × mm	10×10
Type		P
Strip implant		N
Number of strips		103
Length of strips	mm	8
Strip pitch	µm	74.5
Strip readout coupling		AC
Strip implant width	µm	16
Strip readout metal width	µm	20
Strip readout metal		Aluminium
Crystal Orientation		$< 100 >$
Ingot		Float zone
Resistivity	kΩ	>4
Strip bias resistor		Polysilicon
Strip bias resistance R_b	MΩ	1.5 ± 0.5
Strip AC coupling capacitance	pF/cm	> 20
Radiation tolerance	1-MeV n_{eq}/cm^2	$1.2{\cdot}10^{15}$

5.2 STRIDENAS Setup

The designed STRIDENAS detector aims at detecting electrons in an area of 2 cm × 1 cm with a spatial resolution in the 100 µm range and a dynamic range for incoming electrons between $\sim$ 10 – 234 000 electrons ($1.6{\times}10^{-3}$ fC – 37.5 fC) per 224 µm width. The different components of the setup are presented below.

Printed Circuit Board

The printed circuit board (PCB) was designed together with the ZE department at DESY. The layout for production of this board is shown in Appendix E. Basic parameters and components are listed below.

- Size: 127 mm x 140 mm
- Thickness: 1.5 mm

- 2 Layers
- 70 LEMO-00 connectors for signal readout (straight)
- 2 LEMO-00 connectors for high voltage supply
- 2 connectors for grounding of the LEMO-00 readout connectors
- 2 sets of bonding pads
- 2 sets of probing pads for testing the device at a probe station
- 4 grounding pads for the sensors
- 2 copper biasing plates
- 4 holes for possible mounting

Each bonding pad on the PCB is connected to one LEMO-00 connector. All LEMO-00 connectors for each sensor were brought to a common ground potential which can be accessed by the corresponding connector. The high voltage potential of the power supply LEMO-00 connector is connected to the respective copper biasing plate. The biasing plates are separated by 0.5 mm to enable independent biasing of the two sensors. One HV-pad for each connector allows high voltage supply, if the device is tested on the probe station. Four ground pads for each sensor are available. The pads are connected to the ground level of the power supply LEMO-00 connector. In addition, one probe ground pad per sensor is available for tests at the probe station.

A picture of the PCB is shown in Figure 5.3 and Figure 5.4. Due to the final implementation in ultra-high vacuum, it was refrained from implementing a signal amplifier on the PCB.

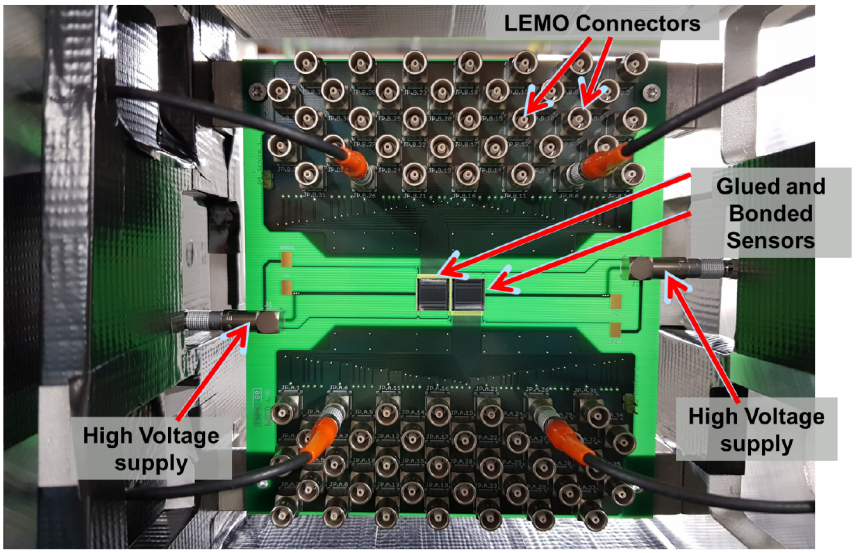

Figure 5.3: Picture of the printed circuit board hosting two ATLAS12EC miniature sensors. The sensors are bonded to the PCB and connected to LEMO-00 connectors for readout. The high voltage supply is provided on the sides of the PCB.

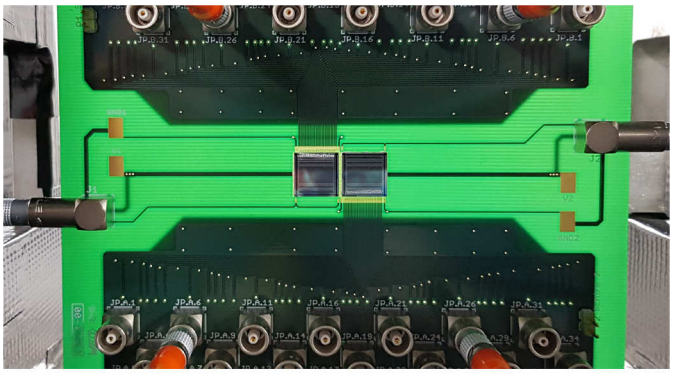

Figure 5.4: Zoom on the sensors bonded to the PCB.

Sensor Bonding

The sensors were glued to the PCB using a conducting silver epoxied glue (EPO-TEK H20E [46]) which is commonly used at DESY for the gluing of chips. The bonding of the sensors was done with a wire bonding machine. For the bonding of the sensor, three strips were connected to one readout channel. This was done for space and cost reduction of the readout on the PCB side (number of connectors) and on the electronics side (number of charge-to-digital converters). The two sensors were bonded individually to opposite sides on the PCB. The outermost strip was not bonded due to spatial constrains of the bonding machine. As a result, one of the bonding pads of each sensor as well as the corresponding connector remained unused. A sketch of the bonding diagram is shown in Figure 5.5. Each sensor is grounded by two wire bonds from the ground pads on the sensor to the ground pad on the PCB. Pictures of the bonds on the strips and bonding pads of the PCB are shown in Figure 5.6 and Figure 5.7, respectively.

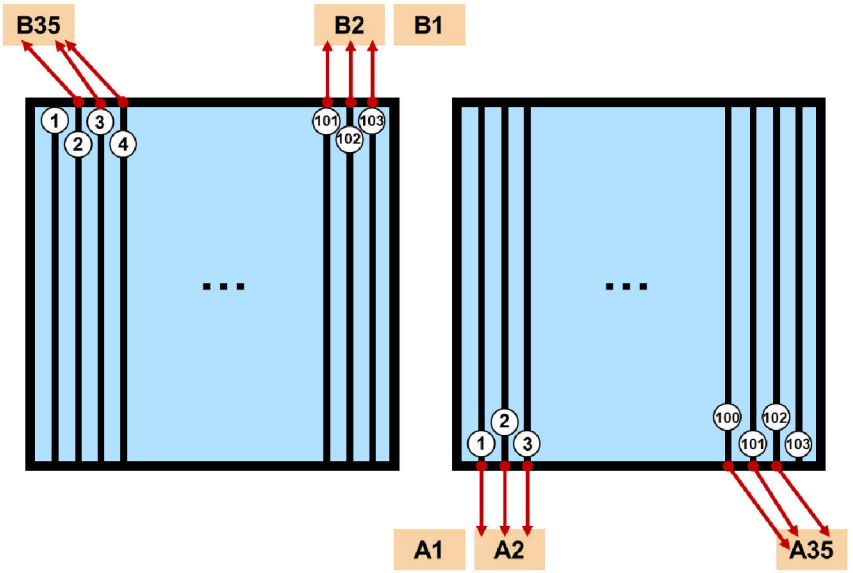

Figure 5.5: Bonding diagram for the sensors on the PCB. For each sensor 35 bonding pads were available. The names A1 to A35 and B1 to B35 correspond to the names of the LEMO-00 connectors to which the pads are connected. Three sensor strips were bonded to one pad. Due to spatial constraints pad A1 and B1 remained unused.

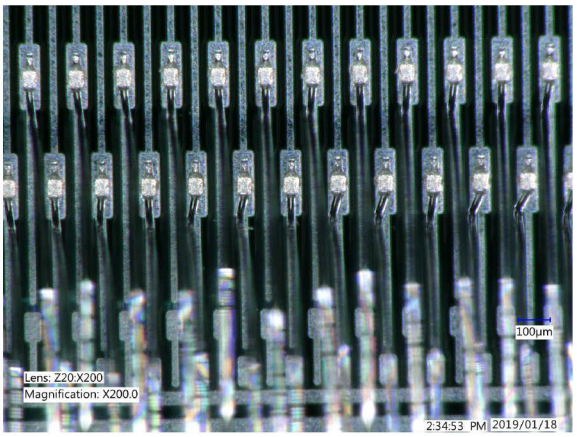

Figure 5.6: Microscopic picture of the bonding feet on the AC bond pads of the sensor.

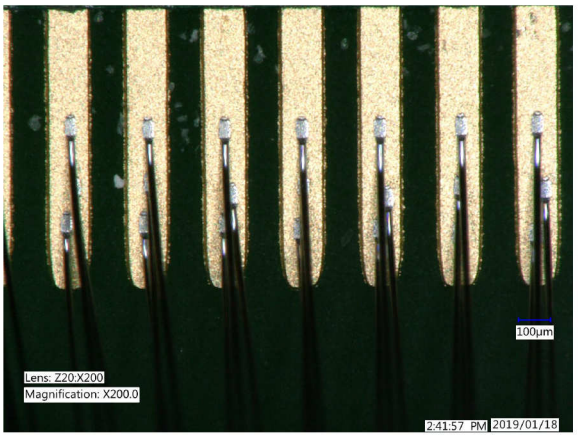

Figure 5.7: Microscopic picture of the bonds on the PCB.

PCB Holder

To mount the PCB, a dedicated PCB holder was designed within this thesis. It is made out of aluminium and consists of a ground plate and two side walls. For stability, the two sides are connected by a bridge. Each side wall has two brackets to which the PCB can be screwed. In addition, the side walls have three holes to enable the readout cable feed-through. An additional cover for light shielding for the top and sides of the holder can be screwed on the top bridge. The front and back of the PCB holder are open in order not to interfere with the electron beam. To shield the PCB from light, these sides can easily be closed with aluminium foil. The 3D model of the PCB holder is shown in Figure 5.8. A picture of the PCB holder containing the PCB is shown in Figure 5.9 and a side view is shown in Figure 5.10.

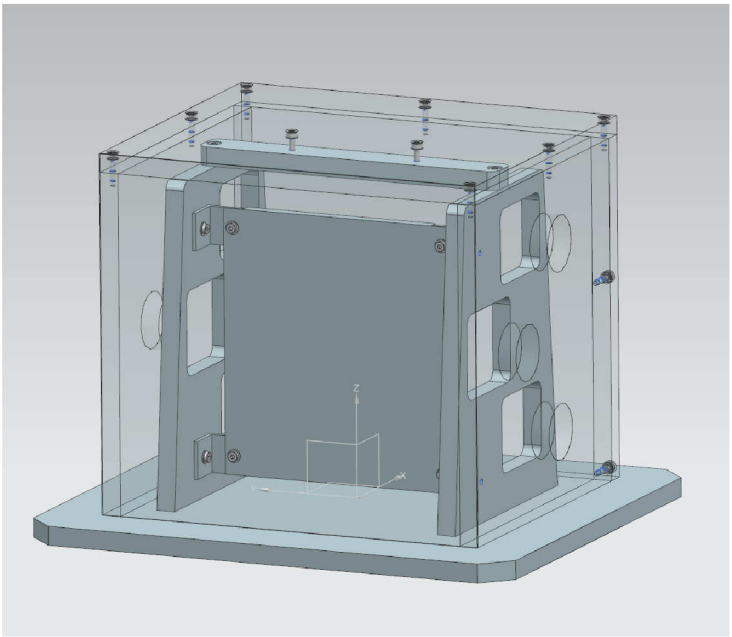

Figure 5.8: Technical drawing of the PCB holder. Courtesy: J. Stein

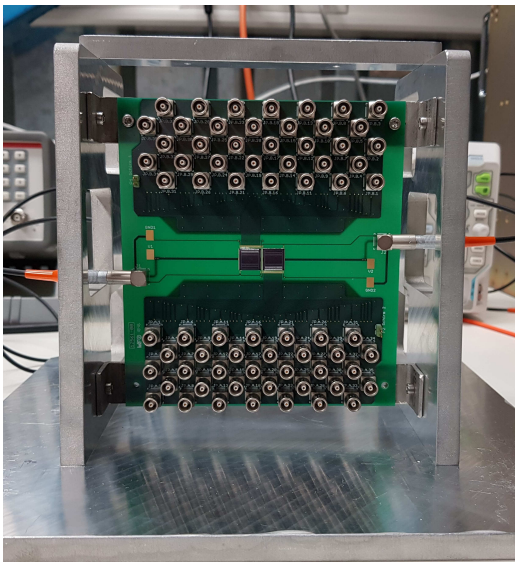

Figure 5.9: PCB holder with mounted PCB.

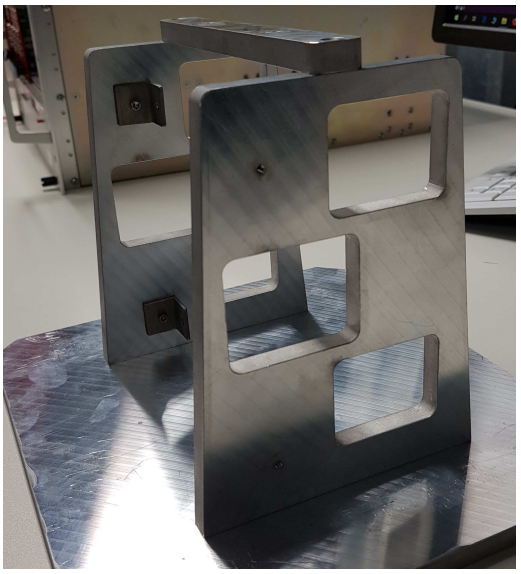

Figure 5.10: Side view of the PCB holder.

CAEN Charge-to-Digital Converter

For the spectrometer measurements, a large variation in charge density is expected and therefore a large dynamic range for the readout electronics is required. For the presented detector, the readout of the strip signal is performed by four charge-to-digital converters (QDCs) fabricated by CAEN. A picture of the device is shown in Figure 5.11. The QDCs V965 [47] have 16 channels, a 12 bit resolution and two simultaneous ranges to increase the dynamic range of the device. The specific parameters of the QDC V965 are listed in Table 5.3.

Table 5.3: CAEN V965 charge-to-digital converter parameters [47].

Parameter	**Unit**	**Value**
Range 1 / High range	pC	0 – 900
Range 2 / Low range	pC	0 – 100
Clear time	ns	600
Dead time	µs	6.9

The input charge of each channel of the QDC is converted to a voltage using a charge-to-amplitude converter (QAC). QAC signals are converted to a digital signal by two analogue-to-digital converters (ADCs) in parallel. These ADCs have two different gains, corresponding to the two different ranges of the QDC. The resolution depends on the number of bits since the voltage signal is divided into $2^{\mathrm{n}} - 1$ intervals. The minimum resolution is then given by the Least Significant Bit (LSB) as shown below:

$$1\ \mathrm{LSB} \mathrel{\widehat{=}} \frac{U_{\mathrm{max}} - U_{\mathrm{min}}}{2^n - 1}, \tag{5.1}$$

where U_{max} is the maximal voltage, U_{min} is the minimum voltage an n is the number of bits [12].

For range 1 (0 – 900 pC) the minimum resolution is 200 ± 20 fC [48] corresponding to around 1 248 300 electrons. For range 2 (0 – 100 pC), the minimum resolution is 25 ± 2.5 fC [48], which corresponds to about 156 000 electrons [49].

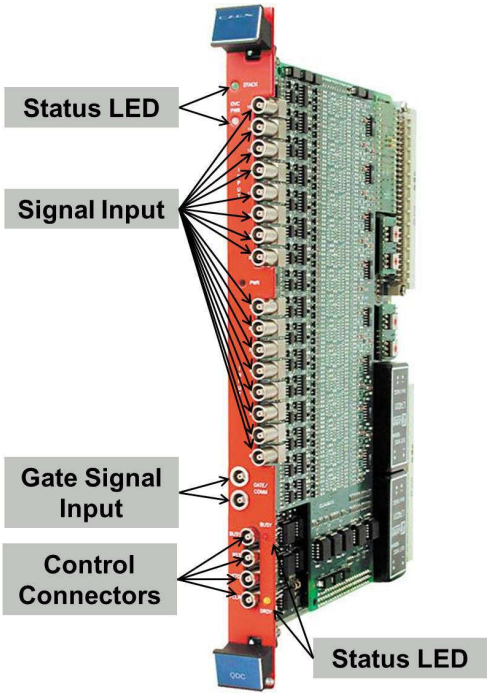

Figure 5.11: Picture of the CAEN V965 charge-to-digital converter [49]. 16 LEMO-00 signal inputs, two gate signal inputs and four control connectors are visible. LEDs to show the data acquisition status, the power status, the busy status and the data ready status are also implemented.

In order to start the charge measurement, the QDC requires a gate signal. The gate signal is common to all channels and is acting as the temporal window within which the input current is integrated. A sketch of the timeline of the gate signal and data acquisition is shown in Figure 5.12. This signal needs to be between -400 mV and -800 mV. Once this signal is received, the QDC starts the charge integration until the gate signal stops again. The gate signal length should be in the range of 30 ns to 900 ns in range 2 (0 – 100 pC) operation, and between 30 ns and 5 µs for range 1 (0 – 900 pC) operation to guarantee a linear behaviour. The repetition rate should be such that at least a 10 µs gap between gate signal is given, to take the dead time of the QDC into account. The gate signal can for example be delivered by an external gate generator or it can be built from a beam trigger signal.

The QDCs are placed in a VME crate as shown in Figure 5.13 and connected via an optical bridge (CAEN V2718 [50]) to a readout computer. The computer has a dedicated data acquisition software which allows the selection of different QDCs, some basic settings and the recording of the data for all 16 QDC channels. The diagram of the readout chain is sketched in Figure 5.14.

The signals from the sensor are transported from the PCB to the QDC via 2 m long HF 50 Ω LEMO cables (RG 174 POLYOLEFIN [51]). The cables have an attenuation of 29 dB /

100 m [51] when operated at 100 MHz which leads to an expected signal loss of approximately 6 % [52] for this setup.

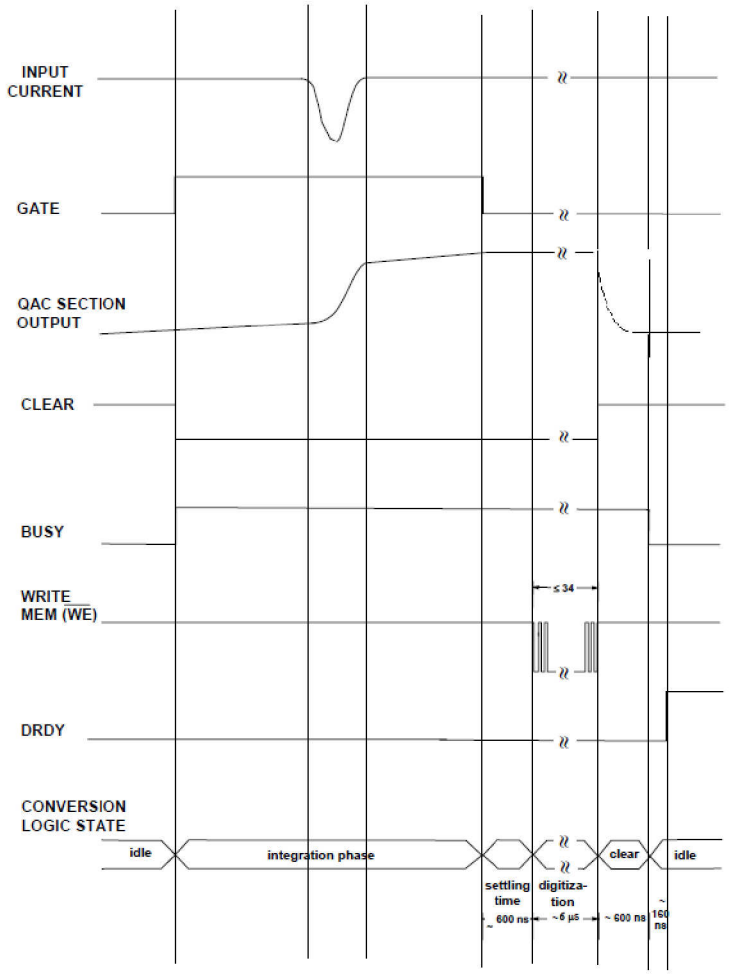

Figure 5.12: Sketch of the gate signal and data acquisition timeline [47].

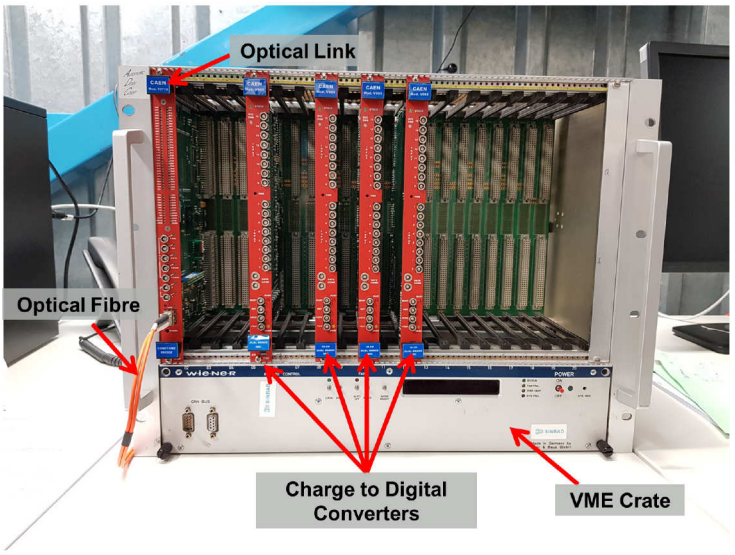

Figure 5.13: Picture of the VME crate containing the charge-to-digital converters and optical link.

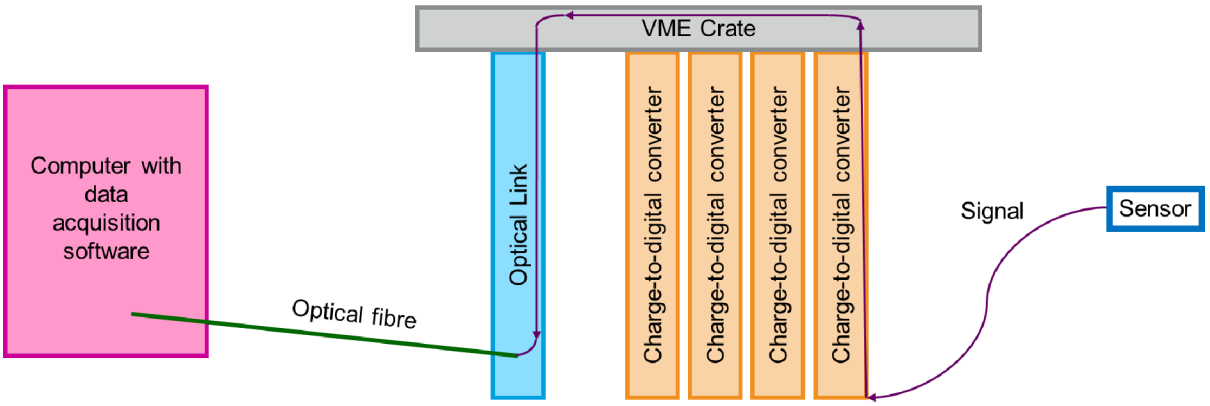

Figure 5.14: Diagram of the readout chain. The charge-to-digital converters are connected to and controlled by an optical link via the VME crate. The computer containing the data acquisition software is connected to the optical link via an optical fibre.

5.3 Simulation of Charge Sharing in Sensor

To estimate the behaviour of the sensor and the signal reaching the charge-to-digital converter, simulations were performed with a script, which was developed by using the ROOT [53] package. In these simulations, the influence of charge sharing between the single strips of the sensor was studied. An expected electron distribution at the position of the detector was produced by an ASTRA [54] simulation and fed into the ROOT script.

For simplicity, a random energy deposition of a minimum ionizing particle following a Landau distribution with the production of 80 electron-hole pairs per micron was assumed. In ROOT, the Landau distribution takes two input values: The most probable value of the distribution, which was set to the in average produced number of electron-hole pairs for a 310 µm thick sensor, and the scaling factor of the distribution, which is a measure for the spread of the function. This scaling factor was set to 8200 electron-hole pairs, which is based on values calculated in [55]. The charge sharing was modelled by a Gaussian distribution.

The structure of the script was as follows: First, the number of produced electron-hole pairs per incoming particle was determined by applying a random number generator to the Landau distribution. Each incoming particle has a given x position. The signal position was smeared out by applying the Gaussian spread. This signal was then filled into histogram bins, which correspond to the readout channels of the sensor. The whole process was repeated for each incoming particle. Charge thresholds of the readout electronics were applied at the end.

The incoming beam distribution simulated in ASTRA uses a macro charge for each particle in order to reduce the computing time. This means that each particle of the distribution corresponds to 312 electrons. In the sensor simulation this was taken into account by multiplying the average produced number of electron-hole pairs by 312. Therefore a simplified assumption of all 312 electrons producing the same number of electron-hole pairs was made.

The effect of incoming electrons not being perpendicular to the sensor surface was not taken into account. A lower threshold of the readout electronics was applied and set to twice

the minimum resolution of the 0 - 100 pC range of the QDC. An upper threshold given by the dynamic range of the charge-to-digital converters was applied. All simulation parameters are listed in Table 5.4.

First, a 1 pC ACHIP microbunching working point was studied. This distribution, however, created an amount of charge in the sensor which exceeded the upper threshold of the readout electronics. Therefore, an achievable ACHIP working point with 0.5 pC was chosen and is presented here. The parameters of the beam distribution are listed in Table 5.5. The distribution at the position of the STRIDENAS detector after the spectrometer dipole is shown in Figure 5.15 in x and y dimensions and in Figure 5.16 integrated over the whole y range. The bin size of this distribution was chosen to match the pitch of the STRIDENAS readout channels. The double horn structure appears due to the microbunching before the electron injection to the DLA. In case of acceleration in the DLA, a shift of this structure on the detector is expected and it is therefore needed to resolve this structure in the detector.

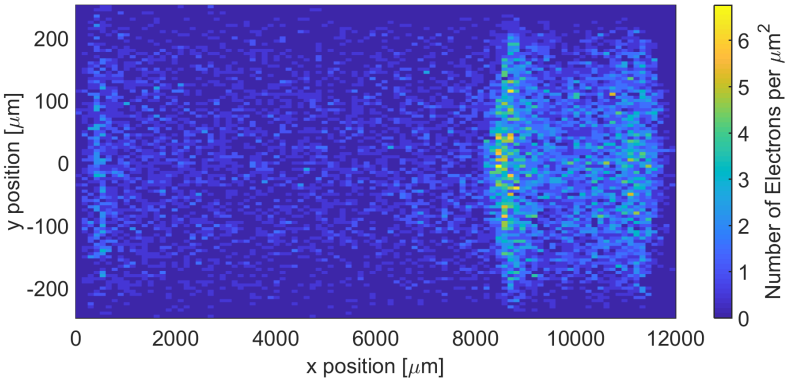

Figure 5.15: Electron beam distribution in x and y dimensions at the position of the detector for a 0.5 pC ACHIP microbunching working point. The number of electrons per µm^2 is displayed with a bin size of (120 × 5) µm^2.

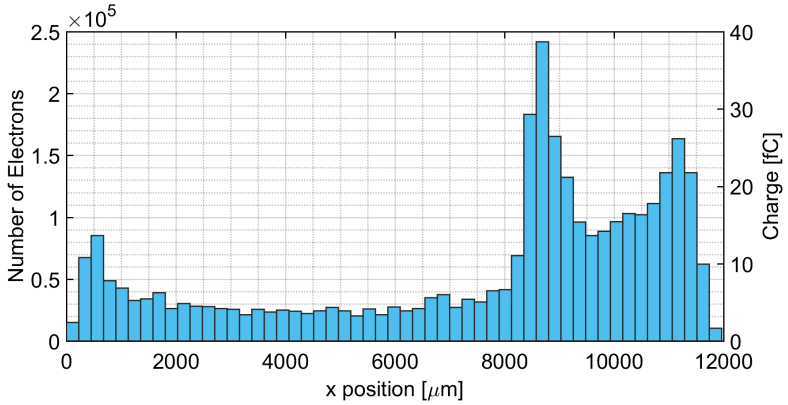

Figure 5.16: Electron beam distribution in x integrated over the whole y range at the position of the detector for a 0.5 pC ACHIP microbunching working point. A bin width of 225 µm was chosen to match the detector readout channel width.

Two charge sharing cases were considered. For a transverse movement due to thermal diffusion only, a Gaussian width of 4 µm was considered (see Section 2.2.5). The result is shown

Table 5.4: Charge sharing simulation parameters.

Parameter	**Unit**	**Value**
Generated electron-hole pairs per micron		80
Lower strip threshold	electrons	300 000 (2 × LSB of QDC)
Upper strip threshold	electrons	5 600 000 000
Width of Gaussian for charge sharing	µm	4 \ 300
Pitch	µm	223.5
Thickness	µm	310
Number of strips		64

Table 5.5: ASTRA beam distribution parameters.

Parameter	**Unit**	**Value**
Charge	pC	0.5
Energy	MeV	52
Full Bunch Duration	ps	5.6
σ_t	ps	1.2
Full Width on Screen Δx	mm	12
σ_x	mm	3.4
Full Height on Screen Δy	mm	0.5
σ_y	mm	0.1

in Figure 5.17. To estimate the impact of the plasma effect, a Gaussian width of 300 µm was chosen. This is an overestimated value oriented at measurements performed in [23]. The result is shown in Figure 5.18. Despite the assumption of a big transversal smearing of the signal, the beam features of interest, i.e. the double peak structure, are well resolved, as seen in channels 40 to 60. The expected spatial resolution of the sensor therefore seems to be sufficient for the desired position measurements.

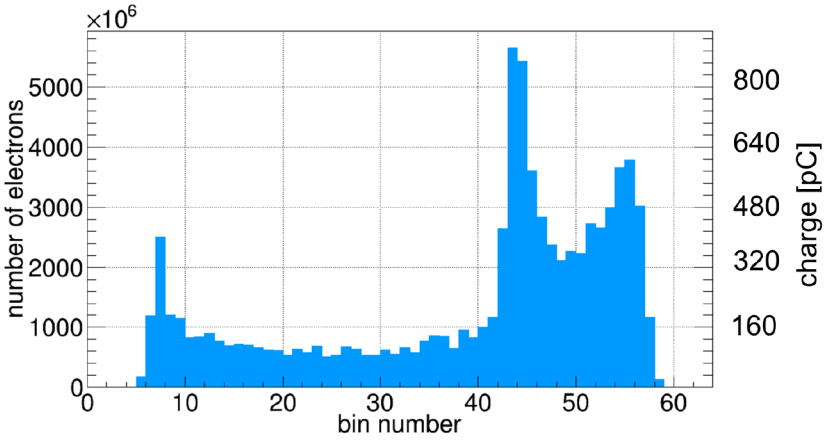

Figure 5.17: Charge sharing for a sensor of 310 µm thickness, 223.5 µm pitch and 64 readout channels with a Gaussian spread of 4 µm.

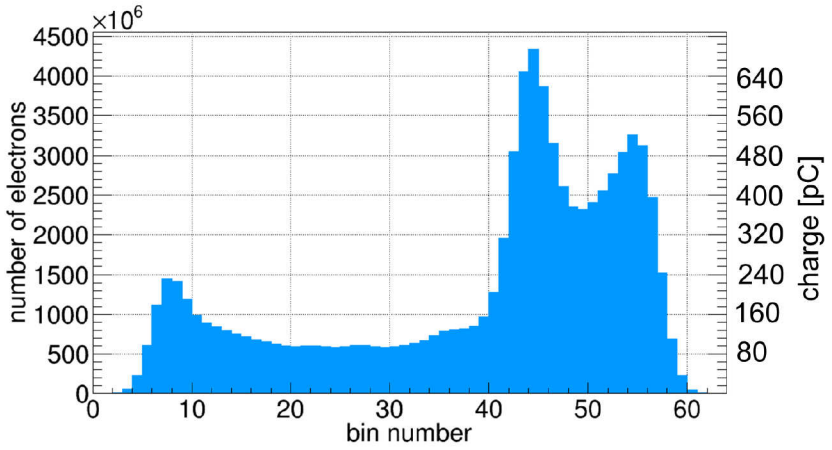

Figure 5.18: Charge sharing for a sensor of 310 µm thickness, 223.5 µm pitch and 64 readout channels with a Gaussian spread of 300 µm.

Chapter 6

Measurements of Sensor Properties and Functionality Tests

To investigate and study the parameters and behaviour of the ATLAS12EC miniature sensors, a series of measurements was performed. This includes measurements to obtain sensor specific properties as well as functionality tests of the STRIDENAS device. In addition, the third part of this chapter focusses on transient-current technique measurements. These measurements enable the investigation of the pulse shapes produced in the sensor under incoming laser light. Measurements with different intensities and bias voltages were performed.

6.1 Measurements of Sensor Properties

Current-voltage (IV) and capacitance-voltage (CV) measurements of the ATLAS12EC miniature sensors were performed. IV measurements provide information about the leakage current of a sensor as well as the tolerated operation voltage. CV measurements can be used to determine the depletion voltage of the sensor. Those quantities are essential for operation of the sensors and might differ from the values in the data sheet due to, for example, environmental influences. Measurements were performed at the probe station of the University of Hamburg. A Keithley 6517B [56] was used for the voltage supply and current measurements of the devices. For the capacitance measurements an Agilent E4980A LCR-Meter [57] was used which can be switched between the device under test and Keithley 6517B. A readout computer with dedicated software was connected to the measurement devices. All measurements were performed at 20 °C with a relative humidity below 10 %. A picture of the setup is shown in Figure 6.1.

To perform measurements, the device under test (DUT) was placed on the chuck of the measurement setup (Figure 6.2). The DUT is placed on a small hole in the chuck and can be fixed there with the help of a vacuum pump. A probe needle was connected to the ground pad of the device under test. For CV measurements, additionally an open measurement for calibration was performed. The open measurement is performed by disconnecting the ground needle from the DUT. To perform the measurements, a high voltage is applied to the chuck. A light-tight

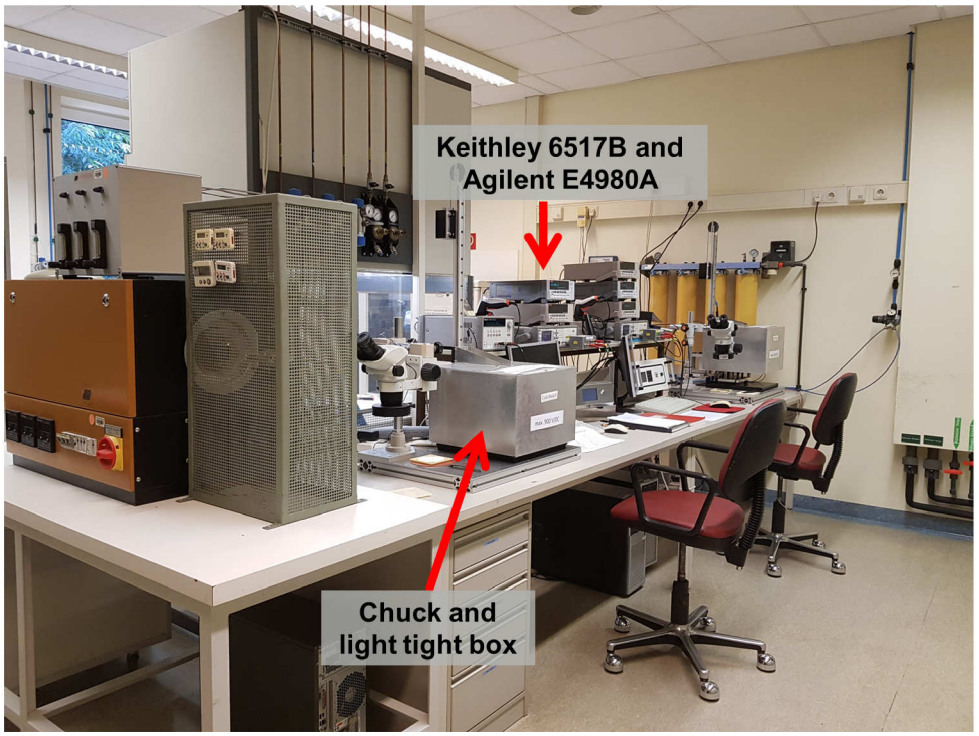

Figure 6.1: Picture of the probe station at the laboratory of the University of Hamburg.

Table 6.1: Results of current-voltage measurements.

Sensor Name	Unit	Leakage Current at 300V	Uncertainty
W012 P4	nA	−0.678	± 0.003
W012 P5	nA	−0.707	± 0.003
W013 P2	nA	−0.662	± 0.003
W013 P3	nA	−0.652	± 0.003

box can be placed on top of the setup. A picture of an ATLAS12EC miniature sensor placed on the chuck at the probe station is shown in Figure 6.2.

To ensure no breakdown of the sensor at the applied voltage occurs, the IV measurement was always performed first. For the IV measurements, a compliance limit of −1 µA was set as a safety measure. Once this current is reached, the applied voltage is ramped down automatically. The IV curves of all sensors are shown in Figure 6.3. It shows a leakage current at full depletion of about −0.7 nA. All measurement results and their uncertainties are shown in Table 6.1. The measurements were performed between −1 V and −350 V. From −1 V to −100 V a step size of 1 V was chosen, while from −100 V to −350 V a step size of 5 V was chosen. In a first test run, performed with the sensor W012 - P4, measurements were taken only up to −300 V. It was then manually checked at the Keithley device that the sensor also withstands a biasing of −350 V. However, in order not to risk any damage of the sensor, it was refrained from performing another full measurement. For the uncertainties of the Keithley 6487 on the current measurement, a range dependent uncertainty was applied. The values and corresponding ranges can be found in Table 6.2.

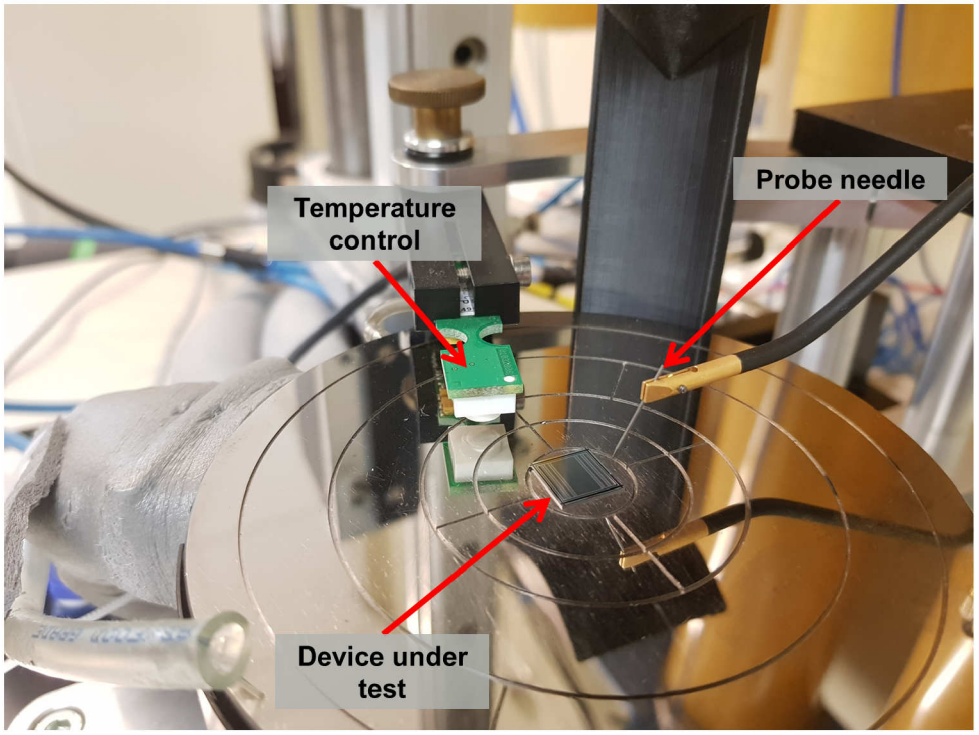

Figure 6.2: Picture of the sensor placed on the chuck for measurements at the laboratory of the University of Hamburg.

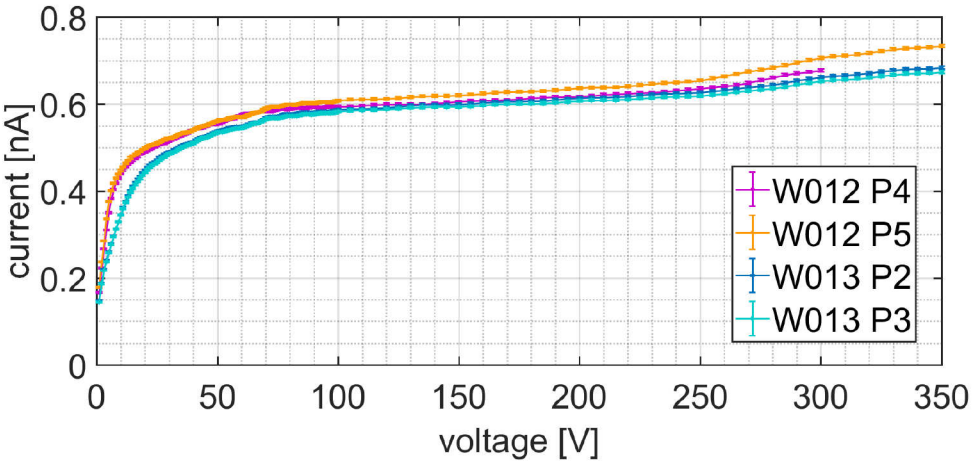

Figure 6.3: IV curves of all sensors. The measurements are displayed in absolute values.

Table 6.2: Range dependent uncertainties on current measurements.

Current Range [A]	Fractional Uncertainty on Current	Constant Uncertainty [A]
$< 2\times10^{-9}$	0.004	0.4×10^{-12}
2×10^{-9} - 2×10^{-8}	0.004	10^{-12}
2×10^{-8} - 2×10^{-7}	0.002	10^{-11}
2×10^{-7} - 2×10^{-6}	0.0015	10^{-10}
2×10^{-6} - 2×10^{-5}	0.001	10^{-9}
2×10^{-5} - 2×10^{-4}	0.001	10^{-8}
2×10^{-4} - 2×10^{-3}	0.001	10^{-7}
$> 2\times10^{-3}$	0.001	10^{-6}

Table 6.3: Results of capacitance-voltage measurements. Fitting range one: -60 to -260 V, range two: -300 to -350 V.

Sensor Name	Unit	Depletion Voltage	Uncertainty
W012 P4	V	-285.6	$\pm$ 2.8
W012 P5	V	-284.3	$\pm$ 2.8
W013 P2	V	-285.0	$\pm$ 3.1
W013 P3	V	-284.3	$\pm$ 2.9

The CV measurements were performed between -1 V and -350 V for all sensors with the same step sizes as for the IV measurements. The measured data for $\frac{1}{C^2}$ is shown in Figure 6.4. The bump in the linear rise of the curves at around -60 V occurs due to the geometry of the sensors. Measurements were taken without connecting the guard ring of the sensor since no guard ring probe pad is implemented in the structure. This however means that the edges of the structure are not well defined and that, at around -60 V, the active depleted area jumps, leading to this bump in the measurements. The not perfectly flat behaviour above -300 V can be explained by the differences to an ideal system of a parallel plate capacitor. The different layers on the backside of the sensor as well as in horizontal direction deplete further even when the sensor is already fully depleted. By plotting $\frac{1}{C^2}$ against the bias voltage, the depletion voltage of the sensor can be determined (see Equation 2.23). This is done by taking the intersection of the linear rise and constant line of the measurements. The obtained depletion voltages for all sensors are listed in Table 6.3. The results show a uniform behaviour of the sensors, which exhibit the same depletion voltage within the uncertainty range. The fit to determine the depletion voltage for sensor W012 - P4 is shown in Figure 6.5 and was applied between -60 V and -260 V for a linear fit 1 and between -300 V and -350 V for a linear fit 2. The measurement uncertainties of the Agilent E4980A on the capacitance measurement at 10 kHz is 0.2% [57].

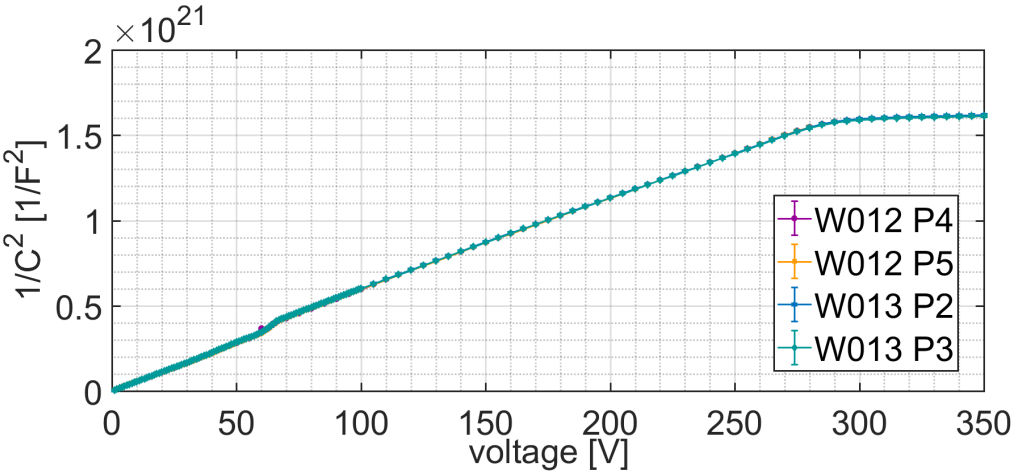

Figure 6.4: CV curves of all sensors. The measurements are displayed in absolute values.

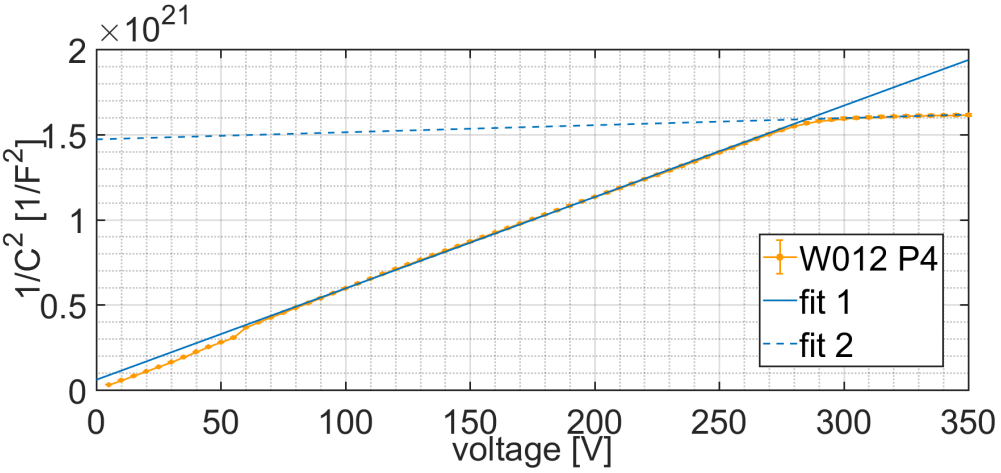

Figure 6.5: CV measurement for W012 - P4. The depletion voltage for this sensor is obtained by taking the intersections of the displayed fit curves.

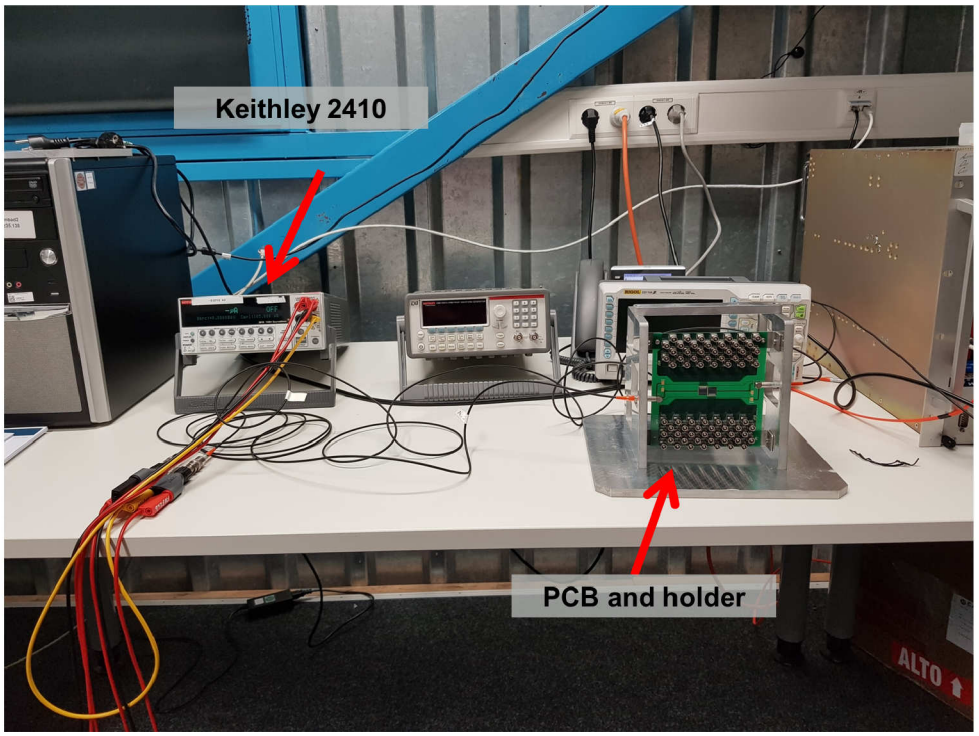

Figure 6.6: Setup for functionality test of the bonded sensors.

6.2 Functionality Tests of Bonded Sensors

The current-voltage and capacitance-voltage measurements presented in Section 6.1 were performed before the sensors were glued and bonded to the PCB. Before starting measurements with the STRIDENAS detector, the sensor behaviour was investigated again.

For a first check of the bonded sensors on the PCB, the PCB with the sensors was placed in the PCB holder. A Keithley 2410 [58] power supply was used to bias the sensors and measure the current. The accuracy of the current measurements is stated as 0.029 % of the reading value + 300 pA [58]. The power supply was first tested up to -300 V. Then the cables were connected to the PCB and a voltage of -0.5 V applied. A current of -10 nA was measured. Although the room was darkened, no light tight box was placed over the sensors, which can explain the discrepancy between the observed current and the current measured at the probe station. When the voltage was increased in 1 V steps to -50 V it settled at around -100 nA, not changing much over the last 30 voltage steps. A picture of the setup is shown in Figure 6.6.

For a more detailed test, IV curves with the same setup were measured. In addition, a cardboard box was placed on top of the holder and ambient light was shielded with black plastic foil as shown in Figure 6.7. Still, all lights were switched off during the measurements. The results of the measurements are shown in Figure 6.8.

Run 1 refers to the first recorded IV curve after the bonding of the sensors. An early breakdown starting at around -85 V can be observed. Such an early breakdown might indicate a damage of a sensor or problems with the readout like a short circuit of the PCB or badly placed bonds. It was suspected that it might occur due to surface charges which accumulated

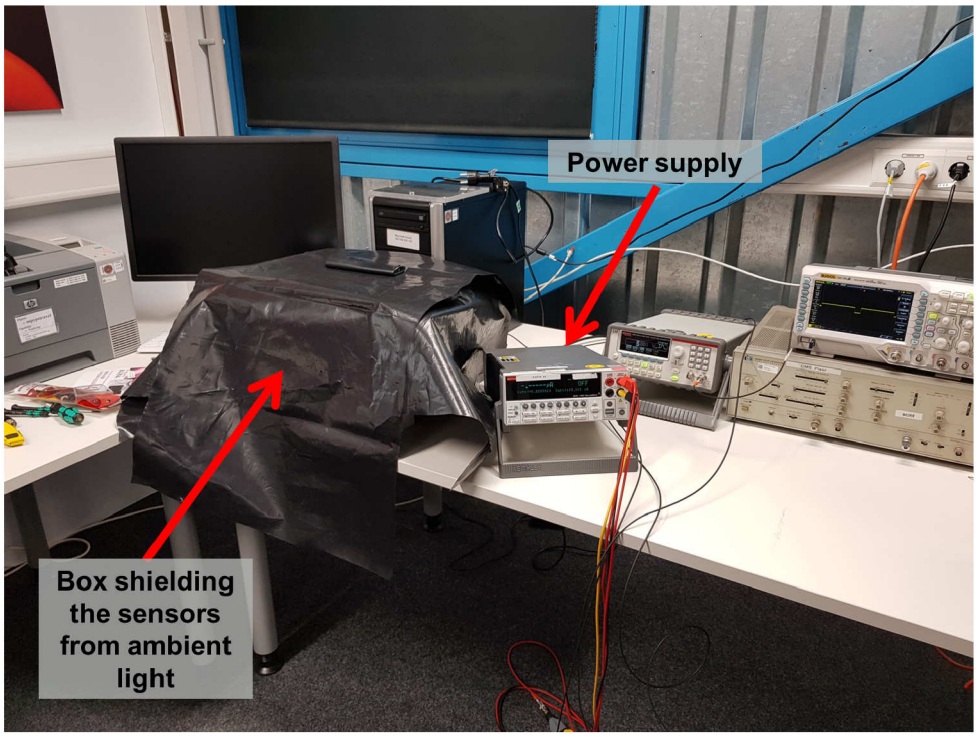

Figure 6.7: Setup for IV curve measurements in darkness.

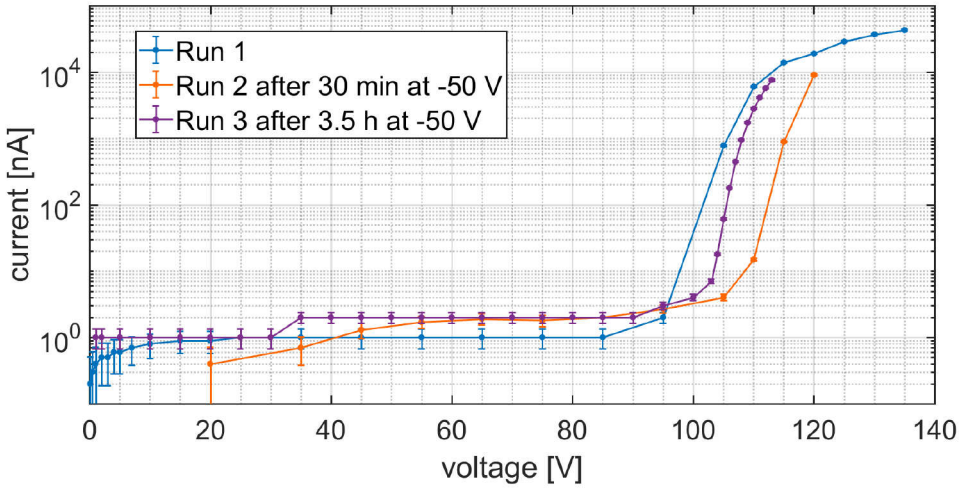

Figure 6.8: IV curves of bonded sensors measured in darkness. The measurements are displayed in absolute values.

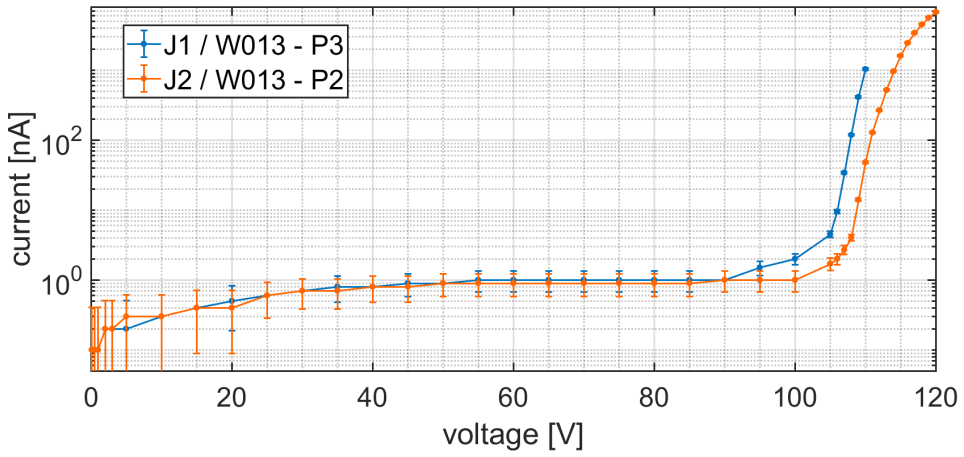

Figure 6.9: IV curves of bonded sensors measured separately. Measurements were performed in darkness. The measurements are displayed in absolute values.

on the sensor while glueing, bonding or storing the sensor. To get rid of these possible surface charges, the sensors were set to -50 V for 30 minutes. Another IV curve, referred to as run 2, was recorded. A shift for the breakdown voltage to about -105 V can be observed. To check if further improvements are possible, the sensors were again set to -50 V for 3.5 hours and the next IV curve referred to as run 3 was recorded. However, no improvement of the breakdown voltage was observed.

The recorded current is a superposition of the currents from the two sensors. It is therefore possible that the early breakdown of the detector occurs even if only one of the two bonded sensors is damaged. To check for any differences between the two sensors on the PCB, IV curves for each sensor were recorded separately. The measurements were done by connecting only one sensor to the high voltage while the other sensor was floating without grounding. The two IV curves can be seen in Figure 6.9. The J1 and J2 indicate to which power supply the sensors were connected to on the PCB. No clear difference in their behaviour is visible. To ensure that the two power circuits on the PCB are separated, a duplicate of the PCB was investigated. No sensors were mounted on this PCB. It was only supplied with one LEMO-00 connector for power supply. A high voltage was applied to that PCB and it was confirmed that the two biasing circuits are well separated. The early breakdown of the detector therefore seems to be a common problem to both sensors, the wire bonding or the gluing of the sensors and does not seem to arise due to the design of the PCB.

The light tightness of the box and the response of the sensors to light was tested. A voltage of -60 V was applied to the two sensors. For a current of around -1 nA, a variation of the value of $\pm$ 0.5 nA was observed. This variation is bigger than the intrinsic uncertainty of the Keithley device. The measured current for different light settings are listed in Table 6.4. The sensor strongly responded to incoming light. This indicated that, at the time of the measurements, despite the early breakdown, the sensors might still be able to detect particles in an experiment.

Table 6.4: Results of light tests on sensor.

Parameter	**Unit**	**Value**
Light off, full covering	nA	-1 ± 0.5
Full light, full covering	nA	-1 ± 0.5
Full light, black foil removed	nA	-8 ± 1
Full light, cardboard box slightly lifted	nA	-1000 ± 29

IV and CV Measurements of Bonded Sensors

To cross-check that the early breakdown of the detector occurs not only due to environmental effects and the measurement setup, current-voltage and capacitance-voltage measurements of the bonded sensor in the laboratory were performed. For the measurements, the PCB with the sensors was placed on the chuck of the probe station. The high voltage supply was done via a probe needle. It was connected to the high voltage probe pad implemented in the PCB design. The ground was set via a probe needle on the ground probe pad on the PCB. Both sensors on the PCB were tested separately. The recorded IV curves are shown in Figure 6.10. Here, also the early breakdown for both sensors is visible. The CV curves are shown in Figure 6.11. Up to the breakdown voltage, the behaviour of these curves looks normal. When comparing to the measured CV curves of the unbonded sensors (Figure 6.4) a shift of the curves can be observed. However, the measurements performed with the bonded sensors are lacking an open measurement for calibration due to the risk of sparks in the probe station (Appendix B). The shift of the curves therefore might only occur due to different calibrations.

Despite the observation of the early breakdown of the sensors, it was decided to test the STRIDENAS detector at the DESY II Test Beam. The results are presented in Chapter 7.

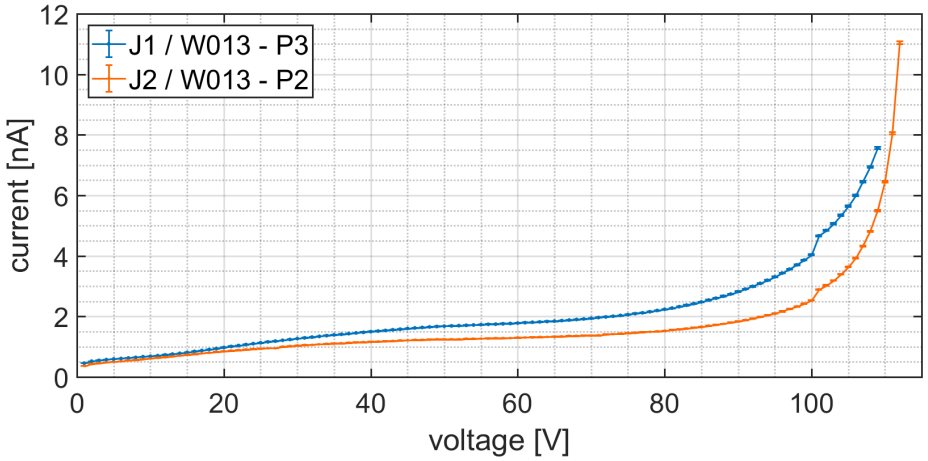

Figure 6.10: Current-voltage measurement of the bonded sensors at the probe station. The measurements are displayed in absolute values.

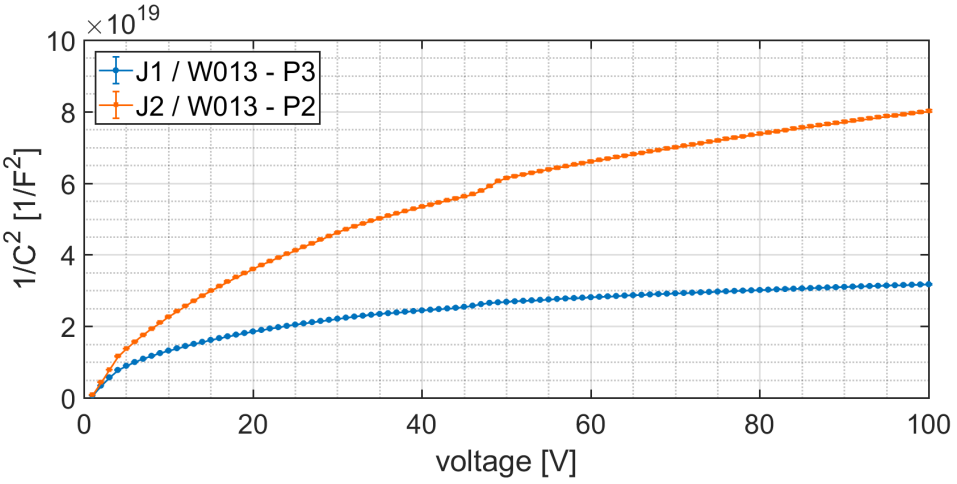

Figure 6.11: Capacitance-voltage measurement of the bonded sensors at the probe station. The measurements are displayed in absolute values.

6.3 Transient-Current Technique Measurements

At ARES, more than 80 000 electrons per sensor strip can be expected. However, the investigated ATLAS12EC miniature sensor was originally developed for single particle detection. Therefore, the performance under high-intensity electron beams needs to be determined. At DESY, no high-intensity electron beams with the necessary infrastructure or accessibility were available for these measurements. However, as described in Section 2.2.3, electron-hole pairs can also be produced by incoming photons. Therefore, a laser pulse can be used to estimate the effect of a high-intensity electron beam.

Measurements of this effect were performed by using the transient-current technique (TCT). In this procedure, the sensor is hit by a laser pulse, generating electron-hole pairs inside the sensor. The induced signal under an applied reverse bias can be read out and analysed. From these measurements, information about the signal length and transverse spread for a given laser intensity can be extracted. For our studies this was of particular interest, since a high incoming electron intensity can induce an undesired plasma effect in the sensor (Section 2.2.6) which leads to an increase of signal length as well as transverse spread. The TCT measurement therefore allows for an estimation of its impact.

Furthermore, the correlation between the applied bias voltage at the sensor and produced charge inside the sensor can be studied. This behaviour was investigated since the dynamic range of the readout electronics is limited by an upper charge threshold which could be reached in some cases. To explore if a charge reduction in the sensor is possible and beneficial, measurements at different bias voltages were of interest.

Measurement Setup

The TCT measurements were performed at the laboratory of the Detector Development group from the University of Hamburg. The setup is shown in Figure 6.12 and 6.13, and a more de-

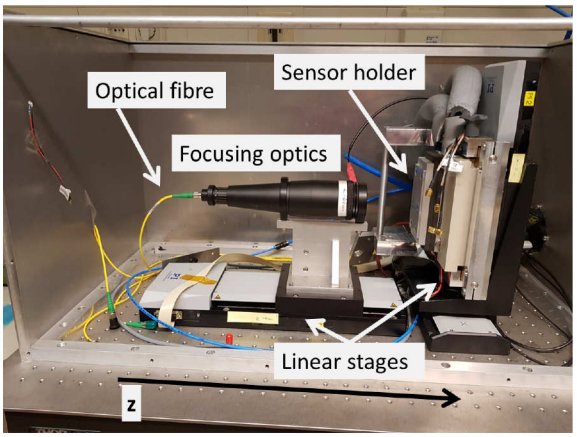

Figure 6.12: Inside of the experimental box used for the TCT measurements.

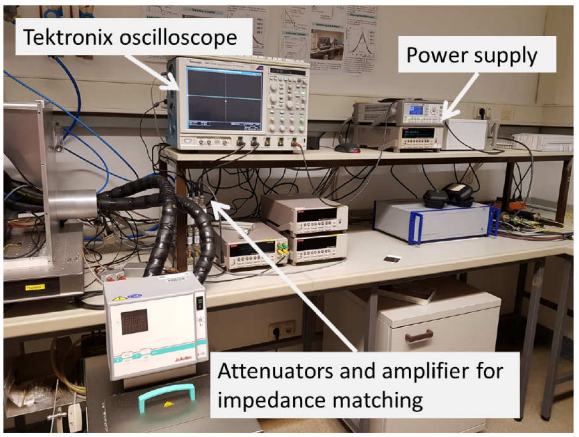

Figure 6.13: Setup for the TCT measurements.

tailed description can be found in [59]. Different wavelengths of the laser light are available. For the following measurements a (660 $\pm$ 2) nm and a (1015 $\pm$ 6) nm wavelength were considered. The energy of the red laser beam is deposited in the sensor within the first µm and therefore enhances the impact of the plasma effect. The infrared wavelength has a larger attenuation length and therefore this laser beam penetrates the whole sensor thickness, making those measurements comparable with incoming minimum ionizing particles.

The generated laser light is guided into the experimental box via optical fibres. An optical focusing system is implemented and mounted on a linear stage with a step size of 0.1 µm and a precision of 0.03 µm. It can be moved in the laser beam direction and therefore enables focusing of the laser beam onto the sensor.

For the measurements, the sensor under test has to be mounted on a PCB, which can be attached to the setup as shown in Figure 6.14. The setup allows for two strips of the sensor to be bonded to the PCB and connected to readout cables. Neighbouring strips are grounded. The bonding diagram for the ATLAS12EC miniature sensor W012 - P4 is shown in Figure 6.15. The sensor is held onto the PCB via a plastic strip. High voltage for depletion of the sensor is delivered via a copper backplate.

The linear stages, which the PCB can be mounted to, have a minimal step size of 0.05 µm and a precision of 0.02 µm to enable movements in both perpendicular planes to the laser beam. The strip signals are guided out of the experimental box and pass through an attenuator. The attenuator is used to allow for a high dynamic range and to match the impedance of the cables and amplifiers [60]. An RF-limiter is used to protect the following components from voltage spikes. A fast amplifier is used and the signal recorded by an oscilloscope. The bias voltage, linear stage positions, laser intensity and measurement steps can be controlled by software programs on a PC.

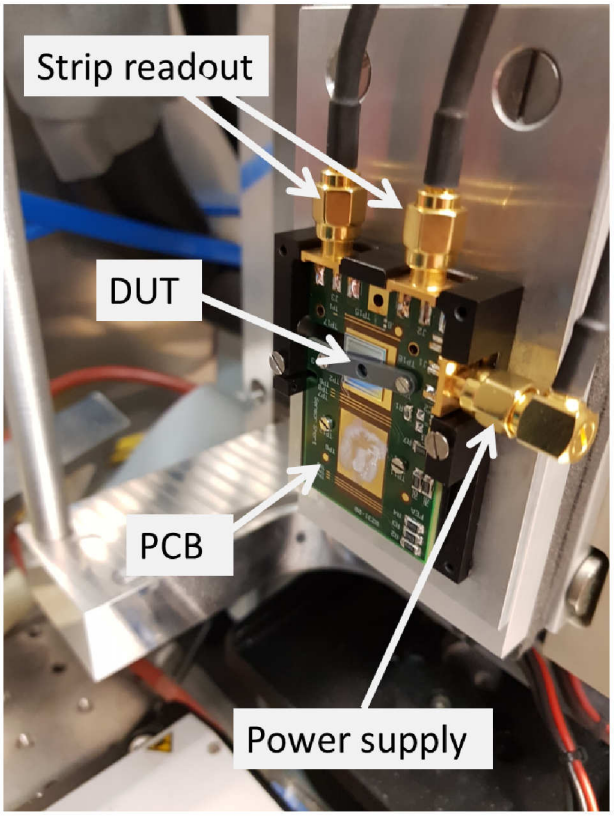

Figure 6.14: PCB and sensor mounted for TCT measurements.

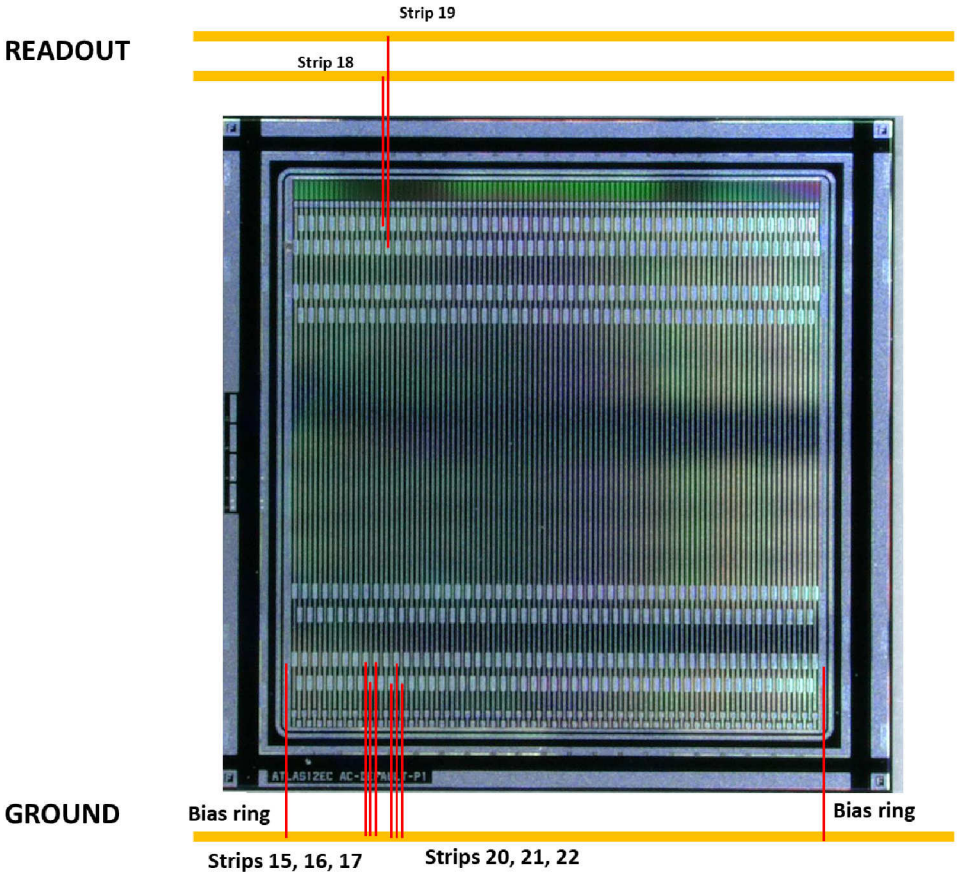

Figure 6.15: Bonding diagram of the ATLAS12EC miniature sensor for the TCT measurements.

TCT Measurements

For the measurements the ATLAS W012 - P4 sensor was used. The sensor depletes at around -286 V (see Table 6.3). Measurements with two different lasers were performed. The first laser has a wavelength of 660 nm, the second laser lies in the infrared with 1015 nm. The optics of the setup are designed such that the laser beam can be focussed. The minimum spot size was measured in [59] to be about 3 µm.

Before starting the measurements, the laser beam needs to be focused and aligned. In a first step, the red laser spot was placed on the connected strips visually. Therefore, a defocussed (big) laser light spot was used and it was seen where this spot hits the sensor. In a second stage, an online analysis of the produced sensor signal on the oscilloscope was performed. The box of the experimental setup was closed and a bias voltage applied to the sensor. Then, if the laser light spot is placed on one of the connected strips of the sensor, a signal is visible on the oscilloscope. The relative position of the sensor to the laser light in x and y was varied, until the signal amplitude was maximal. Then the distance of the laser optics to the sensor was changed until the signal amplitude was minimal, corresponding to a smaller spot size of the laser beam. Again, the position of the sensor in x and y were varied until the signal amplitude was maximal. This procedure was repeated until the maximal signal was found. The last stage to find the laser light focus was an automated scan series. Controlled by the computer software, the linear stages were moved in x and z direction and the generated signal was recorded. By looking at the position-dependent signal strength, the position for the laser light focus can be determined and the laser optics placed in the corresponding z position.

For the first measurement campaign, the red laser at 660 nm was used. For bias voltages between -140 V and -300 V in 20 V steps, the signals of the two strips were measured at different x positions of the laser. Therefore, the laser was moved over the strips in 1 µm steps over a range of 250 µm.

Multiple measurements were performed. The first one at a low laser intensity as a reference measurement and the second one at full laser intensity. As previously mentioned, red light has an attenuation length of ~ 3 µm and therefore only penetrates a few µm into the sensor and deposits all the energy in this volume. A second measurement campaign was done using the 1015 nm laser light which has an attenuation length of ~ 250 µm. The attenuation length of this wavelength is much bigger and the light therefore penetrates through the whole depleted sensor volume. The same bias voltage settings and x position ranges as for the measurement with the red laser light were chosen. Again, one measurement with low intensity and one measurement with full laser intensity were performed.

A calibration for the laser light intensity or measurement devices for the laser spot size was not available. Therefore, only a comparison between low and high intensity is possible but no information about the number of photons on the sensor per area is known.

TCT Data Analysis

For the analysis of the measured TCT data, TCTAnalysis was used. This tool is a shared library based on ROOT and the ROOT interpreter CINT dedicated to TCT analysis. It was adapted to the specific measurement setup presented above. The recorded data is stored in ASCII files and read into histograms. Individual parts of the analysis are organised in macros. A macro to find the laser light focus was available, macros to obtain the produced charge in the sensor depending on the laser light position and laser light intensity as well as macros to obtain the produced charge in the sensor for different applied bias voltages were adapted from already existing functions.

The stored data contains the oscilloscope traces of the measured transient current pulses, which are also called waveforms. To obtain the produced charge in the sensor, the integral of the corresponding waveform is calculated. Each waveform has a baseline with an offset which is always corrected before calculations are performed. This is done for each pulse individually by integrating the pulses in an area with no signal. The integral is then divided by the number of bins and subtracted from the waveform.

The sensor pulse is recorded for 100 ns. The signal strength is measured in volts and converted into a current using

$$I = V_m \frac{\alpha^{1/2}}{100 \cdot 50\Omega}, \tag{6.1}$$

where V_m is the measured voltage, α the 10 dB attenuation of the setup, the factor 100 the amplification by the amplifier and the 50 Ω the impedance of the circuit. Each recorded waveform is the average of 1024 waveforms.

Results

To illustrate the differences in waveforms recorded with low and high laser light intensity, an example for a laser light spot position close to the centre of a connected strip of the sensor is shown. For red laser light, the waveforms are shown in Figure 6.16 and Figure 6.17 for low and high intensities, respectively. An increase of the signal amplitude for the high intensity measurement can be observed. The pulse length of the high intensity measurement increases. This can be explained by the plasma effect described in Section 2.2.6. Due to a high number of photons being absorbed in the first few µm of the silicon, a high charge carrier density is present. This delays the readout process and leads to the change of the pulse shape.

The waveforms for the infrared laser light measurements are shown in Figure 6.18 for low intensity and in Figure 6.19 for the high intensity. As for the red laser light measurements, an increase of the amplitude and pulse length can be observed with increasing laser light intensity. The increase of pulse length is not as strong as for the red laser light. This can be explained by different laser intensities and the different attenuation of infrared laser light. The electron-hole pairs are created over the whole thickness of the sensor and therefore the charge carrier density in the sensor is smaller than for the red laser light measurement.

The increase of the pulse length is not expected to cause problems with regards to the read-

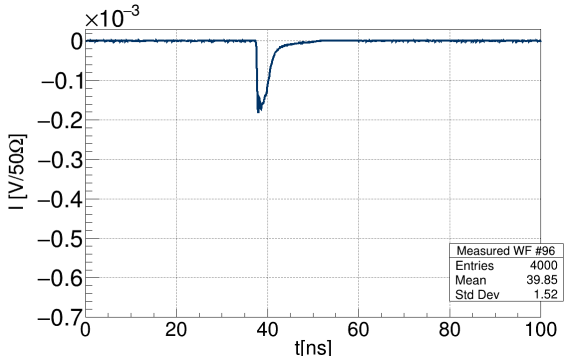

Figure 6.16: Recorded waveform for a red laser light and low intensity at $x = 48$ µm.

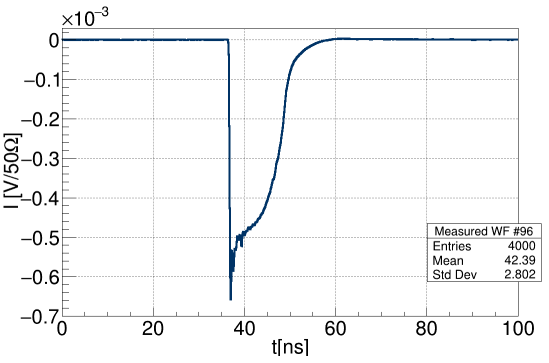

Figure 6.17: Recorded waveform for a red laser light and high intensity at $x = 48$ µm.

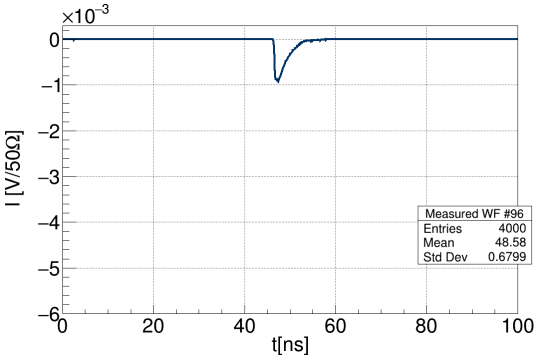

Figure 6.18: Recorded waveform for an infrared laser light and low intensity at $x = 48$ µm.

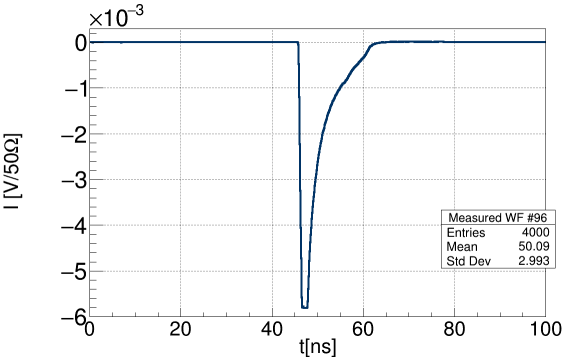

Figure 6.19: Recorded waveform for an infrared laser light and high intensity at $x = 48$ µm.

out of the STRIDENAS detector. The observed pulse lengths of maximal $\sim$ 20 ns for a bias voltage of -300 V are well below the incoming electron repetition rate of 50 Hz and the signal integration time between 30 ns to 1 µs.

By integrating the measured current over the signal length, the total charge produced in the sensor can be obtained. This was done for different laser positions for the low and high intensity measurements. The results for the red laser light are shown in Figure 6.20 and the results for the infrared laser light in Figure 6.21. The integration time was set to 45 ns to accommodate both small and wide wavefunctions. In both plots, a strong reduction of the signals at $x \approx 65$ µm and $x \approx 140$ µm can be seen. This arises due to the metallic layers on the sensor strips. The laser light is unable to penetrate this material and therefore no signal can be observed at these positions. When looking at the distances between the minima, it can be seen that it agrees well with the strip pitch of $\sim$ 75 µm listed in the sensor specifications.

In Figure 6.20, an increase of the collected charge close to the strip metallization can be seen. This increase might occur due to light reflection on the strip metalization [23]. By looking at the laser position scans, the charge sharing between two neighbouring strips can be observed. When the laser light enters the sensor in the middle of two strips, both channels produce the same signal. If the laser moves towards the middle of one channel, a signal is still induced on the neighbouring strip. The radius of the laser beam w_0, which also determines the position resolution of this measurement, was estimated with $\sim$ 6 µm and was measured in [59]. It was not possible to cross-check the spot size for our measurement since the required equipment was not available. In addition, the exact behaviour of the signal is hard to extract since the signal information at the position of the strip metallization is missing. With a distance of 85 µm from the strip centre, the signal has already dropped significantly. After a distance of 135 µm, no more signal is observed on the strip for the measured laser light intensity. Keeping in mind the readout channel pitch of 223.5 µm for the STRIDENAS detector, no problems due to transverse spread below this charge carrier density are expected.

To investigate the effect on the produced charge and signal shape for different bias voltages of the sensor, a position scan at different bias voltages for high laser light intensity were performed. The results are shown in Figure 6.22 for the red laser light and in Figure 6.25 for the infrared laser light. For the red laser light, no differences in the peak produced charge can be observed. A zoom at the peak for channel 2 is shown in Figure 6.23. This is expected since the laser light only enters the first few µm of the sensor. A p-type sensor operated at a bias voltage below the depletion voltage results in an undepleted area at the bottom of the sensor. For the thickness of the laser light penetration, no change in depletion area occurred.

When looking at the slope of the signals (Figure 6.24), a difference can be seen. Signals from low bias voltage measurements spread out more compared to the measurements with high bias voltage. This can be explained by the strength of the electric field created by the bias voltage. When operating at a lower voltage, the electric field decreases accordingly. The charge collection time depends on the doping concentration only, when the sensor is operated under-

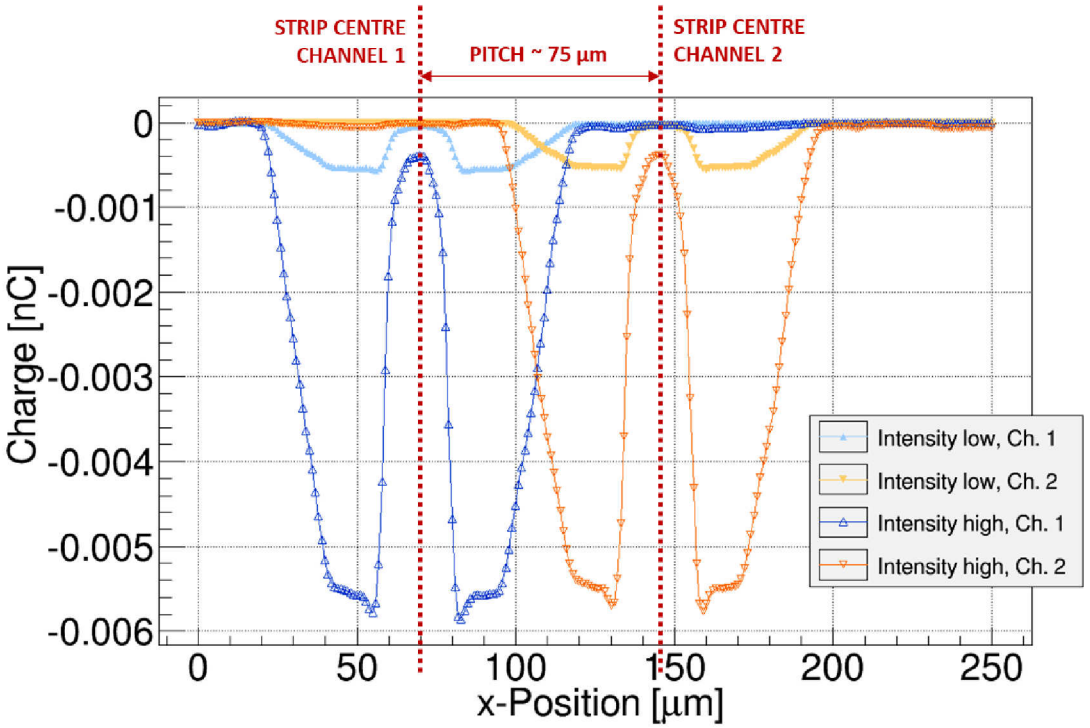

Figure 6.20: Position scan for red laser light and low and high laser intensities.

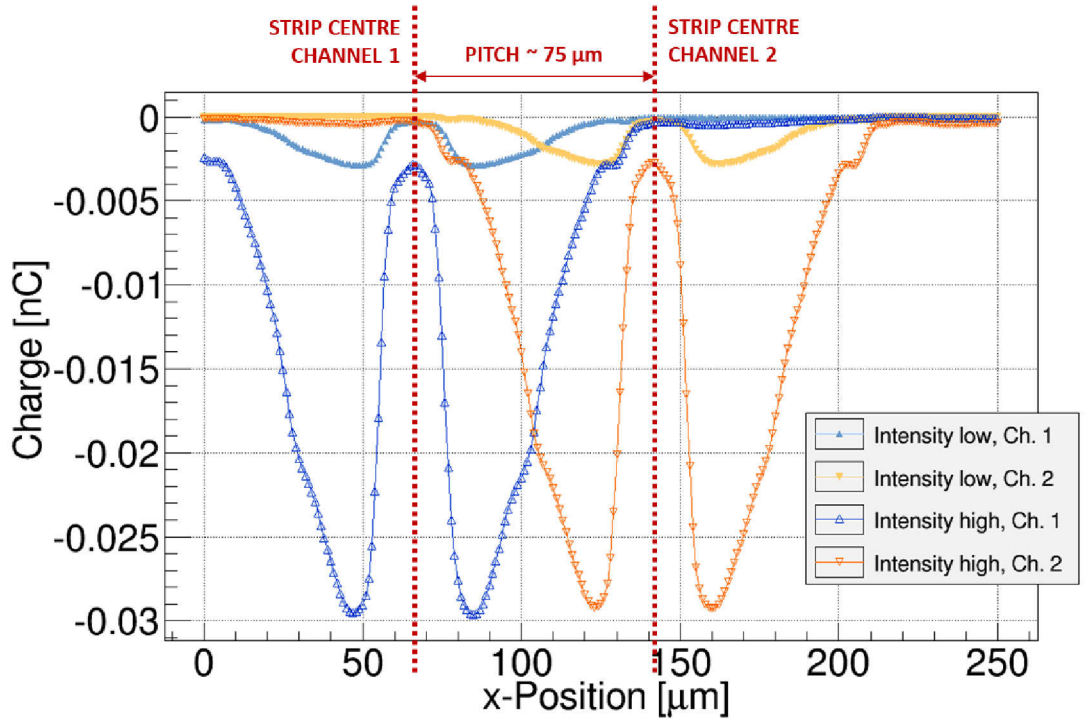

Figure 6.21: Position scan for infrared laser light and low and high laser intensities.

depleted. This might lead to a longer charge collection time and therefore a stronger transverse spread due to thermal diffusion. Additionally, the strength of the electric field influences the plasma effect in the sensor, as it works against the shielding of the charge carriers in the sensor.

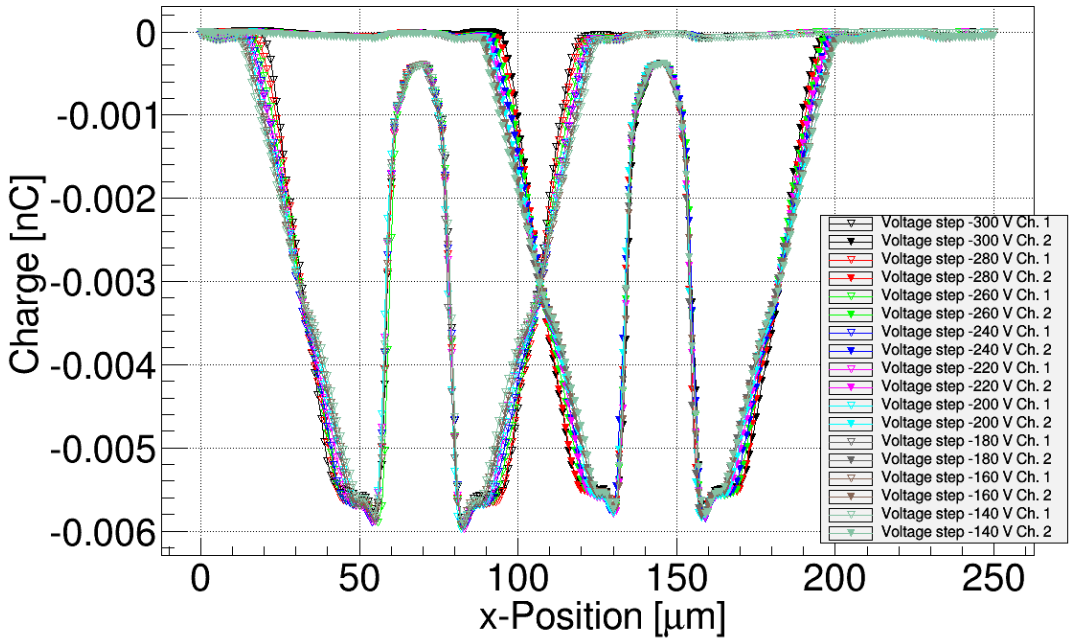

Figure 6.22: Position scans for different bias voltages and high intensity red laser light.

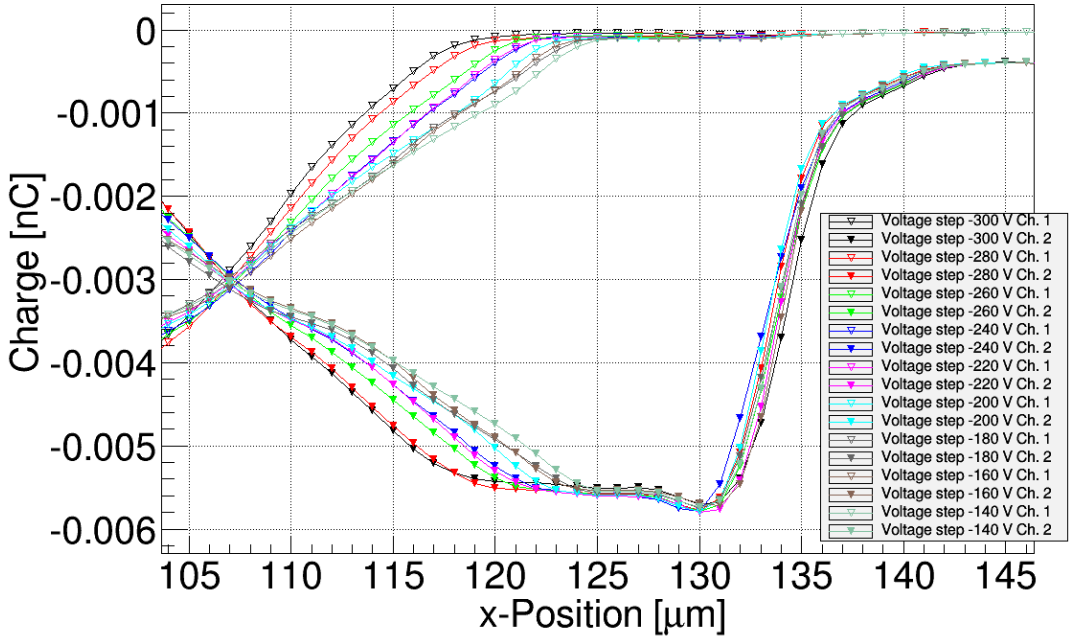

Figure 6.23: Zoom in at the peak position of the position scan for different bias voltages and high intensity red laser light.

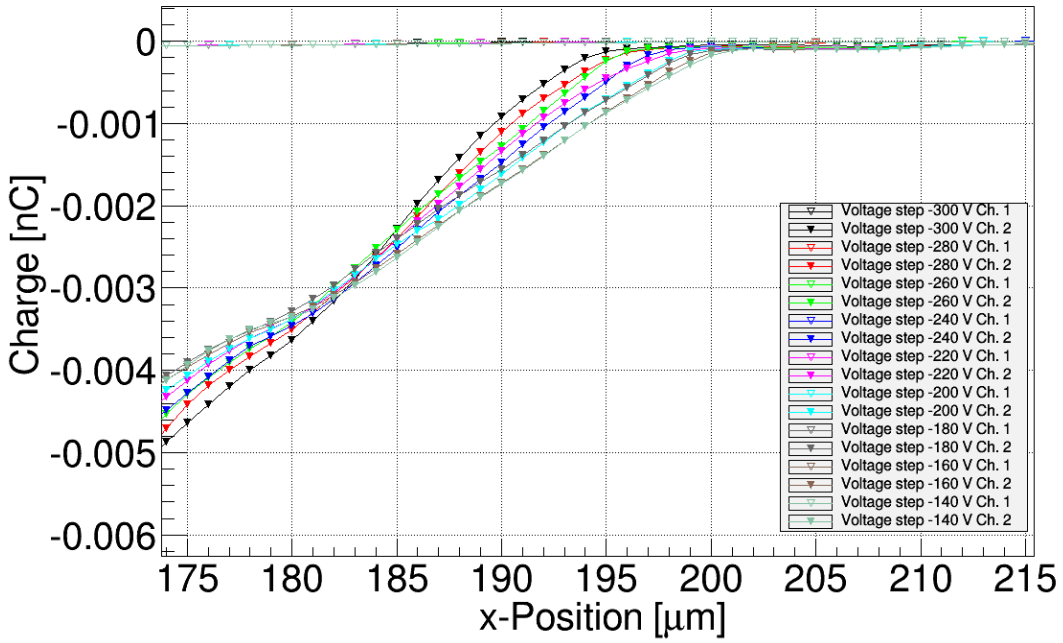

Figure 6.24: Zoom in on the slope of the position scan for different bias voltages and high intensity red laser light.

When looking at the maximum produced charge in the sensor for infrared laser light (Figure 6.26), a slight decrease with decreasing bias voltage can be observed. In contrast to the red laser light, the infrared laser light penetrates through the whole sensor. Therefore the undepleted region on the bottom of the sensor influences the amount of produced electron-hole pairs. The depletion depth depends on the applied voltage with $\sqrt{V}$. A reduction of 160 V in the bias voltage therefore only leads to a reduction of the charge in the sensor by ~ 3 pC. No significant differences for the signal spread at different bias voltages (Figure 6.27) can be observed.

For measurements with red laser light, two waveforms for a bias voltage of -140 V and -300 V are shown in Figure 6.28 and Figure 6.29 respectively. The according waveforms for the infrared laser light measurements are shown in Figure 6.30 and Figure 6.31. For both measurements, an increase of the pulse length for lower bias voltages can be observed.

Estimation of measurement uncertainties and charge carrier densities

Uncertainties on the acquired data arise due to imperfections of the readout chain. This includes:

- Fluctuation of the laser light intensity [59]: < 1 %
- Imperfection of the attenuator: $\pm$ 1 dB
- Imperfection of the amplifier: $\pm$ 1 dB

In addition to these uncertainties, an additional factor is added when determining the total charge in the sensor due to the fixed signal integration boundaries. This uncertainty was estimated by performing signal integrations with a varied integration boundary of $\pm$ 10 ns. The

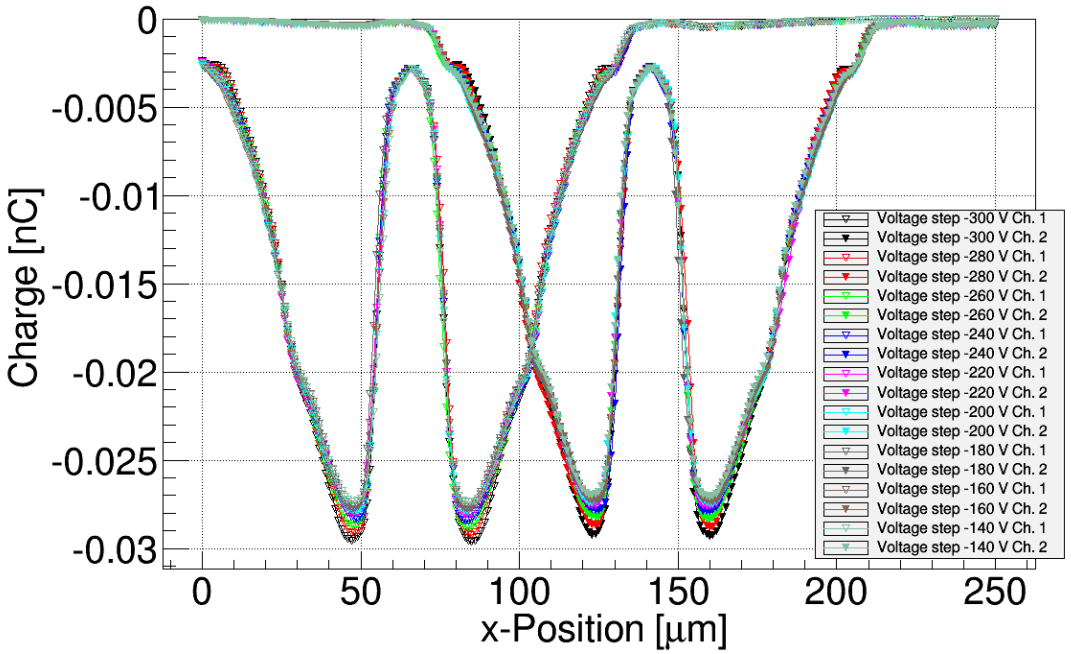

Figure 6.25: Position scans for different bias voltages and high intensity infrared laser light.

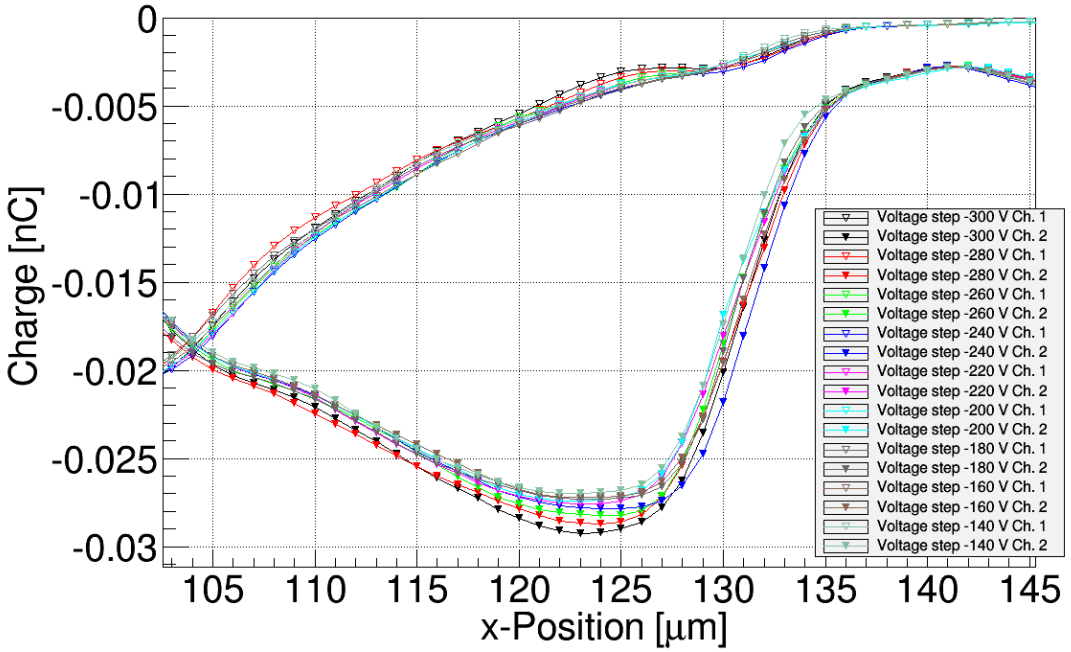

Figure 6.26: Zoom in at the peak position of the position scan for different bias voltages and high intensity infrared laser light.

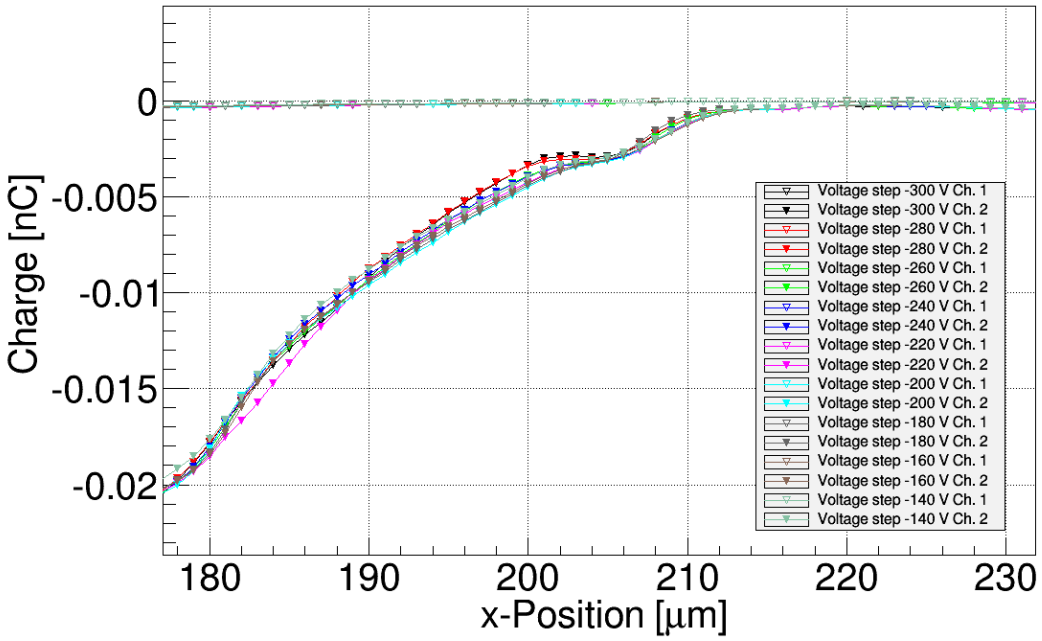

Figure 6.27: Zoom in on the slope of the position scan for different bias voltages and high intensity infrared laser light.

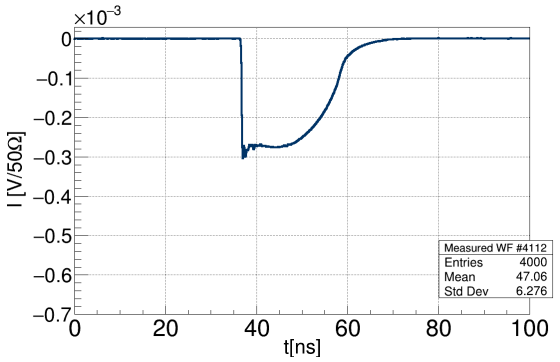

Figure 6.28: Recorded waveform for a high intensity red laser light and a bias voltage of -140 V at $x = 48$ µm.

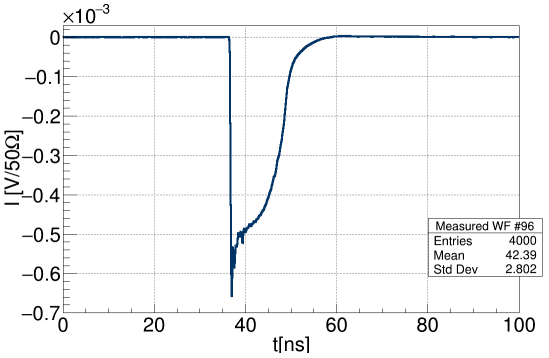

Figure 6.29: Recorded waveform for a high intensity red laser light and a bias voltage of -300 V at $x = 48$ µm.

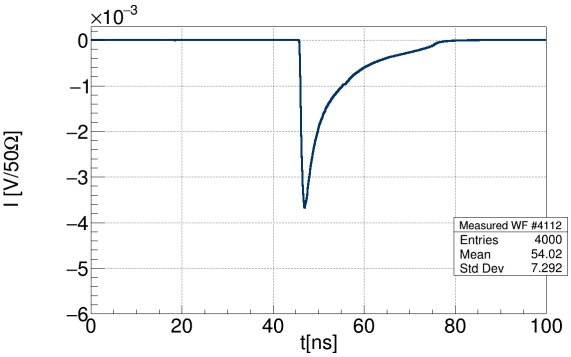

Figure 6.30: Recorded waveform for a high intensity infrared laser light and a bias voltage of -140 V at $x = 48$ µm.

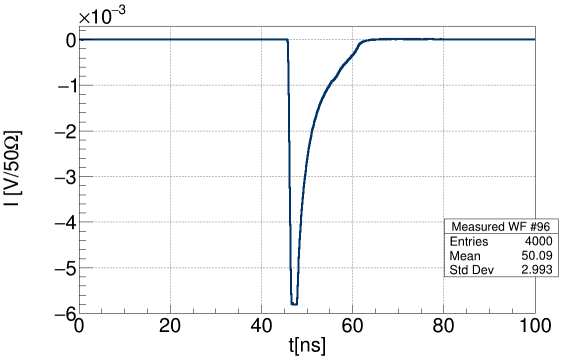

Figure 6.31: Recorded waveform for a high intensity infrared laser light and a bias voltage of -300 V at $x = 48$ µm.

uncertainty is estimated with 5 %.

To determine the electron-hole pair density in the sensor, two quantities are needed. The total number of electron-hole pairs which can be determined from the total charge in the sensor and the volume this charge was produced in. Dividing the total produced charge in the sensor by the electron charge leads to the total number of electron-hole pairs. For the maximum produced charge in the sensor of (0.029 ± 0.0015) nC with the infrared laser light, this yields $\sim (181 \pm 9) \times 10^6$ electron-hole pairs. For the red laser light a maximum charge of (0.006 ± 0.0003) nC was observed. This results in $\sim (37 \pm 2) \times 10^6$ electron-hole pairs.

To determine the sensor volume traversed by the laser light, its behaviour needs to be studied in detail. The laser beam radius at which the intensity falls to $\frac{1}{e^2}$ of its axial value at a given sensor depth s_D is given by

$$w(s_D) = w_0 \cdot \sqrt{1 + \left(\frac{s_D}{z_R}\right)^2}, \tag{6.2}$$

where w_0 is the radius at the beam waist. The radius of a Gaussian beam at the beam waist is given by

$$w_0 = 2 \cdot \sigma, \tag{6.3}$$

where σ is the standard deviation of a normal distribution. It was measured for this setup in [59] with $\sigma = (3 \pm 0.5)\mu$m.

The Rayleigh length z_R is given by [61]

$$z_R = \frac{\pi w_0^2 n}{\lambda}, \tag{6.4}$$

where λ is the free space wavelength and n the refractive index in silicon. For an incoming wavelength of 660 nm, a refractive index of $n = 3.8 \pm 0.05$ was assumed, while for 1015 nm $n = 3.5 \pm 0.1$ [62] was used. The resulting Rayleigh length is $z_R^{\text{red}} = (651.2 \pm 217.2)$ µm for the red laser light and $z_R^{\text{IR}} = (390.0 \pm 130.5)$ µm for the infrared laser light.

For the following calculations, the sensor volume traversed by the laser light is considered to have the shape of a truncated cone. To account for the divergence of the laser light inside the sensor, one of the radii was chosen to be at the maximum penetrated sensor depth $w_0(s_D^{\max})$. For the second radius, the spot size w_0 at the sensor surface was chosen, since the laser light focus was assumed to be placed there.

Due to the large uncertainties on all values, the results are rather imprecise. For an estimated maximum penetration depth of (12 ± 3) µm for the red laser light and (310 ± 25) µm for the infrared laser light this leads to:

$$V_{\text{red}} = 1\,697 \pm 525\ \mu\text{m}^3$$

$$V_{\text{IR}} = 45\,687 \pm 13\,513\ \mu\text{m}^3.$$

The resulting electron-hole pair density is $(21\,804 \pm 6\,842)$ electron-hole pairs per μm^2 for the red laser light and $(3\,962 \pm 1\,188)$ electron-hole pairs per μm^2 for the infrared laser light.

Another approach to determine a lower boundary of an upper threshold of an incoming particle intensity on the impact of the signal spread, is to translate the amount of produced electron-hole pairs to an incoming number of MIP equivalent particles. In silicon, a MIP corresponds to ~ 80 electron-hole pairs per µm thickness of penetrated detector material [13]. For the red laser light this results in

$$38\,542 \pm 9\,858 \text{ incoming MIPs.}$$

For the infrared laser light it results in

$$7\,298 \pm 691 \text{ incoming MIPs.}$$

These numbers present a lower threshold of incoming MIP-like particles on one sensor strip. The number obtained from the red laser light measurements is larger compared to the infrared measurements. Again, this is expected due to the different attenuation coefficients of these two wavelengths. To predict the real behaviour of the sensor under incoming MIPs it is more suitable to look at the infrared measurements.

Conclusion

Transient-current technique measurements with a laser at two different wavelengths were performed. The produced charge in the sensor and the spread of the signal was determined. For a number of incoming MIPs per sensor strip below $\sim 7\,300$, no problems are expected. This number is however more than 11 times smaller than possible electron intensities expected at ARES. The behaviour of the sensor under such intensities needs yet to be studied. For the here presented measurements, however, no laser with higher light intensity was available. A scan of the bias voltage showed its impact on the produced charge and the signal length in the sensor under a high intensity incoming laser beam. For red laser light, no impact on the produced charge was observed. An increase of the signal spread for lower bias voltages could however be seen. This is expected due to the influence of thermal diffusion and plasma effect which increases with a decreasing electric field strength in the sensor. For measurements with high intensity infrared laser light, a small difference in the amount of produced charge can be observed. The reduction of produced charge in the sensor when reducing the bias voltage is however small. Since an increase of the signal length occurs when reducing the bias voltage, it does not seem very beneficial to use a reduced bias voltage to reduce the charge in the sensor.

Chapter 7

STRIDENAS Functionality Tests at the DESY II Test Beam Facility

In order to test the different components of the STRIDENAS detector, measurements at the DESY II Test Beam facility were performed. The DESY II Test Beam delivers single electrons at a particle rate up to $\sim$ 40 kHz and provides infrastructure for experiments. Here, the Test Beam facility and the performed measurements are presented.

7.1 The DESY II Test Beam Facility

The DESY II Test Beam Facility [63] uses the DESY II electron synchrotron, the pre-accelerator of PETRA III. In standard operation, beams are injected at 0.45 GeV and then ramped up to 6.3 GeV with a possible maximum beam energy of 7 GeV. When no beam is requested by PETRA III, DESY II keeps the beam for two magnet cycles corresponding to 160 ms and dumps the beam afterwards. Extraction of the beam takes place within one magnet cycle (80 ms) once the electrons have reached an energy of 6 GeV. DESY II then stays empty until the next injection.

The Test Beam particles are generated by a double conversion setup. A several µm thick fibre is placed in the orbit of the DESY II beam and bremsstrahlung is produced by the electrons hitting the fibre. These photons then leave the accelerator through a 500 µm aluminium exit window and hit a secondary target. Electron-positron pairs are produced and separated by a dipole magnet placed downstream. A collimator in combination with the dipole makes a beam momentum selection possible. The selection of the electron momentum, as well as collimator settings at the entrance to the Test Beam area, can be independently controlled from the Test Beam hut by the users. A layout of the DESY II Test Beam facility is shown in Figure 7.1. For the following measurements, beamline 22 and 24 with the area 24.1 were used. Both beamline areas allow cable feed-through to the hut. In all areas a beam telescope [64] is installed, and in area 24.1 a superconducting solenoid is also available. Both infrastructures were not used. Both areas have photomultipliers installed which were used for the following measurements.

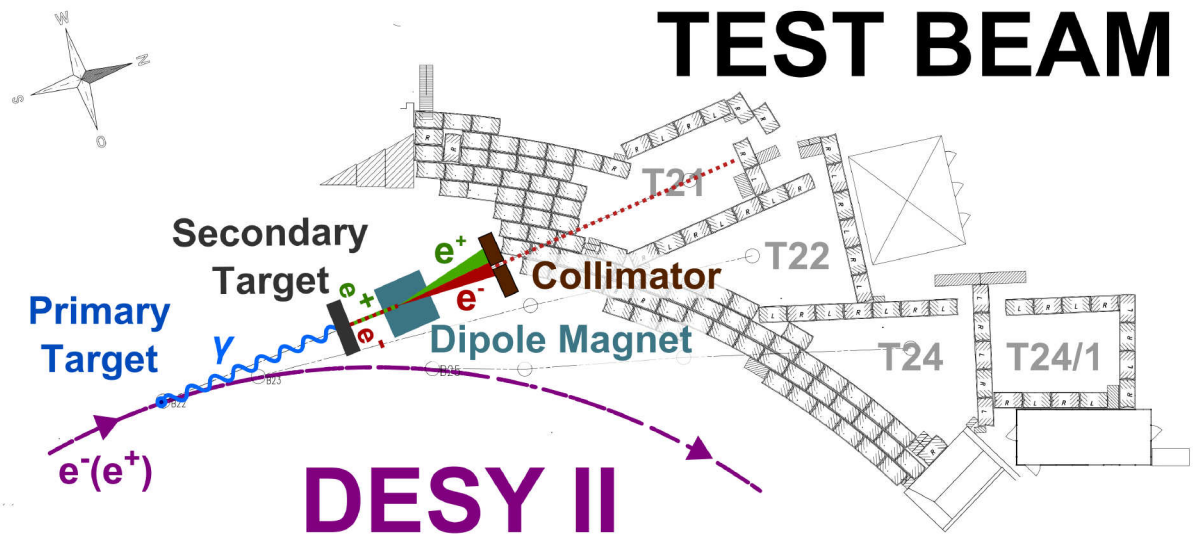

Figure 7.1: Sketch of the DESY II Test Beam facility [63]. The different beamlines are indicated.

Test Beam area 24.1 is placed behind area 24, as can be seen in Figure 7.1. It has a separate beam shutter installed, which allows access to the area even when beam in area 24 is available. This feature makes area 24.1 ideally suited for parasitic use of the DESY II Test Beam 24 when all beamlines are occupied. The collimator in area 24.1 can be exchanged manually. In both areas, linear stages were placed which can be remotely controlled from the hut. The DESY II Test Beam delivers single electrons at a rate up to 40 kHz. The particle rate depends on the selected particle energy and can be observed on a monitor in each Test Beam hut. It is, however, important to note that no reference measurement of the particle rate at the detector was available.

7.2 Proof-of-Principle Tests

Multiple measurements were performed at beamline 22. These included tests of the readout electronics, tests of the STRIDENAS detector and tests with a single sensor. The measurement setups and results are described and discussed.

7.2.1 Measurement Setup

Measurements were conducted at beamline 22 of the DESY II Test Beam. The devices under test were placed on a linear stage which could be moved in and out of the beam. The VME crate containing the CAEN readout electronic was placed on a table next to the stage and connected via an optical link to the readout computer in the Test Beam hut. In addition, a TEKTRONIX MSO 5104B oscilloscope [65] was placed next to the stage and connected to the hut via an Ethernet connection. The silicon sensors were biased via a Keithley 2410 [58] voltage source. A Keithley 3390 gate generator [66] was available. Two photomultipliers from the beam telescope

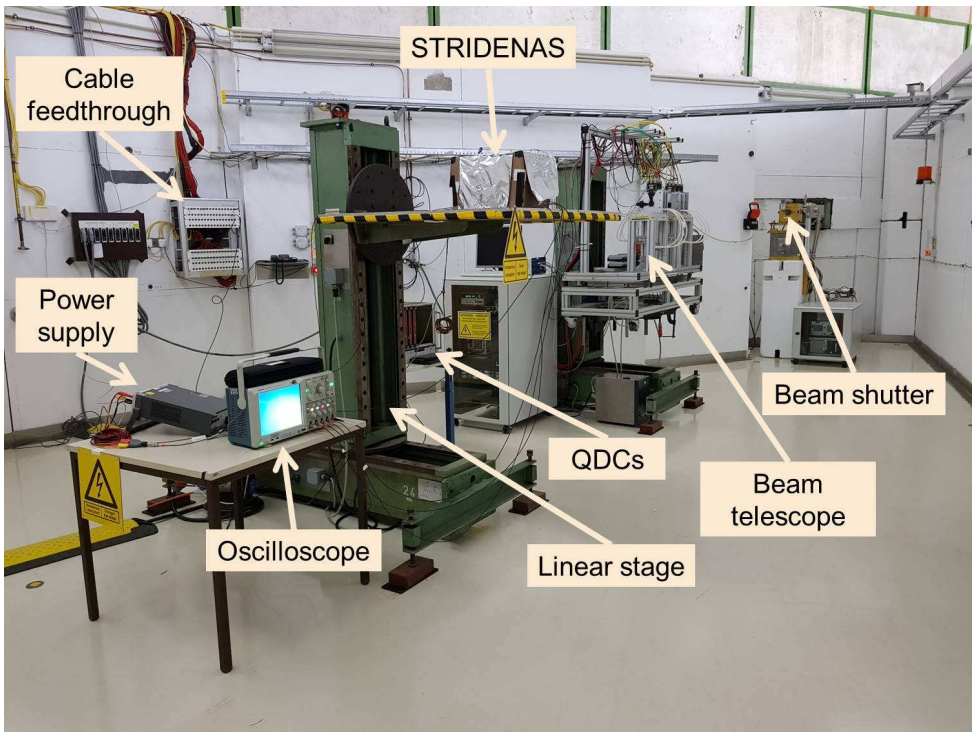

Figure 7.2: Photo of the Test Beam area 22.

were used. The operating voltage of 800 mV was supplied by the beam telescope and the signal could be read out via a LEMO-00 cable. A picture of the Test Beam area and the different components is shown in Figure 7.2.

Sensors on STRIDENAS PCB

For measurements with the STRIDENAS detector, the PCB holder was placed on the stage and the PCB was mounted. It was isolated from the stage and grounded. Sensor and LEMO ground were connected to the ground of the voltage supply. With the help of lasers indicating the beam axis, the middle of the sensors was aligned to the beam as shown in Figure 7.3. Power cables and readout were connected and the PCB holder box closed with aluminium foil and tape. In addition, a cardboard box covered in black plastic foil was placed on top. The power cables were connected to the Keithley power supply, the readout cables were connected to the oscilloscope, the QDCs or an amplifier, depending on the measurement run. For some measurements, 2 cm thick iron plates were placed in the beam in order to create a particle shower and, therefore, increase the number of particles hitting the sensor. A more detailed discussion of particle showers can be found in Appendix C.

Sensors on STRIDENAS PCB with ^{90}Sr Source

For the tests with a ^{90}Sr source on the STRIDENAS detector, the cardboard box covering was removed. The closing of the PCB holder box was changed to one aluminium foil layer with a hole facing the sensors. A ^{90}Sr source was placed in that hole. The readout channels were

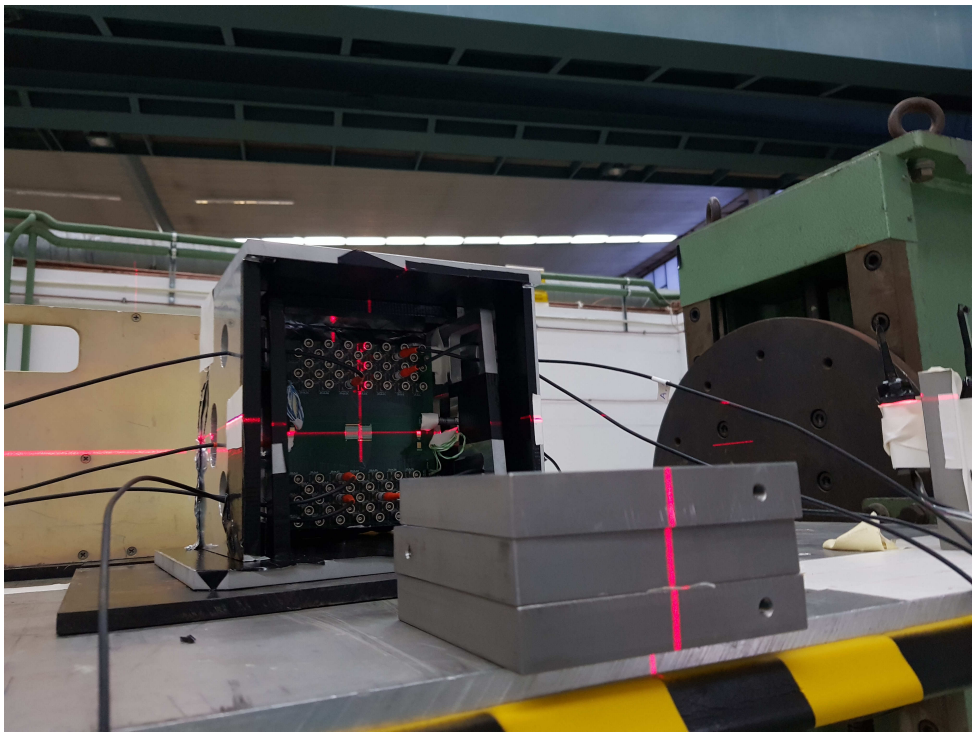

Figure 7.3: Photo showing the alignment of the sensors with the help of lasers in the Test Beam area.

connected to a QDC which was triggered by the gate generator gate pulse.

Photomultiplier Signal

Two photomultiplier tubes (PMTs) from the beam telescope were available for use. Both PMTs were connected to an active scintillator area of 1 cm x 2 cm. This area was aligned with the beam with the help of the lasers. The PMT signal was connected to the oscilloscope, the QDCs or the hut via a LEMO-00 cable.

Sensor with Single-Bonded Strips

The sensor used for the TCT measurement (described in Section 6.3) was placed in the test beam. The PCB was placed in a small plastic box with holes for the SMA connectors for power supply and readout. A picture of the sensor setup can be seen in Figure 7.4. The sensor was aligned with the help of the lasers. SMA to LEMO-00 adapters were used to connect the readout channels to the QDC. The power was delivered by the Keithley power supply.

Charge Integration Gates

The CAEN QDCs require a NIM input gate signal for data acquisition. Three different sources for gate generation were used during the measurements at the Test Beam. A brief description of each is included below.

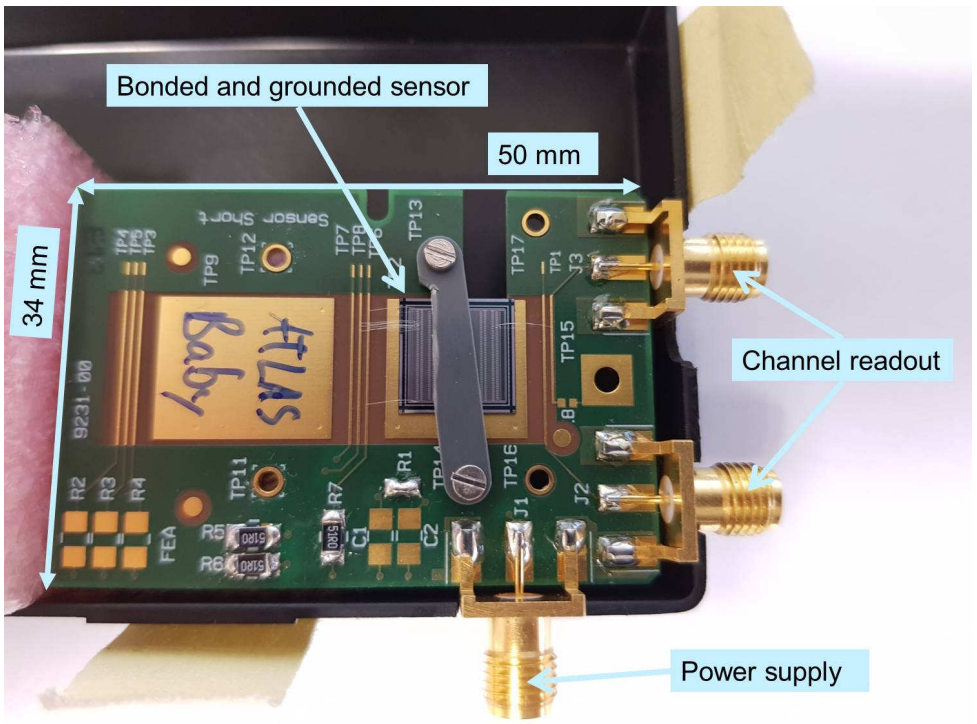

Figure 7.4: Photo of the single-bonded strip sensor and PCB in the plastic box used for placing it at the Test Beam.

E_{min} Gate The Test Beam huts are provided with a trigger signal when the beam energy at DESY II reaches its minimum. In the hut, this signal was transformed into a NIM signal to create a gate signal. To synchronize the gate signal with the time at which particles of the selected energy reach the Test Beam area, the NIM signal was delayed by $\sim$ 10 ms. A gate of 10 µs or 100 µs was created. Due to losses on the way back to the area, the signal had to be amplified and was then sent to the Test Beam area via a BNC connection and connected to the QDCs. The drawback of this gate signal is the low rate with only one gate pulse every 80 ms.

Photomultiplier Gate For this gate option, a photomultiplier signal was used as a trigger signal for the gate. The photomultiplier pulse was discriminated in the hut and a 1 µs gate was created. In order to forbid two gates to be closer than 10 µs together, a second 10 µs long signal was generated. This gap between gate pulses is needed in order to take the QDC dead time into account. Via an AND logic, the two signals were combined, triggering a gate if the 10 µs pulse is off and the 1 µs pulse is on. The resulting gate is a gate triggered by the PMT with a gap of at least 10 µs until the next gate can be triggered. The length of the signal could be changed at the NIM logic in the hut. The final gate signal was sent back to the area and fed into the QDCs. A screenshot of the PMT signal, the gap enforcing signal and the resulting gate signal can be see in Figure 7.5.

Gate Generator Gate A Keithley 3390 gate generator was used to create gate signals of different amplitude, frequency and length and a 50 Ω impedance. In contrast to the other two

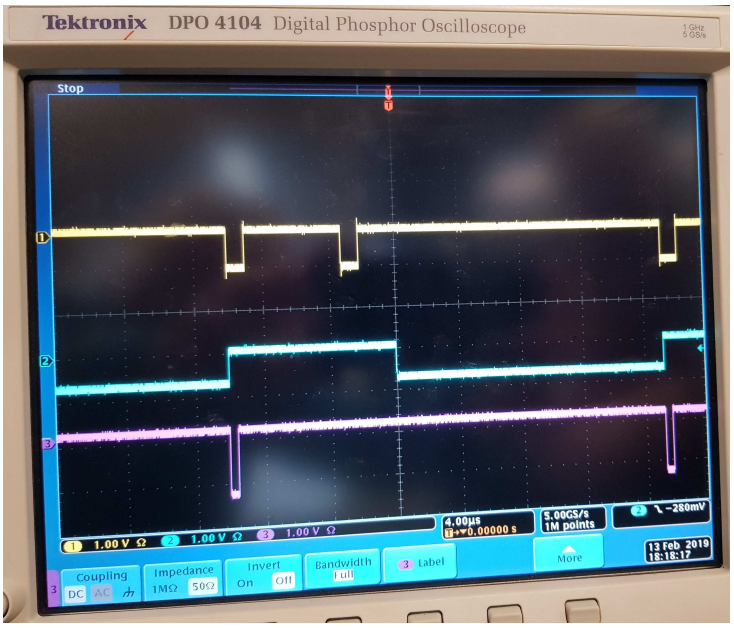

Figure 7.5: Picture of the oscilloscope showing the PMT signal (yellow / top), the gap enforcing signal (blue / middle) and the resulting gate signal (purple / bottom).

gate signals this signal is independent from the arrival of the test beam.

7.2.2 Readout Electronics Test with Photomultiplier Signals

The CAEN charge-to-digital readout electronic was tested at the DESY II Test Beam with photomultiplier signals. This approach was chosen since it was uncertain if the STRIDENAS sensor was able to produce enough charge for detection in the Test Beam. This procedure, therefore, allowed the different components of the STRIDENAS setup to be individually and independently tested. Four QDCs were available, the naming convention is explained in Table D.1. The combination of scintillator and photomultiplier (total amplification of $\sim 9.6 \cdot 10^7$) amplifies the charge sent to the QDCs. The scintillator active area of 1 cm $\times$ 2 cm enables a higher sensitivity to the incoming particles than one readout channel of the STRIDENAS detector. Therefore, the signal rate and intensity is increased.

The charge-to-digital converters were triggered with a gate from the gate generator. Measurements with different gate widths and different number of shower plates were performed. The energy of the incoming electrons was set to 1.8 GeV since the highest particle rate could be achieved at this energy. Due to the random gate signal, a high rate of empty bin counts compared to the signal rate is expected. The measured data is therefore displayed with a logarithmic scale on the y-axis.

Measurements with 15 µs Gate

Measurements on QDC 3 with different thicknesses of shower material in front of the scintillator were performed. The number of produced shower particles depends on the thickness of the material. Without an iron plate placed in the beam, the signal is expected to be generated

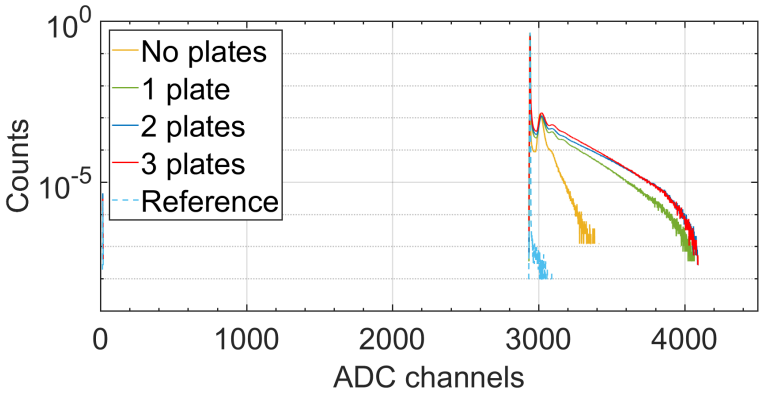

Figure 7.6: QDC measurement with 15 µs gate width. Measurements for 0, 1, 2 and 3 shower plates in the beam before the scintillator were performed. The high-charge range of the QDC is displayed. The number of counts has been normalized to the total number of recorded events.

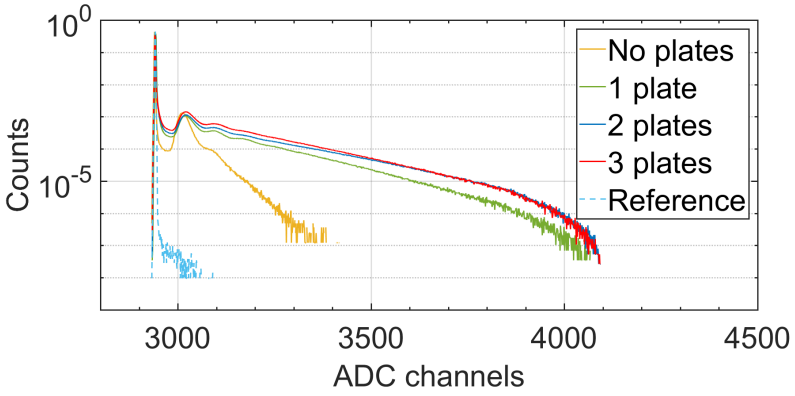

Figure 7.7: Zoom in on the QDC measurement with 15 µs gate width. Measurements for 0, 1, 2 and 3 shower plates in the beam before the scintillator were performed. The high-charge range of the QDC is displayed. The number of counts has been normalized to the total number of recorded events.

by one electron only. Once one iron plate with a thickness of 2 cm is placed in the beam, signals created by one electron as well as signals created by two or more particles are expected. When increasing the material thickness to 4 cm and 6 cm, more particles are expected to hit the scintillator and produce a higher charge. The aim of this measurement was to see if the difference between one incoming electron and more incoming particles can be resolved with the STRIDENAS readout electronics as well as if it is possible to see differences in the signals for the different thicknesses of the shower material. The measurements were performed with a 15 µs long gate signal. Due to the length of the gate signal, only the high-charge range of the QDC acquired data. The integrated charge exceeded the dynamic range of the low-charge range. The amplitude of the gate signal was not monitored, but lay between -1 V and -1.5 V. A reference measurement was performed with no iron plate and the Test Beam switched off.

The recorded signals are normalized to the total number of recorded events for each measurement. Results are shown in Figure 7.6, and a zoom is shown in Figure 7.7. The ADC channels correspond to the integrated charge value of the QDC per applied gate signal. A noise

peak at around 2900 ADC counts is visible for all four measurements and agrees well with the recorded noise from the reference measurement. The counts below 100 ADC channels also appear in the reference measurement and most likely occur due to the choice of gate width and gate amplitude.

The ADC counts for the first peak next to the noise peak agree well for the measurements with one to three shower plates. The measurement without a shower plate is shifted to lower ADC Channels by about 10. The standard deviation of the reference measurement is 6.5 ADC counts. When looking at the one plate measurement, the first visible peak has a distance of around 72 ADC counts to the noise peak. This results in a signal-to-noise distance of ~ 11. For the measurement with no shower plates, no further peaks are visible. This is expected since only one electron per 15 µs gate is expected from the Test Beam. When looking at the measurement with 1 shower plate, two additional peaks at higher ADC counts are visible. These peaks are expected due to shower particles hitting the scintillator and producing additional charge. When two or three shower plates are placed in the beam, these additional peaks smear out. This can be explained by the higher number of shower particles being produced. These shower particles are not only minimum ionizing particles, as they can have different energies, and their number varies. Therefore, the produced charge in the scintillator is no longer discrete and the peaks are smeared out.

Measurements with 1 µs Gate

As discussed above, the best visibility of detected peaks caused by shower particles is given for one shower plate. The following measurements therefore show comparisons between zero and one shower plate. The aim of these measurements was to investigate the difference between zero and one shower plate in more detail as well as to compare results from the low-charge and high-charge ranges. For this, the smaller gate width was needed in order not to reach saturation of the low-charge range. The gate width was set to 1 µs with a gate amplitude of -800 mV. Measurements were performed using QDC 1 and QDC 2. The reference measurements were performed with the Test Beam switched off. The measurements on QDC 1 for the low-charge range are shown in Figure 7.8. The measurements for the high-charge range are shown in Figure 7.9. The measurements are normalized to the total number of recorded events for each measurement run. For the low-charge range measurement, the peaks are shifted to higher ADC channel values compared to the high-charge range. This is expected since one ADC count in the low-charge range corresponds to less charge than in the high-charge range. This also leads to the broadened peaks in the low-charge range compared to the high-charge range.

The recorded data with one shower plate was fitted in the high-range measurement with a superposition of three Landau functions (see Section 2.2.2). This fit function was chosen to represent the three visible peaks, which are expected to correspond to 1, 2 and 3 particle events, assuming the deposited energy follows a Landau distribution. The fitting range was set between ADC channel 288 and 520 to suppress the influence of the high intensity noise peak

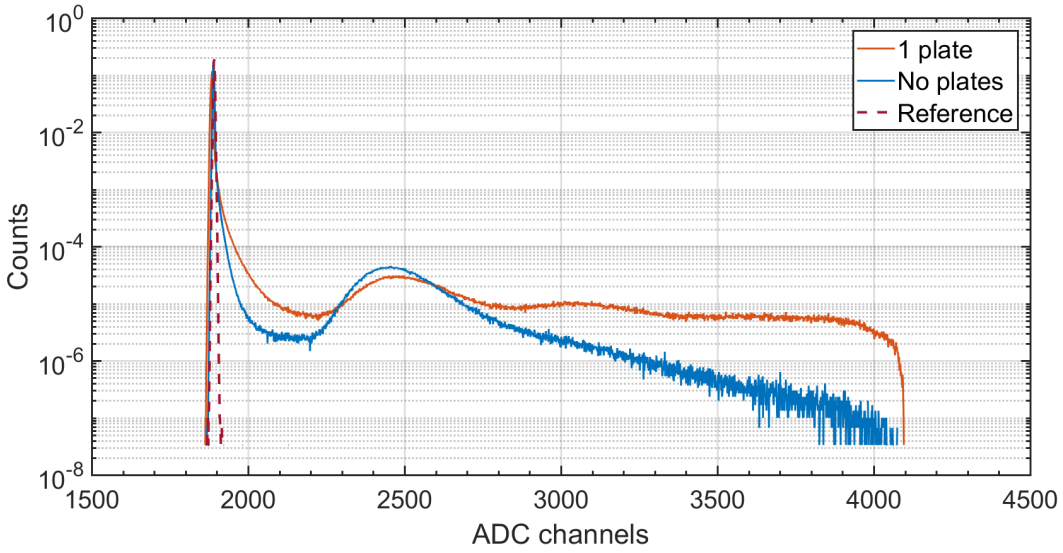

Figure 7.8: Measurement of the low-charge range of QDC 1 with a 1 µs gate width and zero and one shower plates. The number of counts has been normalized to the total number of recorded events.

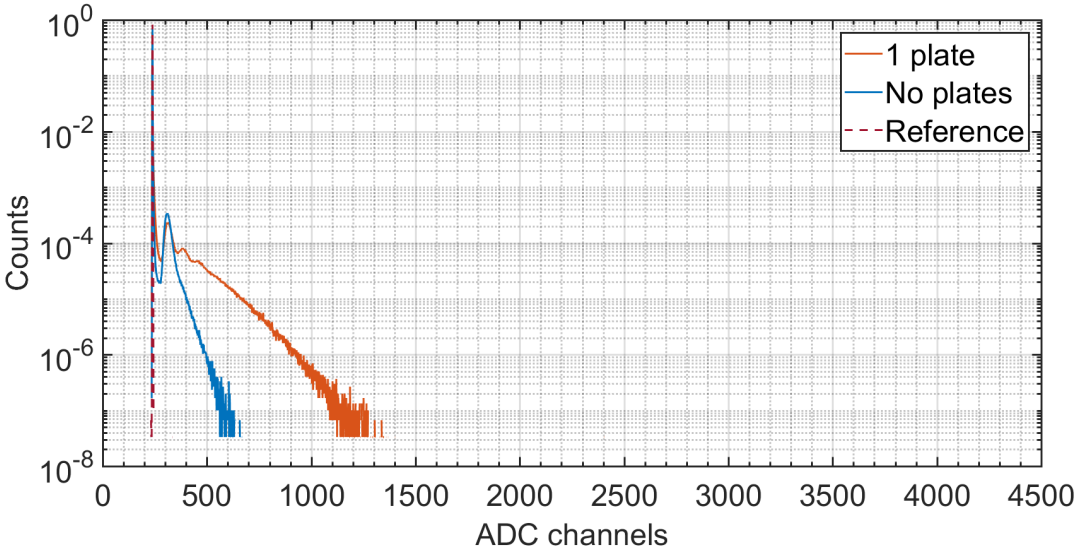

Figure 7.9: Measurement of the high-charge range of QDC 1 with a 1 µs gate width and zero and one shower plates. The number of counts has been normalized to the total number of recorded events.

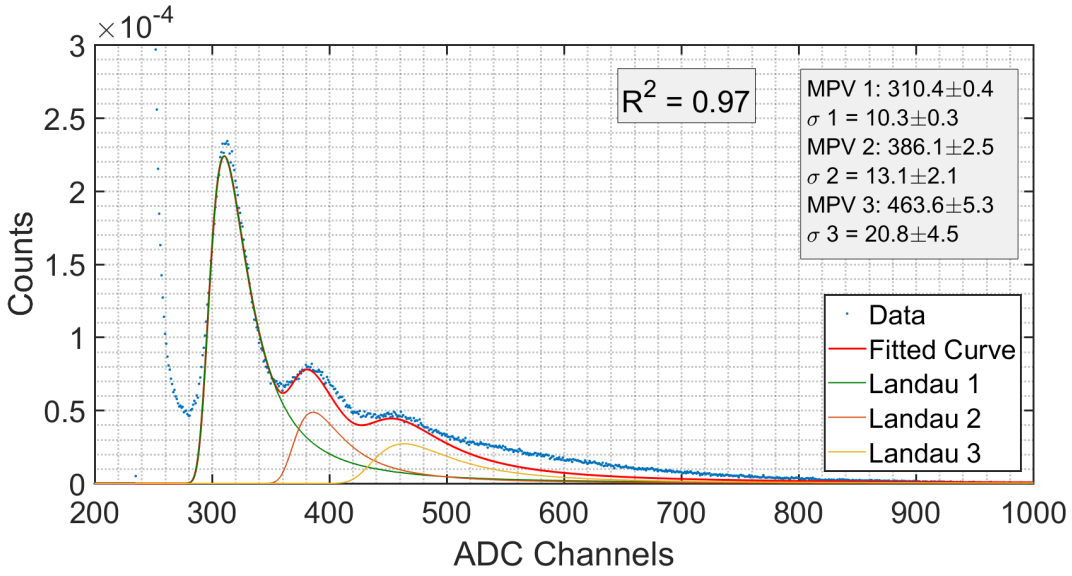

Figure 7.10: Triple Landau distribution fit to the photomultiplier data measured with the QDC high range and one shower plate. The data is displayed in a linear range and normalized to the total number of recorded events.

Table 7.1: Fit parameters for the triple Landau distribution fit to the measured photomultiplier signal with one shower plate shown in Figure 7.10.

	Landau 1	**Landau 2**	**Landau 3**
Mean [ADC Channel]	310.4 ± 0.4	386.1 ± 2.5	463.6 ± 5.3
Sigma [ADC Channel]	10.3 ± 0.3	13.1 ± 2.1	20.8 ± 4.5

and acquired data beyond the third visible peak. The result is shown in Figure 7.10 using a linear scale to illustrate the shape of the Landau functions. The resulting fit parameters are also listed in Table 7.1. When looking at the peak-to-peak distances, the fit shows an equally spaced peak structure within the fit uncertainties. The distance between the first and second peak is (75.7 ± 2.5) ADC Channels, the distance between the second and third peak is (77.5 ± 5.9) ADC Channels. Assuming 200 fC per ADC Channel this results in a spacing of (15.1 ± 0.5) pC and (15.5 ± 1.2) pC, respectively.

Assuming a photomultiplier gain of 2×10^5 [67], a scintillator light yield of ~ 1600 photons per mm and per incoming MIP and an efficiency of 10 % [68], the produced charge per incoming MIP after the photomultiplier can be roughly estimated to be 15 pC. This agrees well with the peak spacing measured with the QDC.

Comparison of the different QDCs using a 1 µs Gate

Measurements with all four QDCs, one shower plate and a gate width of 1 µs were performed. The amplitude of the gate signal is -800 mV for QDC 1 and QDC 2. For QDC 3 and QDC 4 the amplitude was not monitored and lay between -1 V and -1.5 V. The aim of these measurements was to perform a functionality test of all four QDCs and to compare their results.

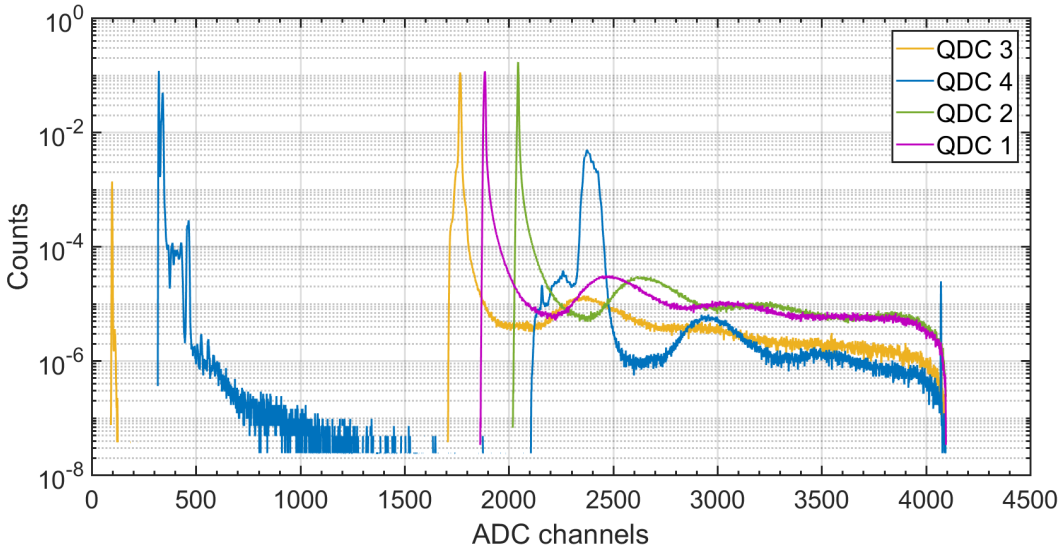

Figure 7.11: Comparison of different QDCs with a gate width of 1 µs and one shower plate. The low range channel of the QDC is displayed. The number of counts has been normalized to the total number of recorded events.

With the help of these measurements, it was concluded that the gate signal amplitude has an impact on the recorded signal quality and the amount of recorded noise. In Figure 7.11, the signals for all four QDC in the low-charge range are displayed. The measurements are normalized to the total number of recorded events. For QDC 3 and QDC 4, counts at low ADC channels are visible. These counts most likely occur due to the amplitude settings of the gate signal. When changing the amplitude of the gate signal for later measurements, these low ADC channel counts disappeared (see also Appendix D). Despite these counts at low ADC channels, several peaks are visible.

7.2.3 Test Measurements of the STRIDENAS Detector

Various measurements using the STRIDENAS detector were performed. For these measurements, the two sensors were biased with -95 V. First measurements were performed using an oscilloscope for the readout. This setup was used to reduce the electronic noise as much as possible by grounding the sensors and connectors on the PCB as well as isolating the setup from the linear stage. Once this was done, different sensor channels were connected to the oscilloscope. One channel was directly connected, and two channels first went through an amplifier. In addition, a signal from a photomultiplier was fed into the oscilloscope to be used as a trigger. Two iron plates to create particle showers were placed in front of the STRIDENAS sensors. The photomultiplier was mounted before the plates. No beam signals from the STRIDENAS detector were observed. The amplifier, however, introduced additional noise on the channel and was found unsuitable for this setup.

A measurement of STRIDENAS using the QDC 4 for readout was also performed using a gate signal of 1 µs. As an example, the data acquired in the low-charge range of channel B10

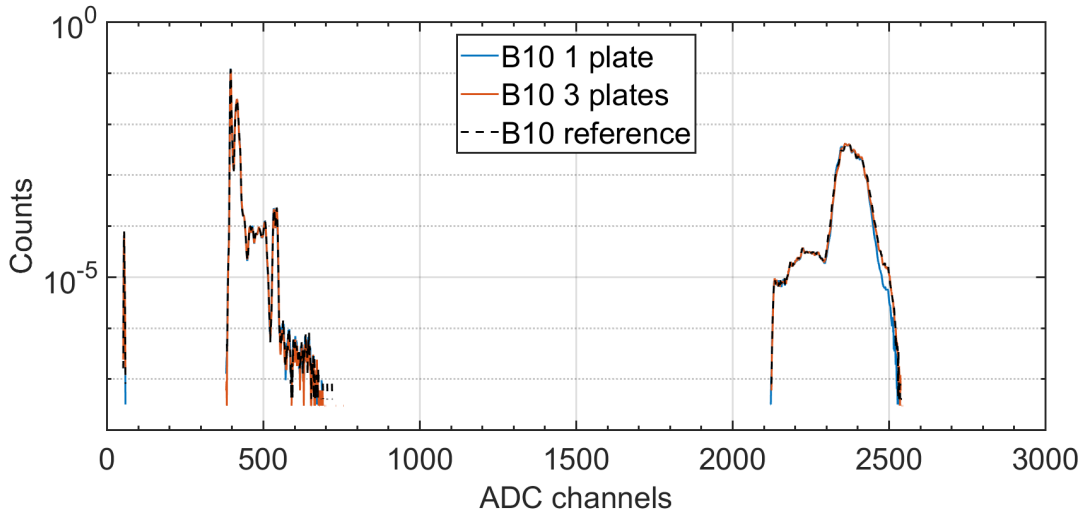

Figure 7.12: STRIDENAS measurements with 1 µs gate width. Measurements with one and three shower plates as well as a reference measurement without beam are displayed for the QDC 4 in low-charge range. The number of counts has been normalized to the total number of recorded events.

(see Figure 5.3 and 5.5 for reference) is shown in Figure 7.12. The reference measurement was performed with no beam and with applied bias voltage. Measurements with one and three iron shower plates in the beam were performed. The data is normalized to the total number of recorded events. No differences between the reference measurement and the measurements with beam can be seen. Therefore no particles from the Test Beam could be observed during this measurement. The shape of the noise (visible counts in Figure 7.12) is caused by the amplitude of the gate signal as it can also be seen in Figure 7.11. The amplitude of the gate signal was not monitored and lay between -1 V and -1.5 V. The knowledge of the gate signal amplitude being a crucial value for the data acquisition was only gained later in the measurement campaign after many discussions with the CAEN support team.

Further measurements of the STRIDENAS detector in combination with the QDC readout electronics were conducted using E_{min} gate signals as well as 15 µs width gate signals from the gate generator. Still, no signals from the beam could be observed. As a final test with the STRIDENAS detector, in order to have more control of the electron rate and position on the sensor, tests using a ^{90}Sr source were performed. The readout was done by a QDC. A 15 µs gate width was used. A reference measurement with no radioactive source was performed. No differences between this reference measurement and those including the sample could be observed.

In conclusion it was found that measurements with the STRIDENAS detector were unsuccessful due to the problems of an early breakdown described in Section 6.2. To investigate whether it is in principle possible to observe electrons with this setup, measurements with another ATLAS12EC miniature sensor were performed.

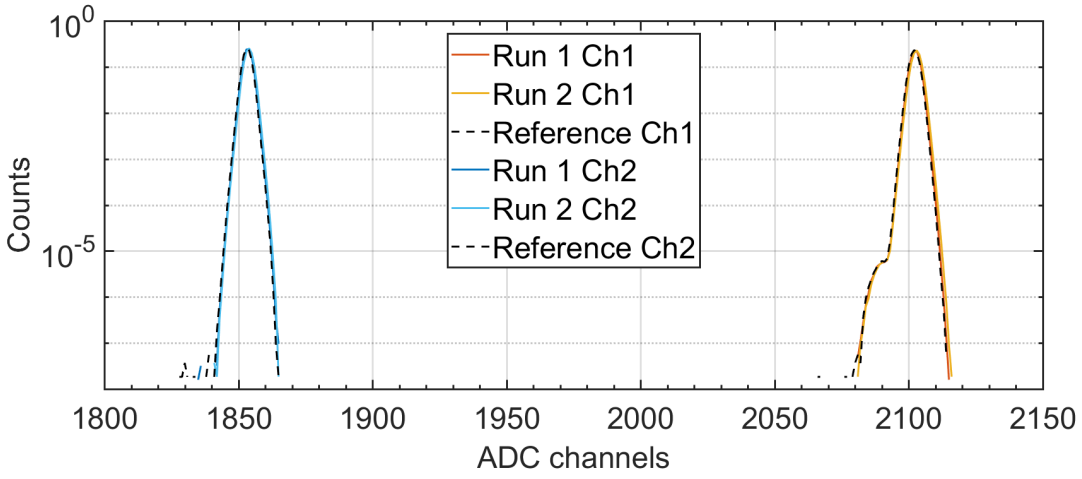

Figure 7.13: Single-bonded strip sensor measurements with a gate generator gate of 1 µs and 3 plates placed in the beam. Both channels of the sensor were read out with the QDC 4. The reference measurement was performed with an applied bias voltage and the beam switched off. The number of counts has been normalized to the total number of recorded events.

7.2.4 Test of Sensor with Single-Bonded Strips

The here investigated sensor was bonded for TCT measurements which are described in Section 6.3. Only two single sensor strips with a width of 74.5 µm each were connected and read out by the QDCs. A bias voltage of −290 V was applied on this sensor. Three iron plates were placed in the beam to increase the particle rate as much as possible. Measurements with a gate generator gate of 1 µs width and −800 mV amplitude were performed. Both sensor channels were read out with the QDC 4. Reference measurements were performed while the Test Beam was switched off and the bias voltage of the sensor still applied. The recorded signals for the low-charge range are shown in Figure 7.13 and are normalized to the total number of recorded events for each measurement run. The measurements with beam for both channels shown no difference to the reference measurement. No signal from the beam is visible.

The two noise peaks from channel 1 and channel 2 are separated by around 250 ADC channels. This difference might occur due to different leakage currents on the two strips or due to different noise means in the two QDC channels.

In addition, measurements with a photomultiplier gate signal were performed. The signal width was varied. The measured amplitude of the gate signal in the Test Beam hut was −1.3 V. Due to long cables to the Test Beam area, losses are expected. The amplitude is expected to be between −800 mV and −1 V. Reference measurements for photomultiplier gates were performed by moving the sensor out of the beam axis and tilting it by 90° to minimize the active sensor area exposed to the Test Beam. The aim of these measurements was to optimize coincidence between gate signal and incoming electron and therefore increase the chances of a detected signal. Since the gate signal needs to pass through several meters of cable, the coincidence between incoming electron and gate signal is however questionable. Measurements

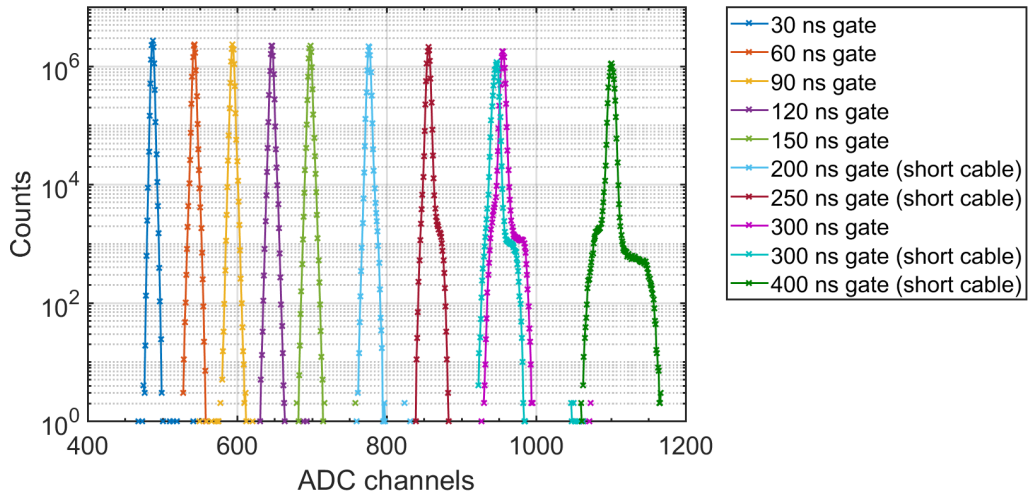

Figure 7.14: Single-bonded strip sensor measurements with a PMT gate of 1 µs and 3 plates placed in the beam. The reference measurement was performed by moving the sensor out of the Test Beam.

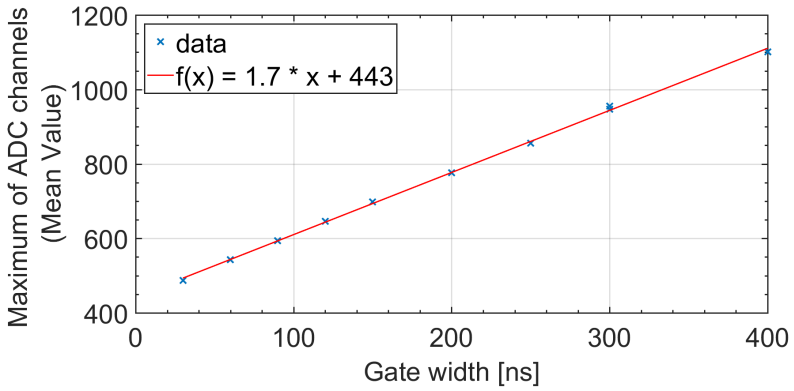

Figure 7.15: ADC count for the maximum signal value for different gate widths.

with a reduced cable length were therefore also performed.

In addition, these measurements were used to study the behaviour of the QDC under different gate widths. The measurements for different gate widths and cable lengths are shown in Figure 7.14. No particle signals can be seen. The ADC channel for the maximum signal value for each gate width measurement was obtained. The relation between these values and a linear fit is shown in Figure 7.15. The ADC count for the maximum value shifts proportional to the applied gate width. The standard deviation of the measured distribution for each gate width was determined and is shown in Figure 7.16. The standard deviation was expected to be independent of the applied gate width. This, however, seems only to be the case for gate widths below 300 ns. The increase of the standard deviation worsens the signal-to-noise ratio.

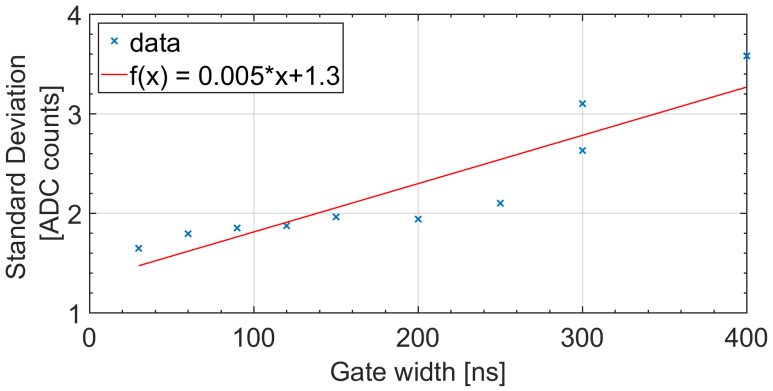

Figure 7.16: Standard deviation for different gate widths.

7.2.5 Summary of the Performed Measurements

The functionality of the readout electronics was tested with photomultiplier signals triggered by electrons from the DESY II Test Beam facility. The low-charge range and high-charge range were tested and are working. The increase of measured charge with the increase of incoming particles as expected was confirmed and agrees well with the expected produced charge of the PMT. The pulses created by the photomultiplier were resolved well.

Due to the low electron rate at the Test Beam, the signal produced inside the sensor was too small to be detected by the QDCs or oscilloscope. The produced charge in the sensor for one incoming electron is expected to be ~ 4 fC, which lies well below the resolution of 25 fC for the low-charge QDC range. Therefore, it is not unexpected that no signal from the beam was observed with the QDCs. Attempts to increase the particle intensity per readout gate with a longer gate width or particle showers were unsuccessful. In order to compensate for losses in the cables and to resolve signals with the readout electronics, a higher charge carrier density in the sensor is needed. Alternatively, the signal could be increased by placing an amplifier close to the sensor.

7.3 Sensor Test with an Amplifier

During the first measurement campaign at the DESY II Test Beam, it was seen that the produced charge was insufficient to be detected with the STRIDENAS setup. Therefore, a new fast (GHz) amplifier was purchased and implemented in the measurement setup.

7.3.1 Measurement Setup

Measurements using this amplifier were taken at the Test Beam area 24.1, which is using the beamline 24. For the measurements with the fast amplifier, the sensor with single-bonded strips was placed in the beam. The sensor was aligned to the incoming electron beam using the alignment lasers in the Test Beam area. In addition, the beam was not collimated to increase the particle rate and probability to hit the bonded strip on the sensor. A 2 cm thick iron plate was placed in front of the sensor in the beam to create a particle shower and increase the particle rate on the strip. One single-bonded strip of the sensor was connected to a Femto HSA-X-1-40 amplifier [69]. The amplifier specifications are listed in Table 7.2.

Table 7.2: Femto HSA-X-1-40 amplifier specifications [69].

Parameter	**Unit**	**Value**
Gain	dB	40 ± 1
Impedance	Ω	50
Bandwidth	kHz	10 - 1200000
Rise time	ps	290

The amplified signal was fed into a Tektronix MSO 5104B oscilloscope [65]. In addition, four photomultipliers were placed in the beam before the measurement setup and a coincidence photomultiplier signal was fed into a second channel of the oscilloscope for comparison with the sensor signals. A bias voltage of -290 V was applied to the sensor. This corresponds to the measured depletion voltage of the sensor (Section 6.1). A picture of the setup is shown in Figure 7.17. The oscilloscope was remotely controlled from the Test Beam hut.

7.3.2 Measurements

Measurements were performed parasitically to other Test Beam users with an electron energy of 2 GeV and 4 GeV. A total number of 328 signals were recorded. An example of a recorded waveform is shown in Figure 7.18. The blue signal corresponds to the sensor strip signal while the orange signal corresponds to the photomultiplier signal. A clear sensor signal at a time of 0 ns is visible as well as a photomultiplier signal delayed by ~ 40 ns. This delay is expected since this signal runs through different NIM modules before reaching the oscilloscope. The photomultiplier pulse is a coincidence pulse between four photomultipliers. It is not expected to always trigger when a sensor signal is seen, since the coincidence of all four photomultipliers is

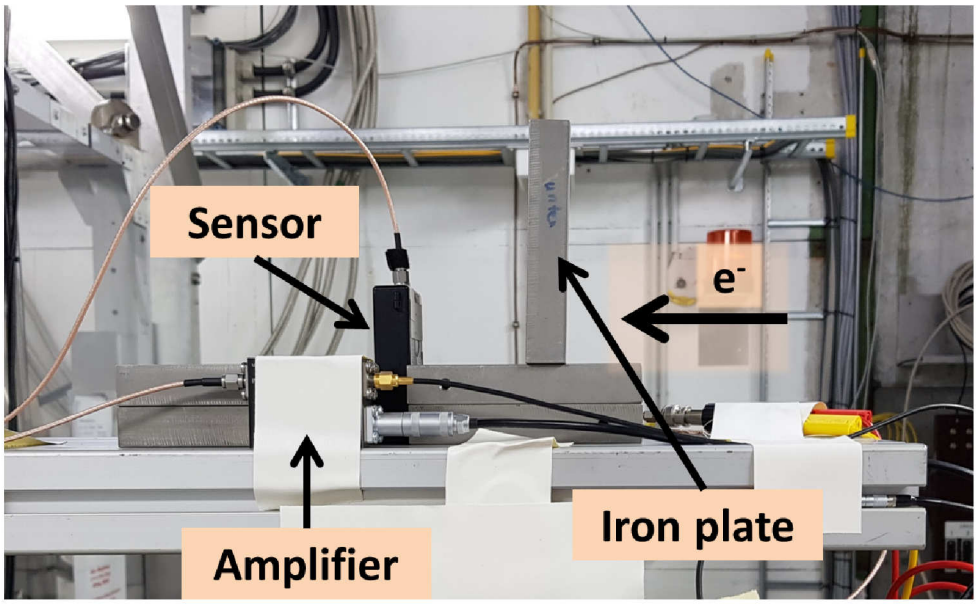

Figure 7.17: Side view of the measurement setup with the single-bonded strip sensor at the DESY II Test Beam facility.

not always given. The area of the sensor signal is proportional to the produced charge inside the sensor and varies according to the Landau distribution. To obtain the area under the signal, the signals were integrated over 15 ns. The integration boundaries were determined automatically relatively to the peak position starting 50 data points before and ending 240 data points after the peak exceeds -0.02 V. This integration range was chosen to ensure that the signal of each recorded waveform always fits into this integration range. Figure 7.19 shows the superposition of all recorded waveforms. In Figure 7.20 and Figure 7.21, two waveforms of different widths are shown as an example.

The baselines of the recorded waveforms have an offset from the zero position. This offset was corrected for by taking the mean of all recorded values 100 steps before the lower integration boundary. This value was then subtracted from all measurement points. The baseline correction was performed for all waveforms individually. A histogram of the integrated signals for the whole dataset is shown in Figure 7.22. A fit for the Landau distribution for the different integrals is shown in Figure 7.23. The different integral values agree well with the Landau distribution as can be seen by the factor R^2 of 0.97. The most probable value (MPV) obtained from the fit can be used as an integral equivalent to the average charge produced in the sensor.

When looking at the waveforms, every wiggle of the noise could be mistaken for a signal. Therefore, to determine the noise of the measurements, the data between neighbouring zero crossings was integrated. These values are assumed to be Gaussian and were fitted for each recorded measurement separately. The value of the standard deviation for each measurement is shown in Figure 7.24. The mean of the Gaussian lies around zero as expected and is shown in Figure 7.25. When the noise is assumed to be equal for all measurements, the noise integrals of all measurements can be combined. All values were fed into a histogram and fitted by a Gaussian. The obtained fit values give a mean of $\mu \sim (-2 \pm 22) \cdot 10^{-5}$ V and a standard

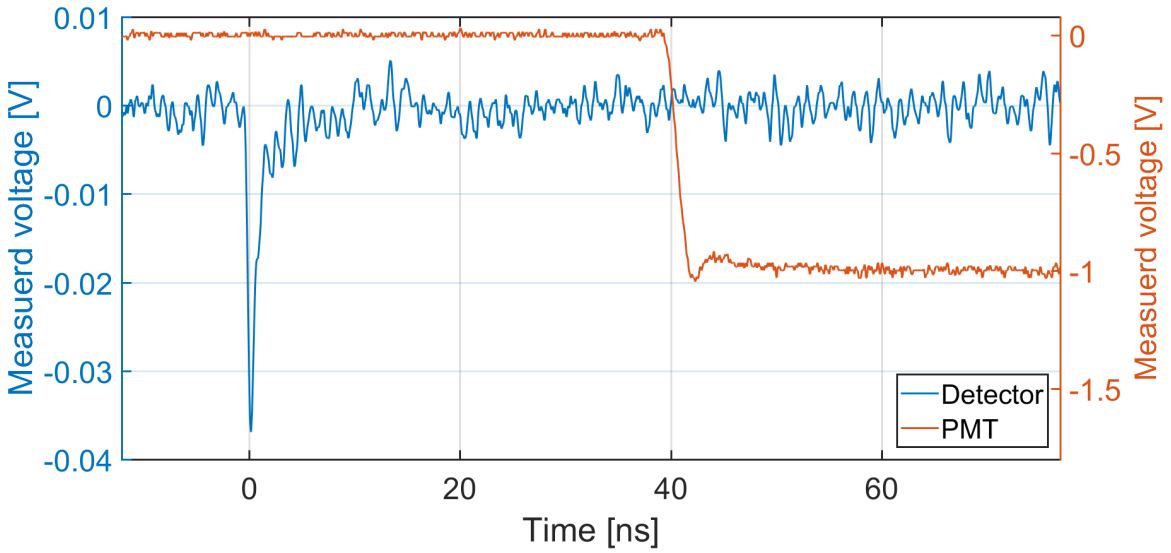

Figure 7.18: Example of a measured waveform for the sensor signal (blue) and photomultiplier signal (orange).

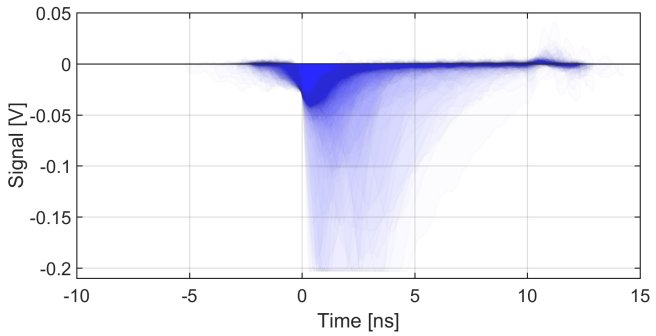

Figure 7.19: Superposition of all measured waveforms.

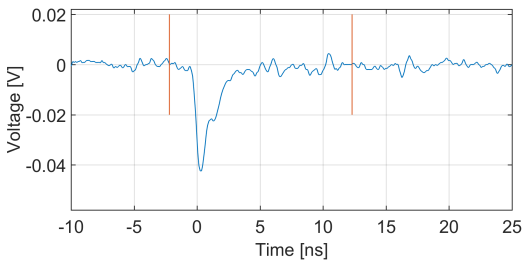

Figure 7.20: Thin waveform with integration boundaries.

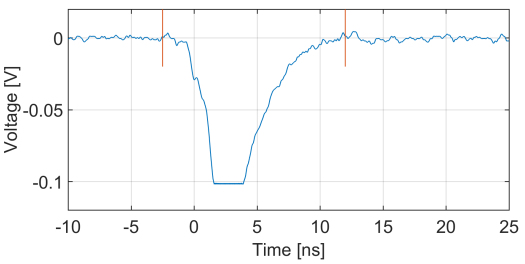

Figure 7.21: Wide waveform (truncated) with integration boundaries.

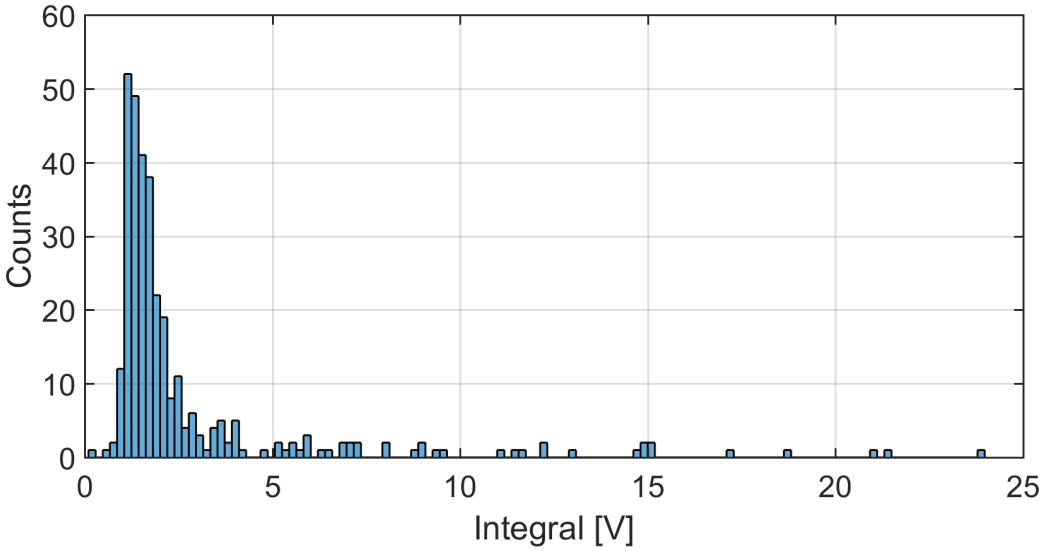

Figure 7.22: Histogram of waveform integrals. The integral values correspond to the integral I_M described in Equation 7.1.

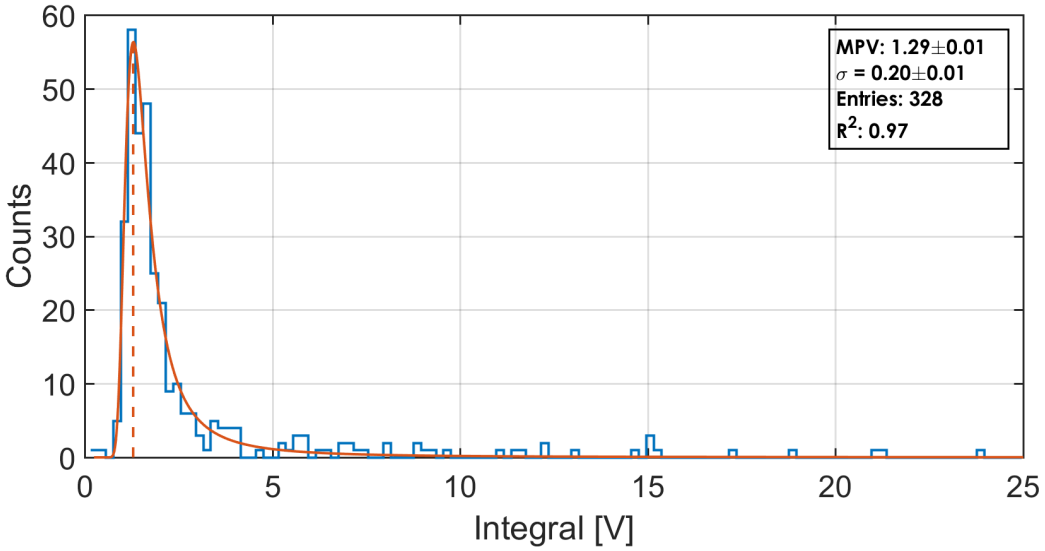

Figure 7.23: Histogram of waveform integrals and fit of a Landau distribution. The integral values correspond to the integral I_M described in Equation 7.1.

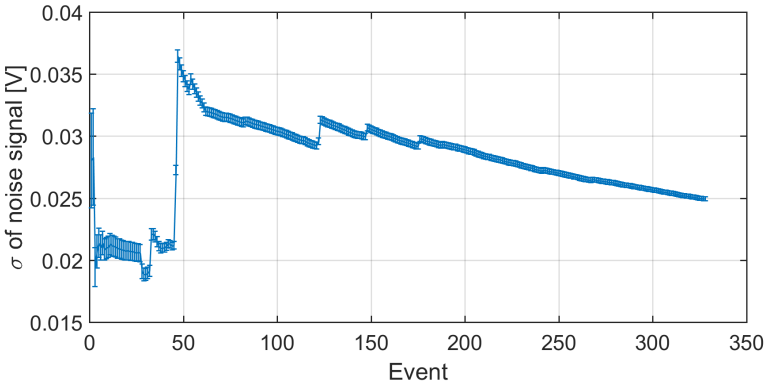

Figure 7.24: Sigma of noise values.

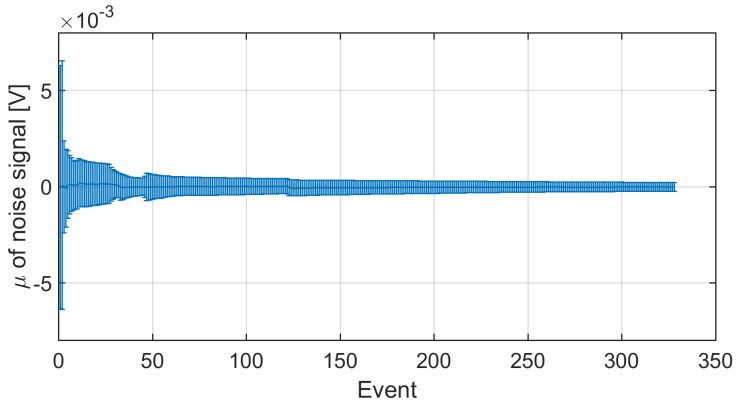

Figure 7.25: Mean of noise values.

deviation of $\sigma \sim 0.0249 \pm 0.0002$ V. This results in a signal-to-noise ratio of about 51.

The produced charge in the sensor can be calculated from the data as

$$Q = \frac{L_c}{A \cdot R} \cdot \int_{t_s}^{t_f} U dt \sim \frac{L_c}{A \cdot R} \cdot I_M \cdot \Delta t, \tag{7.1}$$

where L_c is the compensation for signal losses in the cable, A is the amplification factor of the amplifier, R is the impedance of the system and U is the measured voltage, which is integrated between the starting and final time boundaries t_s and t_f. This integral was calculated with a MATLAB function which assumes a unitary spacing between data point. Therefore, the obtained integral value, I_M, has to be multiplied by the actual data spacing Δt. Impedance mismatch and changes in the times steps (sampling rate of oscilloscope) were neglected. The uncertainty on the amplification factor includes an uncertainty due to a temperature dependence of the device and a baseline shift and is listed with 1 dB in the datasheet [69]. The uncertainty on the signal integral is composed of the uncertainties introduced by the integration boundaries, the fit uncertainty of the most probable value (if used) and the noise, where the integration boundary uncertainty is three times bigger than the other contributions.

The average charge produced inside the sensor was determined by using Equation 7.1. For the integral value, the most probable value obtained from the Landau fit was used. All parame-

Table 7.3: Parameters for signal calculations.

Parameter	Unit	Value
Most probable value (MPV)	V	1.29
Amplification (A)	dB	40 [69]
System impedance (R)	Ω	50
Sampling step (Δt)	s	$5.17 \cdot 10^{-11}$
Loss compensation (L_c)		1.07 [51]
Sensor thickness (d_{sensor})	µm	310

Table 7.4: Uncertainties for signal calculations.

Parameter	Unit	Value
σ_{I_M}	V	0.124
$\sigma_{\text{MPV}}^{\text{Fit}}$	V	0.014
σ_{Noise}	V	0.028
$\sigma_{\text{MPV}}^{\text{tot}}$	V	0.128
σ_{A}	dB	1 [69]
$\sigma_{\text{d}_{\text{sensor}}}$	µm	25

ters and uncertainties are listed in Table 7.3 and Table 7.4, respectively. With these values, the average charge produced in the sensor was found to be

$$Q = (1.43 \pm 0.14) \cdot 10^{-14}\,\text{C}.$$

The number of produced electron-hole pairs per µm sensor thickness can be obtained by dividing Q over the thickness of the sensor d_{sensor} and the electron charge e

$$\text{N}_{\text{e-h}} = \frac{Q}{d_{\text{sensor}} \cdot e}. \tag{7.2}$$

For the ATLAS12EC miniature sensor with a thickness of 310 ± 25 µm this results in

$$\text{N}_{\text{e-h}} = (287 \pm 37)\ \text{electron} - \text{hole pairs per µm}.$$

This value is ~ 3.6 times higher than the average of 80 electron-hole pairs per µm produced by a MIP. This discrepancy occurs due to an imprecise signal loss compensation L_c, a possible impedance mismatch, noise fluctuations mainly due to ~ 30 cm long cables between sensor and amplifier, errors in the signal integral or additionally incoming low energetic shower particles.

Tests with the STRIDENAS Detector

Tests with the single-bonded strip sensor have shown that the ATLAS12EC miniature sensors, in combination with the above mentioned amplifier, are able to detect electrons coming from the DESY II Test Beam. To check the functionality of the STRIDENAS detector, tests with this device were performed. A bias voltage of -75 V was chosen due to the early breakdown of the sensor at around -100 V and to obtain a low leakage current. The STRIDENAS PCB was mounted in its holder, placed in the beam axis and shielded from light. One channel (corresponding to three strips grouped together) was connected to the amplifier and then read out by the oscilloscope. No signal was observed which confirms that the sensors are damaged, as already suspected from the occurrence of the early breakdown.

7.3.3 Conclusion

The ATLAS12EC miniature sensor is able to detect electrons at the DESY II Test Beam facility if a 40 dB amplifier is used. The signal-to-noise ratio was found to be 51. The average charge produced in the sensor was determined to be $Q = (1.43 \pm 0.14) \cdot 10^{-14}\,\mathrm{C}$, corresponding to a production of (287 ± 37) electron-hole pairs per µm. This value is ~ 3.6 times higher than the expected number from literature [13], which arises due to imperfections in the measurement setup and data analysis. Despite the amplifier no signal using the STRIDENAS detector could be observed. This result confirms that the sensors on the PCB are broken as already suspected from the observation of early breakdowns of the sensors at the probe station (Section 6.2). Previous attempts to identify the reason for this defect were unsuccessful. These checks included a detailed microscopic analysis of the bonded sensor to identify possible loose wires, smeared glue or surface damage of the sensors. Furthermore, the glue used to fix the sensors on the PCB was cross-checked and found to be well suited for this type of sensors. Another reason for the defects could be a pin hole (which might be visible with an infrared-camera [70], if enough heat is produced) or micro cracks in the sensor. This could be investigated by performing X-ray images of the sensors.

Chapter 8

Conclusion

The aim for size and cost reduction of particle accelerators has generated great interest in the development of novel acceleration techniques beyond the current radio frequency based technology. At the SINBAD facility at DESY, different techniques are foreseen to be investigated using the ARES electron linac. To proof that an energy gain was achieved with these techniques, the electron energy needs to be measured downstream of those novel acceleration structures. This is done using a spectrometer dipole to spatially spread out electrons with different energies and a beam profile monitor. In this thesis, a spectrometer setup particularly tailored to the energy measurement of electrons accelerated in dielectric laser accelerators (DLAs) was presented. For this task, the characterization of possible spectrometer dipoles was performed, and a dedicated beam profile monitor, called STRIDENAS, was developed as an internal DESY collaboration between the MPY-1 and FH-ATLAS group with the support of the detector development group of the University of Hamburg.

The spectrometer dipole needs to have a sufficient field quality and strength. The magnetic fields of two dipole candidates were measured in all spatial directions. Additionally, field measurements along the beam trajectory for different magnet strengths and a hysteresis measurement were performed. Based on this magnet characterization, it was shown that the PDE dipole fulfils all the requirements, whereas the DORIS dipole showed a high amount of fringe fields. Therefore, the PDE dipole was selected for the spectrometer and is currently under installation in the accelerator tunnel.

The development of a dedicated detector was motivated by the small volumes, with apertures in the μm range, of the DLAs. These sizes lead to electron beam charges in the sub-pC range and electron densities at the screen position below 7 electrons per μm^2 area. It is very challenging, to measure these low-charge electron distributions with conventional screens. Therefore, a dedicated detector called STRIDENAS was developed to perform this task. The design, development, test of single components and commissioning of a detector prototype was done within this master thesis.

The requirements on the detector were an active area larger than the expected beams at the detector location, a spatial resolution sufficient to resolve the beam features of interest, a high

dynamic range, to withstand the incoming electron intensity, to be remotely controllable and to be ultra-high vacuum compatible in the final setup. To achieve these requirements, the presented STRIDENAS design consists of two ATLAS12 miniature strip sensors with a 74.5 µm pitch. To estimate the produced charge in the sensor and investigate the spatial resolution, simulations based on the ROOT package, including the effects of thermal diffusion and an extra transverse spread to take the plasma effect into account, were performed for an expected 0.5 pC electron distribution at the detector location. The result shows a sufficient resolution of the beam features of interest. The readout was chosen to be done with charge-to-digital converters with a dual range system. In order to not saturate the readout, the charge should be below 36 fC per sensor readout channel. The sensors were characterized by performing current-voltage, capacitance-voltage and transient-current technique (TCT) measurements. The TCT measurements enabled an estimate of the signal shape and transverse spread dependence on the incoming particle intensity and bias voltage. The performed measurements show that below 7300 incoming MIPs per strip no problems are expected. This upper limit is given by the available laser light intensity of the experimental setup and not by critical effects observed on the sensor. Measurements showed that the reduction of the bias voltage results in a reduction of charge produced in the sensor. At the same time, the signal length increases and, therefore, makes this procedure less suitable for charge reduction.

The different STRIDENAS components were tested individually at the DESY II Test Beam facility in two measurement campaigns. The readout electronics were tested with a photomultiplier signal. Both ranges were working, resolving the pulses well and showing a sensitivity to an increase of incoming charge. Due to the single electron rate at the Test Beam, no signals could be observed with the sensors. Therefore, tests with an amplifier were performed. The STRIDENAS sensors suffered from an early breakdown and were not able to detect any electrons. Tests with an additional sensor on a different PCB with the amplifier were successful and able to measure single electrons from the Test Beam. Possible reasons for the early breakdown of the STRIDENAS sensors were investigated and discussed.

Within this thesis, the design and first prototype of the STRIDENAS detector as well as estimates on its performance based on simulations were presented. The sensors were characterized and the single components commissioned individually. Further steps towards the final implementation are presented in the following outlook.

Chapter 9

Outlook

For the final implementation at the ARES spectrometer, further studies are needed. Test of the sensor under a higher electron intensity would give an insight on the behaviour of the sensor under realistic conditions. Such studies are currently being performed inside the DESY II tunnel. The analysis of the acquired data, however, is not part of this thesis. The sensors are placed inside DESY II at the photon beam halo of one of the Test Beam beamlines. A target in front of the sensor is used to create electrons. At this location in the tunnel, a patch panel to the Test Beam area exists, which allows to operate and readout the signals outside of the tunnel. A photo of the experimental setup inside the tunnel is shown in Figure 9.1. Additionally, measurements could be performed by placing the sensor at the beam dump of DESY II. An electron intensity up to the maximum DESY II intensity of 10^{10} electrons would be available. Due to the location of the beam dump, the readout of the signals would need to be performed directly inside the tunnel to avoid long cables. The radiation shielding of the readout equipment adds an extra difficulty to this measurement. Alternatively to high intensity electron beams, TCT measurements with a high laser intensity could be performed. For these measurements, a laser intensity monitor as well as a spot size monitor would be beneficial to allow for a better comparison with electron beams.

To verify the functionality of the designed PCB, tests with a new sensor could be performed. These tests are of interest to check that the length of the wires on the PCB are unproblematic and sufficiently shielded. The implementation of one sensor with only a few bonded strips could be sufficient for these tests. Tests could either be performed at the DESY II Test Beam using the fast amplifier, inside the DESY II tunnel, or the PCB could be implemented in a TCT setup and tests could be performed with laser light.

The length of the readout cables increases the sensitivity to noise of the STRIDENAS detector. The performed measurements with the setup confirmed a high sensitivity to noise. The option to implement a simple low gain amplifier on the PCB close to the sensor strip readout, should therefore be studied, to ensure a better signal quality.

Tests combining the readout electronics with the sensor could be performed to investigate the response to signals produced by the sensor.

For the implementation at the ARES spectrometer, either a vacuum-compatible PCB needs to be designed or the installation after a vacuum window needs to be studied. The vacuum compatible PCB could be realized with a ceramic PCB. The cable feed-through to the readout electronics would need to be designed. For an installation after a vacuum window, the influence of the window in the electron beam quality needs to be studied. Detailed FLUKA or GEANT4 simulations of the particle-matter interaction would be needed. The sensor should be placed on a movable stage to be moved outside of the beam in order to avoid radiation damage. Additionally, this would have the benefit of aligning the sensor to the beam or scanning a larger beam area.

The current version of the readout software does not allow for simultaneous operation of all QDCs. The implementation of this feature is needed for the final operation.

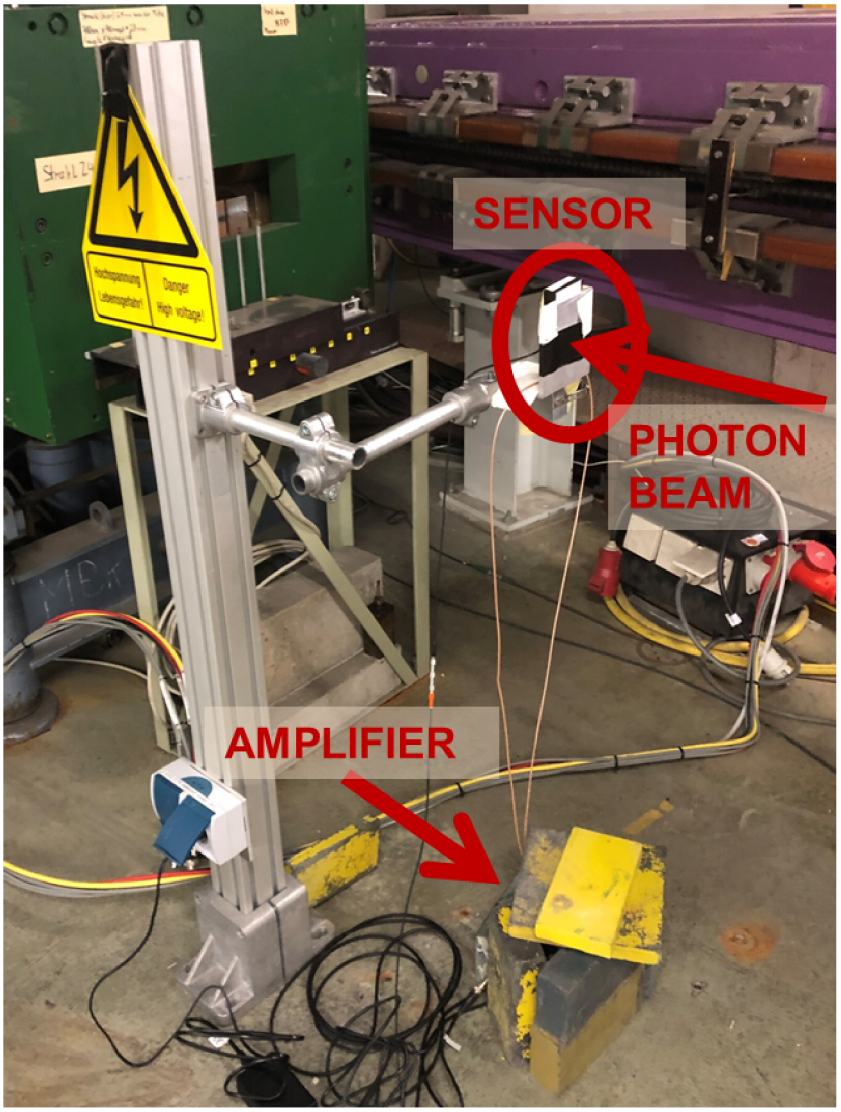

Figure 9.1: Experimental setup inside the DESY II tunnel.

Chapter 10

Acknowledgements

I would like to thank my supervisors Wolfgang Hillert and Florian Burkart as well as Ralph Assmann and Ulrich Dorda for supporting and enabling this project.
I would like to especially thank Florian Burkart for the supervision, answering many questions, helping with measurements, the trust with delicate components, organisation and design of detector parts and the chocolate when frustration got too high.
This project was realized in cooperation with the DESY FH-ATLAS group. In particular I would like to thank Marcel Stanitzki for taking interest in this project, many helpful meetings on the design, measurements and data analysis of the STRIDENAS detector, organising the ATLAS miniature sensors, providing further components, help with sensor specific simulations and analysis and the extra bit of fun at work.
I would like to thank Uwe Kraemer for helping and teaching how the sensor measurements are done in the FH E-Lab and preparing measurements at the Test Beam.
I would like to thank the Test Beam coordinators and everyone else involved for providing the beam time at the DESY II Test Beam as well as the needed equipment. I would like to thank Lennart Huth and Jan Dreyling-Eschweiler for all their help and support. I would further like to thank Florian Burkart, Marcel Stanitzki, Ralf Diener, Norbert Meyners, Uwe Kraemer, Willi Kuropka, Ángel Ferran Pousa, Sumera Yamin and Daniel Marx for setting up the experiment, installing beam triggers, taking shifts or transporting equipment.
I would like to thank Torsten Külper from the E-Lab for providing all the equipment and always helping out when we needed some special components.
I would like to thank Edo Rossi for helping with questions about the ATLAS12 mini sensors.
I would like to thank the detector research and development group of Erika Garutti for inspiring discussions about the plasma effect, providing their probe station and TCT setup for measurements as well as the bonding of the sensor for the TCT measurement and lending us their PCB for further measurements. With regards to the TCT measurements I would like to thank Finn Feindt for all the help and effort.
I would like to thank Ralf Apel for designing the PCB and everyone involved in bonding and gluing the sensors.

I would like to thank Jasmin Stein and Stefan Baark for designing and building the PCB holder.
I would like to thank Holger Sokolinski for helping with questions about our cables and connectors.
I would like to thank Matthias Thede and the rest of the team for all the help with measuring the DORIS dipole and PDE dipole as well as for the helpful discussions.
I would like to thank Frank Mayet for providing the electron beam distribution at the position of the detector for a possible ACHIP working point as well as the CAD model of the ARES linac.
I would like to thank Ángel Ferran Pousa for all the help with programming, inspiring discussions, motivation and proofreading.
I would like to thank Daniel Marx for all the helpful discussions on measurement uncertainties and rice cakes.
Finally I would like to thank my father for supporting my master and taking interest in these thesis (as well as already bringing me to DESY as a baby), my friends and my wonderful boyfriend for all the love and help I could wish for.

Bibliography

[1] O. Barbalat, "Applications of particle accelerators," tech. rep., CERN, 1990.

[2] M. Benedikt, P. Collier, V. Mertens, J. Poole, and K. Schindl, *LHC Design Report*. CERN Yellow Reports: Monographs, Geneva: CERN, 2004.

[3] CERN Accelerating science . `https://home.cern/resources/faqs/facts-and-figures-about-lhc`. Accessed: 2019-06-25.

[4] K. G. Steffen, "High energy beam optics," 1965.

[5] H. Wiedemann *et al.*, *Particle accelerator physics*, vol. 314. Springer, 2007.

[6] J. Rossbach and P. Schmueser, "Basic course on accelerator optics," in *Conf. Proc.*, vol. 9209071, pp. 17–88, 1992.

[7] K. Floettmann, "Some basic features of the beam emittance," *Physical Review Special Topics-Accelerators and Beams*, vol. 6, no. 3, p. 034202, 2003.

[8] K. Wille, *The physics of particle accelerators: an introduction*. Oxford University Press, 2000.

[9] J. Holmes, S. Henderson, and Y. Zhang, "Magnetic Fields and Magnet Design," *USPAS, Vanderbilt*, 2009.

[10] ATLAS Collaboration, "Technical design report for the ATLAS inner tracker strip detector," tech. rep., 2017.

[11] V. Karimäki, "The CMS tracker system project: Technical Design Report," tech. rep., CMS-TDR-005, 1997.

[12] H. Kolanoski and N. Wermes, *Teilchendetektoren*. Springer, 2016.

[13] H. Spieler, *Semiconductor detector systems*, vol. 12. Oxford university press, 2005.

[14] M. Tanabashi, K. Hagiwara, K. Hikasa, K. Nakamura, Y. Sumino, F. Takahashi, J. Tanaka, K. Agashe, G. Aielli, C. Amsler, *et al.*, "Review of particle physics," *Physical Review D*, vol. 98, no. 3, p. 030001, 2018.

[15] K. Nakamura, Particle Data Group, *et al.*, "Review of particle physics," *Journal of Physics G: Nuclear and Particle Physics*, vol. 37, no. 7A, p. 075021, 2010.

[16] H. Spieler, "Introduction to radiation detectors and electronics," *IV. Energy Deposition in the Detector and Spectrum Formation*, 1998.

[17] F. Scholze, H. Henneken, P. Kuschnerus, H. Rabus, M. Richter, and G. Ulm, "Determination of the electron–hole pair creation energy for semiconductors from the spectral responsivity of photodiodes," *Nuclear Instruments and Methods in Physics Research Section A: Accelerators, Spectrometers, Detectors and Associated Equipment*, vol. 439, no. 2-3, pp. 208–215, 2000.

[18] M. A. Green, "Self-consistent optical parameters of intrinsic silicon at 300 K including temperature coefficients," *Solar Energy Materials and Solar Cells*, vol. 92, no. 11, pp. 1305–1310, 2008.

[19] F. Berghmans, B. Brichard, A. F. Fernandez, A. Gusarov, M. Van Uffelen, and S. Girard, "An introduction to radiation effects on optical components and fiber optic sensors," in *Optical waveguide sensing and imaging*, pp. 127–165, Springer, 2008.

[20] S. Ramo, "Currents induced by electron motion," *Proceedings of the IRE*, vol. 27, no. 9, pp. 584–585, 1939.

[21] M. Campbell, E. Heijne, T. Holỳ, J. Idárraga, J. Jakubek, C. Lebel, C. Leroy, X. Llopart, S. Pospíšil, L. Tlustos, *et al.*, "Study of the charge sharing in a silicon pixel detector by means of α-particles interacting with a Medipix2 device," *Nuclear Instruments and Methods in Physics Research Section A: Accelerators, Spectrometers, Detectors and Associated Equipment*, vol. 591, no. 1, pp. 38–41, 2008.

[22] J. Becker, K. Gärtner, R. Klanner, and R. Richter, "Simulation and experimental study of plasma effects in planar silicon sensors," *Nuclear Instruments and Methods in Physics Research Section A: Accelerators, Spectrometers, Detectors and Associated Equipment*, vol. 624, no. 3, pp. 716–727, 2010.

[23] J. Becker, D. Eckstein, R. Klanner, and G. Steinbrueck, "Impact of plasma effects on the performance of silicon sensors at an X-ray FEL," *Nuclear Instruments and Methods in Physics Research Section A: Accelerators, Spectrometers, Detectors and Associated Equipment*, vol. 615, no. 2, pp. 230–236, 2010.

[24] W. Seibt, K.-E. Sundström, and P. Tove, "Charge collection in silicon detectors for strongly ionizing particles," *Nuclear Instruments and Methods*, vol. 113, no. 3, pp. 317–324, 1973.

[25] R. N. Williams and E. M. Lawson, "The plasma effect in silicon semiconductor radiation detectors," *Nuclear Instruments and Methods*, vol. 120, no. 2, pp. 261–268, 1974.

[26] U. Dorda, B. Marchetti, J. Zhu, F. Mayet, W. Kuropka, T. Vinatier, G. Vashchenko, K. Galaydych, P. Walker, D. Marx, *et al.*, "Status and objectives of the dedicated accelerator R&D facility "SINBAD" at DESY," *Nuclear Instruments and Methods in Physics Research Section A: Accelerators, Spectrometers, Detectors and Associated Equipment*, vol. 909, pp. 239–242, 2018.

[27] "ATHENA." `https://www.athena-helmholtz.de/home/index_ger.html`. Accessed: 2019-06-06.

[28] F. Kärtner, F. Ahr, A.-L. Calendron, H. Çankaya, S. Carbajo, G. Chang, G. Cirmi, K. Dörner, U. Dorda, A. Fallahi, *et al.*, "AXSIS: Exploring the frontiers in attosecond X-ray science, imaging and spectroscopy," *Nuclear Instruments and Methods in Physics Research Section A: Accelerators, Spectrometers, Detectors and Associated Equipment*, vol. 829, pp. 24–29, 2016.

[29] J. Zhu, R. W. Assmann, M. Dohlus, U. Dorda, and B. Marchetti, "Sub-fs electron bunch generation with sub-10-fs bunch arrival-time jitter via bunch slicing in a magnetic chicane," *Phys. Rev. Accel. Beams*, vol. 19, p. 054401, May 2016.

[30] J. Zhu, *Design study for generating sub-femtosecond to femtosecond electron bunches for advanced accelerator development at SINBAD*. PhD thesis, 2017.

[31] K. Wootton *et al.*, "Towards a Fully Integrated Accelerator on a Chip: Dielectric Laser Acceleration (DLA) From the Source to Relativistic Electrons," in *Proc. of International Particle Accelerator Conference (IPAC'17), Copenhagen, Denmark, 14-19 May, 2017*, no. 8 in International Particle Accelerator Conference, (Geneva, Switzerland), pp. 2520–2525, JACoW, May 2017. https://doi.org/10.18429/JACoW-IPAC2017-WEYB1.

[32] F. Mayet, R. Aßmann, U. Dorda, W. Kuropka, B. Marchetti, and J. Zhu, "Simulations and Plans for a Dielectric Laser Acceleration Experiment at SINBAD," in *Proc. of International Particle Accelerator Conference (IPAC'17), Copenhagen, Denmark, 14-19 May, 2017*, no. 8 in International Particle Accelerator Conference, (Geneva, Switzerland), pp. 3264–3267, JACoW, May 2017. https://doi.org/10.18429/JACoW-IPAC2017-WEPVA007.

[33] F. Mayet, R. Assmann, J. Boedewadt, R. Brinkmann, U. Dorda, W. Kuropka, C. Lechner, B. Marchetti, and J. Zhu, "Simulations and plans for possible DLA experiments at SINBAD," *Nuclear Instruments and Methods in Physics Research Section A: Accelerators, Spectrometers, Detectors and Associated Equipment*, vol. 909, pp. 213–216, 2018.

[34] S. Bayesteh and H. Delsim-Hashemi, "Diagnostics of Femtosecond Low-Charge Electron Bunches at Regae," *Proceedings of IPAC*, p. 1192, 2011.

[35] A. Jantzen-Stenzel, "DORIS III Dipole Data Sheet."

[36] Budker Institute of Nuclear Physic Novosibirsk, "Certificate of dipole PDE04," 2013.

[37] SENIS GmbH, "Data Sheet, Rev.03a," 2007.

[38] Deutsches Elektronen-Synchrotron, "DORIS - A particle accelerator makes scientific history," 2013.

[39] D. Dubbers, "Simple formula for multiple mu-metal shields," *Nuclear Instruments and Methods in Physics Research Section A: Accelerators, Spectrometers, Detectors and Associated Equipment*, vol. 243, no. 2, pp. 511 – 517, 1986.

[40] ATLAS Upgrade Strip Sensor Collaboration *et al.*, "Supply of Silicon Microstrip Sensors of ATLAS12EC Specification," tech. rep., 2012.

[41] "Hamatsu Photonics." `http://www.hamamatsu.com/`. Accessed: 2019-03-29.

[42] Y. Unno, A. Affolder, P. Allport, R. Bates, C. Betancourt, J. Bohm, H. Brown, C. Buttar, J. Carter, G. Casse, *et al.*, "Development of n-on-p silicon sensors for very high radiation environments," *Nuclear Instruments and Methods in Physics Research Section A: Accelerators, Spectrometers, Detectors and Associated Equipment*, vol. 636, no. 1, pp. S24–S30, 2011.

[43] Y. Unno, S. Edwards, S. Pyatt, J. Thomas, J. Wilson, J. Kierstead, D. Lynn, J. Carter, L. Hommels, D. Robinson, *et al.*, "Development of n+-in-p large-area silicon microstrip sensors for very high radiation environments–ATLAS12 design and initial results," *Nuclear Instruments and Methods in Physics Research Section A: Accelerators, Spectrometers, Detectors and Associated Equipment*, vol. 765, pp. 80–90, 2014.

[44] C. Bertella, C. Escobar, G. Gariano, A. Gaudiello, G. Gemme, S. Katunin, A. Lapertosa, M. Miñano, A. Rovani, E. Ruscino, *et al.*, "Study of damages induced on ATLAS Silicon by fast extracted and intense proton beam irradiation," *Nuclear Instruments and Methods in Physics Research Section A: Accelerators, Spectrometers, Detectors and Associated Equipment*, 2018.

[45] "Study of damages induced on ATLAS silicon by fast extracted and intense proton beam irradiation." `https://indico.ihep.ac.cn/event/8414/session/8/contribution/81/material/slides/0.pdf`. Accessed: 2019-04-02.

[46] Polytek, "Datenblatt EPO-TEK H20E," Version 2, 11/01.

[47] CAEN, "Mod, V965/V965A 16/8 Ch. Dual Range QDC," *Technical Information Manual*, vol. 29.

[48] CAEN Electronic Instr. private communication, 2019.

[49] "CAEN V965 16 Channel Dual Range Multievent QDC." https://www.caen.it/products/v965/.

[50] CAEN, "Mod, V2718 VME-PCI Optical Link Bridge," *User's Manual*, vol. 11.

[51] "LEMO Catalogue." https://www.lemo.com/catalog/ROW/German/cable_catalog_p7.pdf. Accessed: 2019-04-01.

[52] C. Weddigen and W. Jüngst, *Elektronik: eine Einführung für Naturwissenschaftler und Ingenieure mit Beispielen zur Computer-Simulation*. Springer-Verlag, 1993.

[53] R. Brun and F. Rademakers, "ROOT—an object oriented data analysis framework," *Nuclear Instruments and Methods in Physics Research Section A: Accelerators, Spectrometers, Detectors and Associated Equipment*, vol. 389, no. 1-2, pp. 81–86, 1997.

[54] K. Floettmann *et al.*, "ASTRA: A space charge tracking algorithm," *Manual*, vol. 3, 2011.

[55] H. Bichsel, "Straggling in thin silicon detectors," *Reviews of Modern Physics*, vol. 60, no. 3, p. 663, 1988.

[56] Keithley Instruments, Inc., "Model 6517B Electrometer User Manual." http://download.tek.com/manual/6517B-900-01--A-Jun2008--User.pdf. Accessed: 2019-06-25.

[57] "Keysight | E4980A Precision LCR Meter 20 Hz to 2 MHz, E4980AL Precision LCR Meter 20 Hz to 300 kHz/500 kHz/1 MHz – Data Sheet." https://literature.cdn.keysight.com/litweb/pdf/5989-4435EN.pdf. Accessed: 2019-05-15.

[58] "Keithley 2400 series user manual." http://research.physics.illinois.edu/bezryadin/labprotocol/Keithley2400Manual.pdf. Accessed: 2019-04-10.

[59] J. Becker, *Signal development in silicon sensors used for radiation detection*. PhD thesis, 2010.

[60] F. Feindt, "Edge-TCT for the investigation of radiation damaged silicon strip sensors," Master's thesis, 2017.

[61] A. Siegman, *Lasers*. University Science Books, 1986.

[62] "Refractive Index of Si, Silicon." https://www.filmetrics.com/refractive-index-database/Si/Silicon. Accessed: 2019-05-14.

[63] R. Diener, J. Dreyling-Eschweiler, H. Ehrlichmann, I.-M. Gregor, U. Kötz, U. Krämer, N. Meyners, N. Potylitsina-Kube, A. Schütz, P. Schütze, *et al.*, "The DESY II test beam facility," *Nucl. Instr. Meth.*, vol. 922, pp. 265–286, 2019.

[64] H. Jansen, S. Spannagel, J. Behr, A. Bulgheroni, G. Claus, E. Corrin, D. Cussans, J. Dreyling-Eschweiler, D. Eckstein, T. Eichhorn, *et al.*, "Performance of the EUDET-type beam telescopes," *EPJ Techniques and Instrumentation*, vol. 3, p. 7, Oct 2016.

[65] "MSO5000B, DPO5000B Series Datasheet ." https://de.tek.com/datasheet/mixed-signal-oscilloscopes. Accessed: 2019-06-30.

[66] "3390 Arbitrary Waveform Generator." https://www.tek.com/product-support?series=3390%20Arbitrary%20Waveform%20Generator. Accessed: 2019-06-23.

[67] "Hamamatsu Photosensor Modules H11900/H11901 series." https://www.hamamatsu.com/resources/pdf/etd/H11900_H11901_TPMO1076E.pdf. Accessed: 2019-06-17.

[68] Marcel Stanitzki and Katja Krüger. private communication, 2019.

[69] "Datasheet Femto HSA-X-1-40." https://www.femto.de/images/pdf-dokumente/de-hsa-x-1-40.pdf. Accessed: 2019-06-23.

[70] A. Voronin, "Visualisierung von schäden an siliziumsensoren unter verwendung einer ccd-kamera," 2014. Karlsruher Institut für Technologie (KIT), Bachelorarbeit, 2014.

Appendix A

Additional Fieldmaps

DORIS Dipole

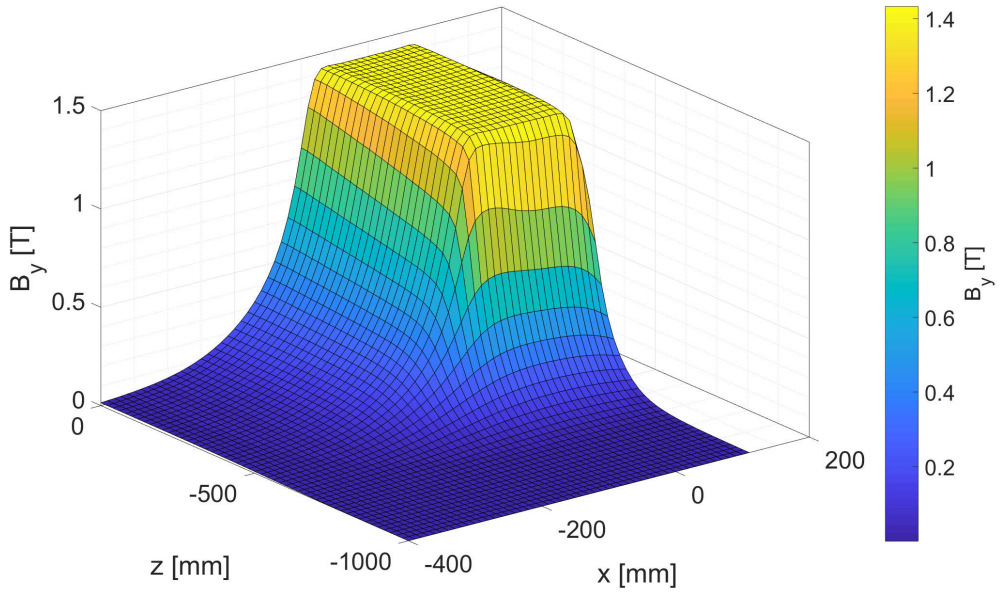

(a) Fieldmap of the B_y component [T] of the DORIS dipole measured at −940 A and y= 15 mm.

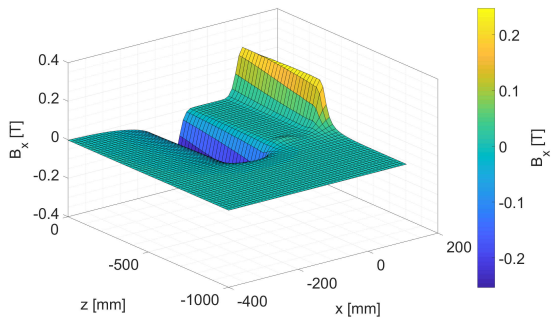

(b) Fieldmap of the B_x component [T] of the DORIS dipole measured at −940 A and y = 15 mm.

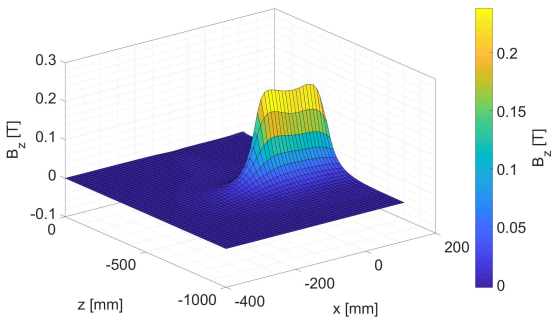

(c) Fieldmap of the B_z component [T] of the DORIS dipole measured at −940 A and y = 15 mm.

Figure A.1: Fieldmap at y = 15 mm.

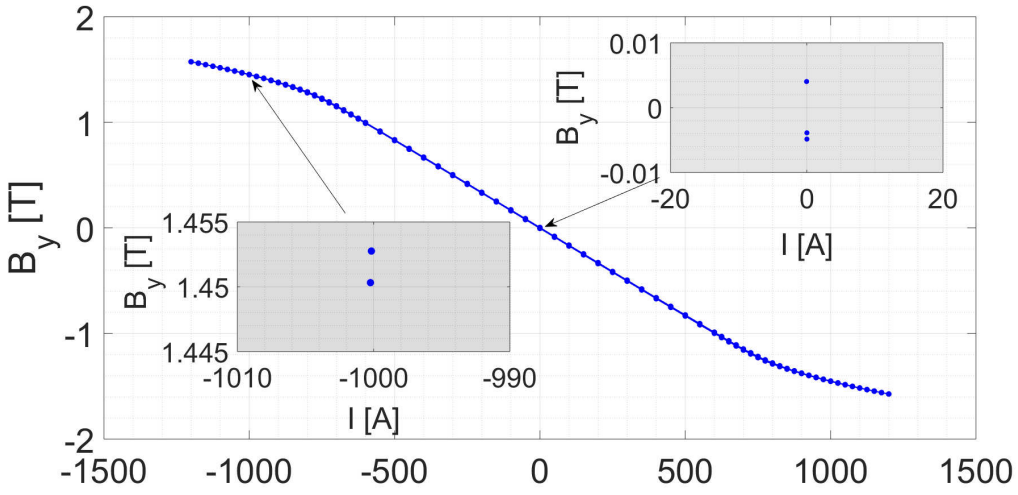

Figure A.2: Measured hysteresis curve of the DORIS dipole between 0 A and ± 1200 A.

PDE Dipole

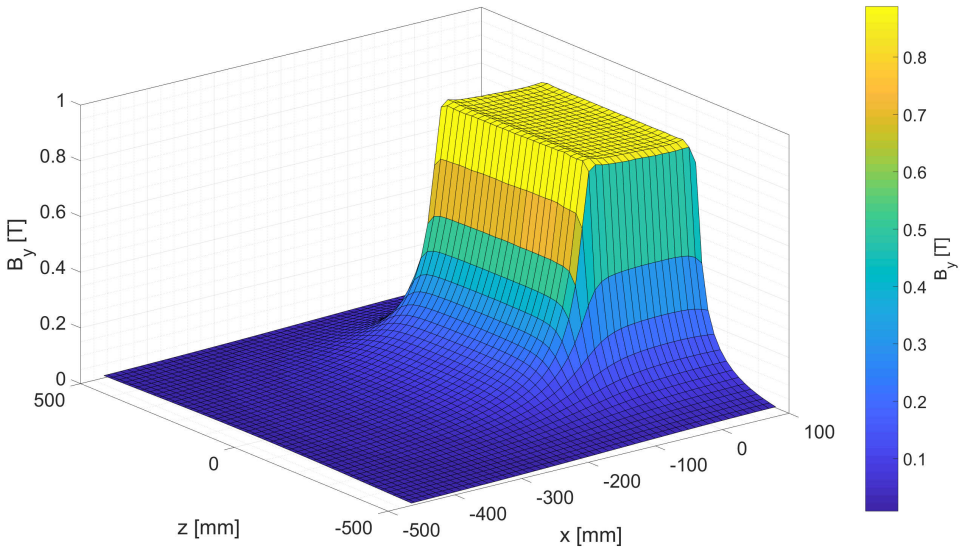

(a) Fieldmap of the B_y component [T] of the PDE dipole measured at 600 A and $y = 15$ mm.

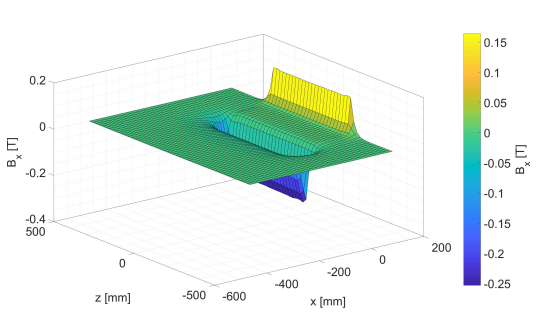

(b) Fieldmap of the B_x component [T] of the PDE dipole measured at 600 A and $y = 15$ mm.

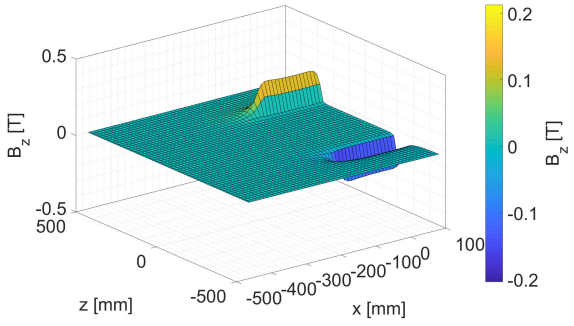

(c) Fieldmap of the B_z component [T] of the PDE dipole measured at 600 A and $y = 15$ mm.

Figure A.3: Fieldmap at $y = 15$ mm.

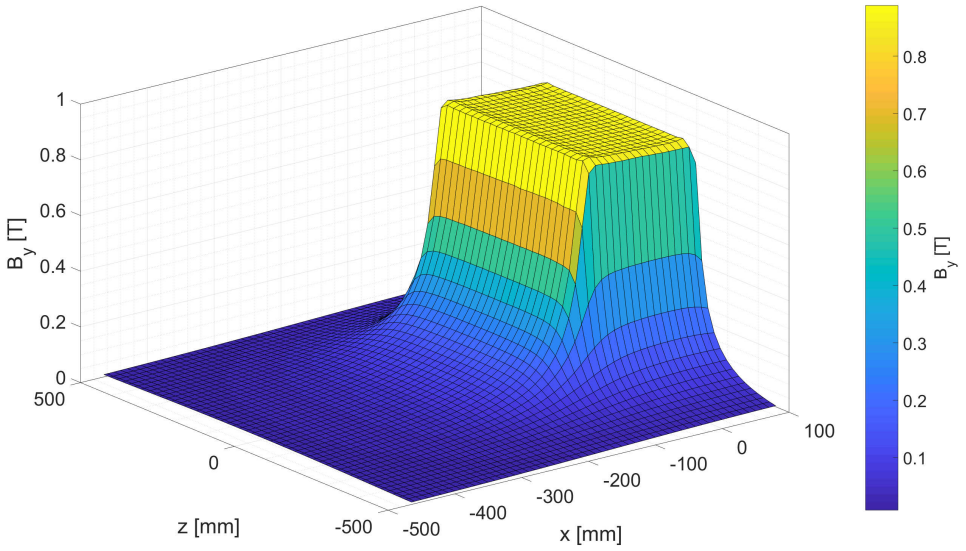

(a) Fieldmap of the B_y component [T] of the PDE dipole measured at 600 A and $y = -15$ mm.

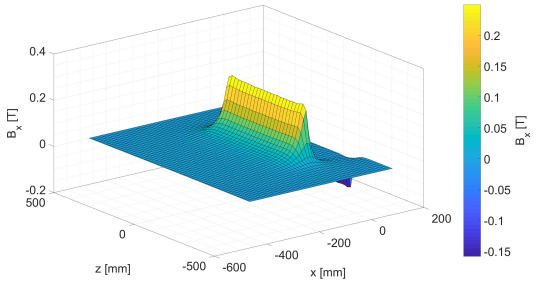

(b) Fieldmap of the B_x component [T] of the PDE dipole measured at 600 A and $y = -15$ mm.

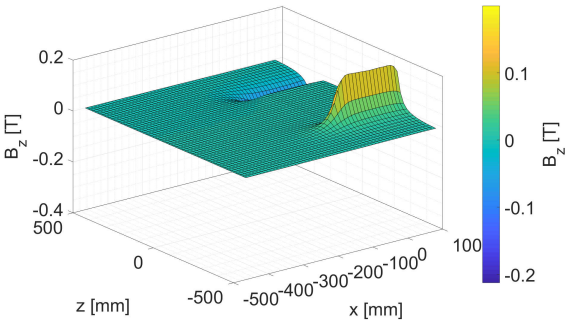

(c) Fieldmap of the B_z component [T] of the PDE dipole measured at 600 A and $y = -15$ mm.

Figure A.4: Fieldmap at $y = -15$ mm.

Appendix B

Probe Station Check

During the first measurement run of the ATLAS12EC miniature sensors at the FH E-Lab both available sensors were damaged. Since one of the sensors was damaged due to a spark produced while connecting the needle of the probe station to the sensors, a dedicated testing of the probe station was performed.

- The process of the previously performed measurements was reproduced. No problems or mistakes were observed while connecting the needle. While performing the measurements it was seen that both sensors are broken due to an early breakdown after a few volts.
- For a second check, a measurement of a p-type diode was performed. The measurement as well as the diode behaved as expected. An IV measurement with and without guard ring were performed and looked as expected.
- Problems with sparks were also reported from another measurement and a floating of the Keithley was suspected to create a potential on the needle. Therefore it was agreed to manually set the Keithley to 0 V before connecting the needle to the sensor.
- This procedure did not prevent further sparks. Therefore a new IV/CV box was build.
- Also with this new box sparks were observed. Therefore the current procedure foresees all measuring and powering devices to be switched off when the needle is connected. So far this procedure prevented further sparks. However, it disables the calibration of the capacitance measurements since for an open measurement the probe station needle needs to be disconnected and then connected again to the sensor without the Agilent being switched off.

Appendix C

Particle Showers

When high energetic electrons, positrons or photons pass through matter, electromagnetic showers are produced. These showers are mainly characterized by the alternating emission of photons by the electrons and positrons as well as the electron-positron pair production by the photons. The characteristics of the shower depend on the energy of the incoming particle as well as the material properties of the traversed material [12]. Important shower parameters based on shower models presented in the book Teilchendetektoren by Kolanoski and Wermes [12] are briefly discussed. These models are only approximations, more accurate information can be obtained by simulations.
The shower maximum of an electro-magnetic shower is given by

$$S_{\max} = ln(\frac{E_{\text{Incoming}}}{E_C}), \tag{C.1}$$

where E_{Incoming} is the energy of the incoming particle and E_C is the critical energy. For a solid the critical energy is given by

$$E_C = \frac{610MeV}{Z+1.24}, \tag{C.2}$$

where Z is the atomic number of the shower material.
The radiation length X_0 of a material is a measure of the point where the energy of the incoming particle is reduces to $1/\text{e}$ of its original value. By multiplying the shower maximum $S_{\max}$ with the radiation length X_0 one obtains the point of the shower maximum in cm.
To characterize the width of a shower, the Moliere radius r_{Molier} is used. It is defined as the radius which contains 90% of the shower and is given by

$$r_{\text{Molier}} = 21.2\text{MeV}\frac{X_0}{E_C}. \tag{C.3}$$

For the use at the Test Beam specific cases were studied and are presented in Table C.1.

Table C.1: Shower parameter calculations for different beam energies.

Beam Energy	**Material**	**Z**	$\mathbf{E_C}$ **[MeV]**	$\mathbf{S_{max}}$	$\mathbf{X_0}$ **[cm]**	$\mathbf{S_{max} \cdot X_0}$ **[cm]**	$\mathbf{r_{Molier}}$ **[cm]**
1.8 GeV	Fe	26	22.39	4.39	1.76	7.73	1.67
2 GeV	Fe	26	22.39	4.49	1.76	7.90	1.67
4 GeV	Fe	26	22.39	5.19	1.76	9.13	1.67

Appendix D

Characterization of Readout Electronics

Detailed characterization tests of the CAEN V965 charge-to-digital converters were performed. All charge-to-digital converters used during this master thesis were characterized. A list of all QDC, their serial number and their names is shown in Table D.1. An Arbitrary Waveform Generator (Keithley 3390) [66] was used to create the gate signals for these characterization tests. The measurement parameters are listed in Table D.2.

The QDCs were controlled by a computer. Input gate signals of different widths were sent to the QDC. All QDC channel inputs were unconnected and the noise of this setup was measured. One QDC was characterized at a time. The signal of all QDC channels for both ranges were recorded and saved in histograms of ADC counts. One ADC count corresponds to a certain amount of integrated charge. This value depends on the chosen QDC range. In total there are 4096 ADC count bins. In the user manual a gain of 25 fC per ADC count for the low range and 200 fC per count for the high range are stated [49]. The ADC count of the noise mean value was determined by using a Gaussian fit. The uncertainty on the value is given by the fit uncertainty. The following studies were performed for all QDCs, all QDC channels and both QDC ranges:

- The ADC count for the mean for all QDC channels at different gate widths are displayed for both QDC ranges. Data of even QDC channels correspond to the high range data, uneven QDC channels correspond to the low range data.
- The uniformity of the acquired values among the channels (interchannel uniformity) was determined. The standard deviation (STD) of the mean values of the acquired noise was taken. In addition, its percentage on the average of the noise means is displayed.

Table D.1: List of all QDCs with serial number, base address and name.

Serial Number	**Base Address**	**Name**
2867	1D00	QDC 1
2789	0003	QDC 2
2787	0011	QDC 3
2794	0013	QDC 4

Table D.2: List of measurement parameters for the QDC characterization tests.

Parameter	Unit	Value
Gate signal amplitude	mV	−800 (NIM)
Gate signal repetition rate	kHz	10
Pulse edge time	ns	5
Number of events (gate pulses) per measurement run		2 million
QDC pedestal current I_{ped}		100

- The dependence of the mean value ADC count on the gate width is shown for one channel of each range. The uncertainty on the gate width is given by the accuracy of the gate generator and is stated as 0.3 ns + 10^{-7} × gate width [66].
- The noise spread is displayed in terms of the standard deviation of the Gaussian fit. Its dependence on the gate width is displayed for one channel in both ranges.

Gate Width Scan of All Channels

The QDC scan with gate widths of 30 ns, 60 ns, 90 ns, 150 ns, 300 ns, 600 ns, 1 µs, 5 µs and 15 µs are shown in Figure D.1 to D.8. Measurements are displayed for each QDC and range individually. For the low range measurements, no data for the 5 µs and 15 µs gates are available due to saturation of the channels.
The interchannel uniformities are displayed in Table D.3 to D.6.

QDC 1

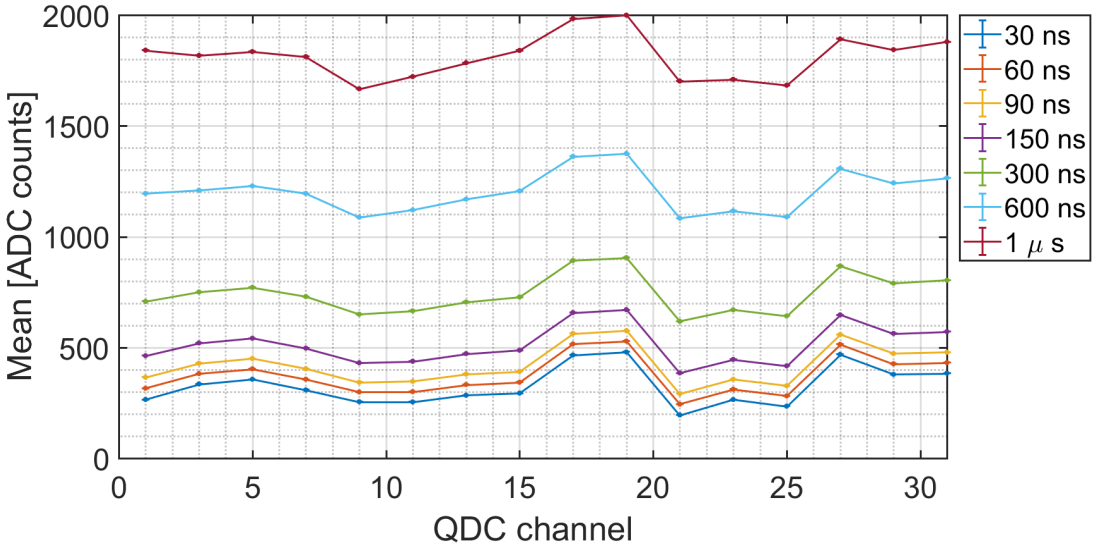

Figure D.1: Mean value of the acquired noise for different gate widths for the low range of QDC 1.

Table D.3: Interchannel quality of QDC 1.

	Low range		High range	
Gate width	**STD [Counts]**	**STD / Mean [%]**	**STD [Counts]**	**STD / Mean [%]**
30 ns	88	27	11	25
60 ns	88	24	11	22
90 ns	88	21	11	20
150 ns	89	17	11	17
300 ns	89	12	11	12
600 ns	92	8	11	7
1 µs	99	5	12	5
5 µs	-	-	30	3
15 µs	-	-	85	3

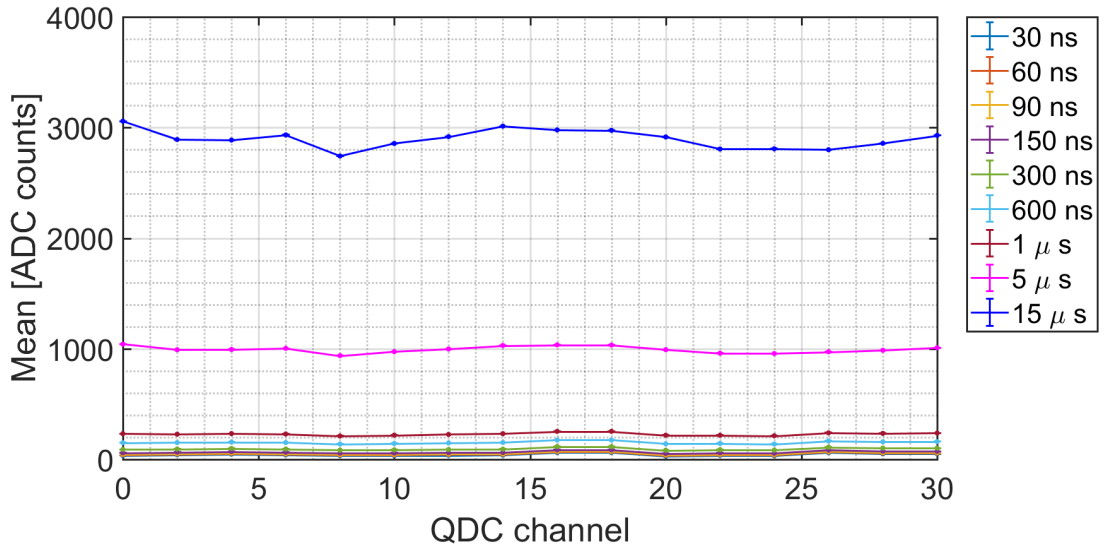

Figure D.2: Mean value of the acquired noise for different gate widths for the high range of QDC 1.

QDC 2

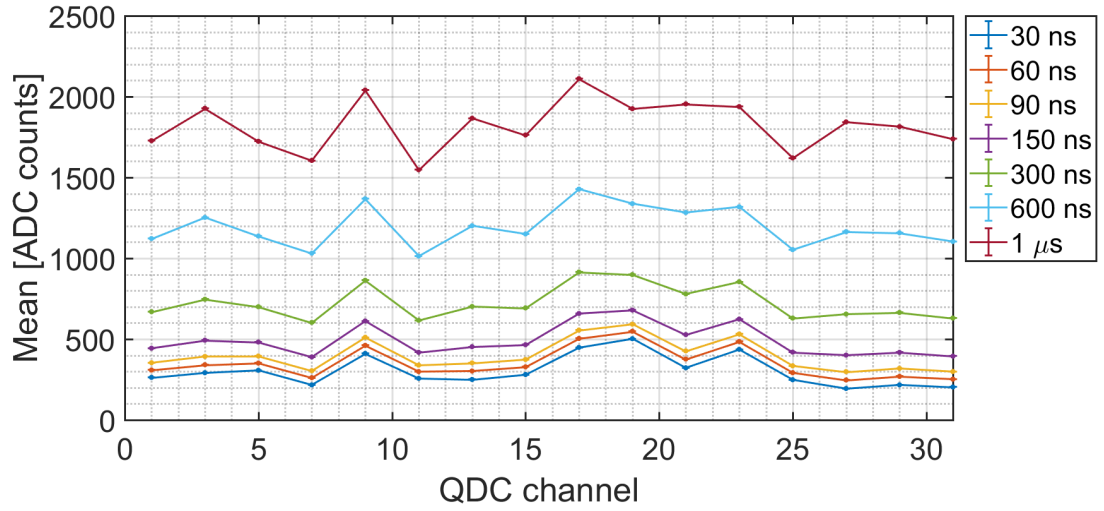

Figure D.3: Mean value of the acquired noise for different gate widths for the low range of QDC 2.

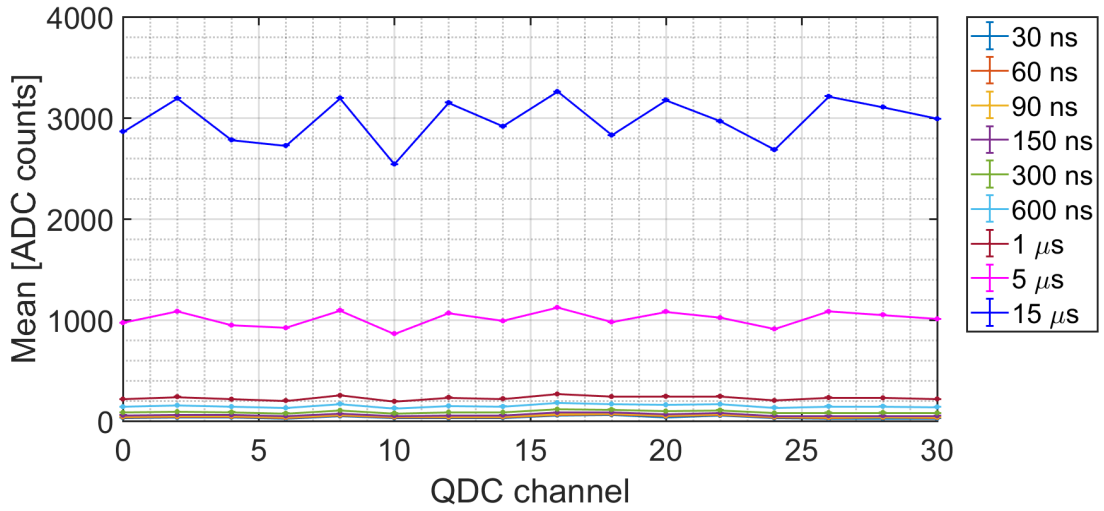

Figure D.4: Mean value of the acquired noise for different gate widths for the high range of QDC 2.

Table D.4: Interchannel quality of QDC 2.

	Low range		High range	
Gate width	**STD [Counts]**	**STD / Mean [%]**	**STD [Counts]**	**STD / Mean [%]**
30 ns	96	32	12	32
60 ns	96	27	12	28
90 ns	97	24	12	24
150 ns	98	20	12	20
300 ns	105	14	13	14
600 ns	124	10	16	10
1 µs	159	9	20	9
5 µs	-	-	76	8
15 µs	-	-	221	7

QDC 3

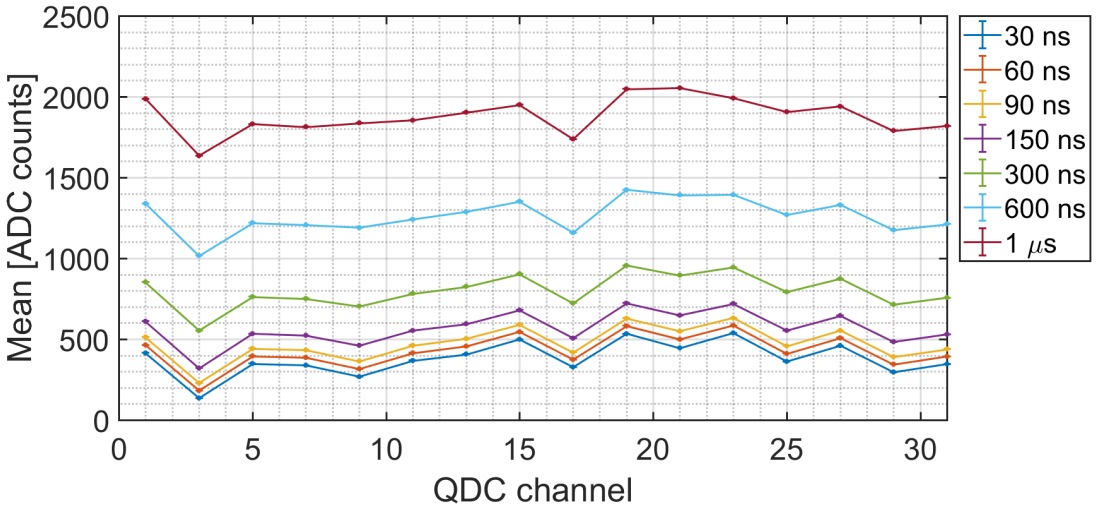

Figure D.5: Mean value of the acquired noise for different gate widths for the low range of QDC 3.

Table D.5: Interchannel quality of QDC 3.

	Low range		High range	
Gate width	**STD [Counts]**	**STD / Mean [%]**	**STD [Counts]**	**STD / Mean [%]**
30 ns	104	27	13	25
60 ns	104	24	13	23
90 ns	104	22	13	20
150 ns	104	18	13	17
300 ns	104	13	13	13
600 ns	107	8	13	8
1 µs	113	6	14	6
5 µs	-	-	35	3
15 µs	-	-	99	3

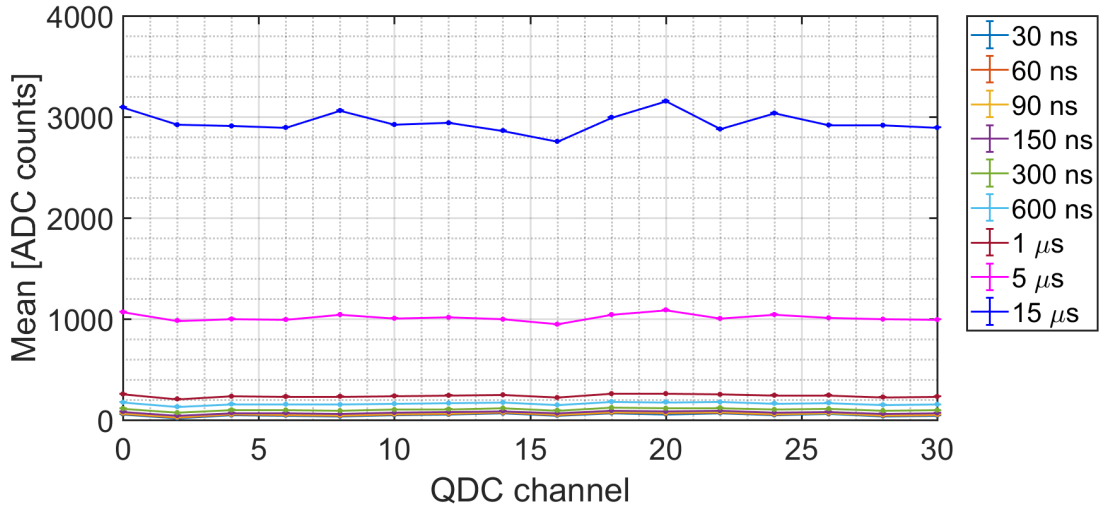

Figure D.6: Mean value of the acquired noise for different gate widths for the high range of QDC 3.

QDC 4

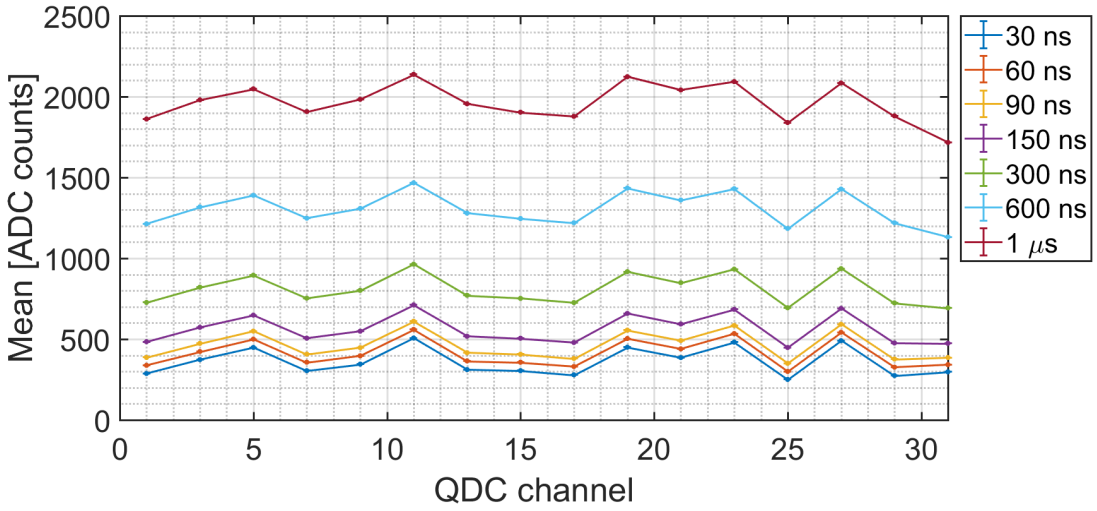

Figure D.7: Mean value of the acquired noise for different gate widths for the low range of QDC 4.

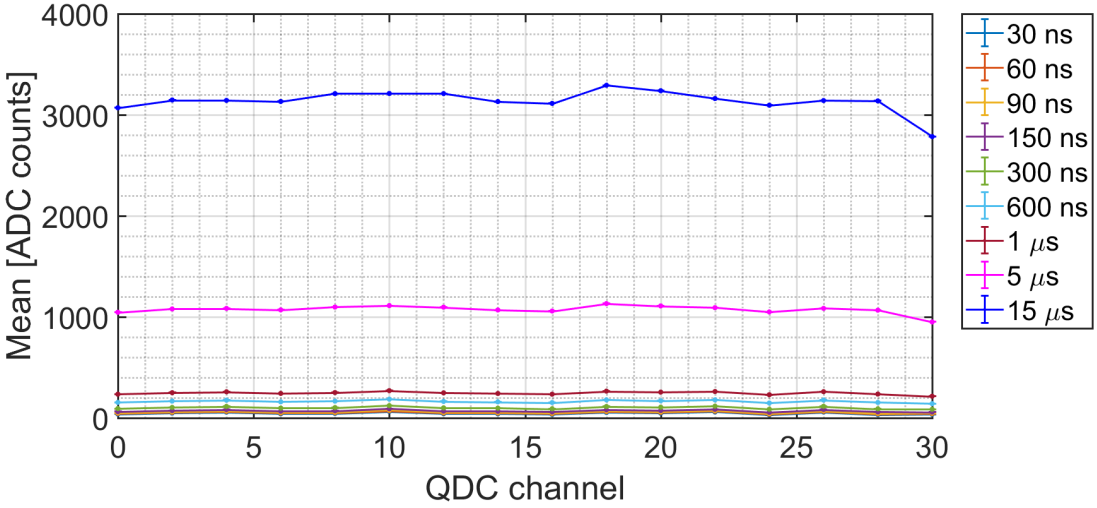

Figure D.8: Mean value of the acquired noise for different gate widths for the high range of QDC 4.

For all four QDCs an increase of the mean ADC counts with increasing gate width can be observed. This is expected since an increased gate width corresponds to a longer charge integration time. For the low range channels, the mean ADC counts are higher compared to the corresponding high range values as expected from the different resolutions of the ranges.
The interchannel uniformity varies strongly for different gate widths between 3% and 32% with increasing values for smaller gate widths. The CAEN user manual states an interchannel gain uniformity below $\pm$ 4% [49] where the interchannel gain uniformity is defined as the uniformity of the acquired values among the channels.

Table D.6: Interchannel quality of QDC 4.

	Low range		High range	
Gate width	**STD [Counts]**	**STD / Mean [%]**	**STD [Counts]**	**STD / Mean [%]**
30 ns	87	24	11	23
60 ns	88	21	11	20
90 ns	89	19	11	18
150 ns	90	16	11	15
300 ns	94	12	12	11
600 ns	103	8	13	8
1 µs	118	6	15	6
5 µs	-	-	40	4
15 µs	-	-	110	4

Mean ADC count dependence on gate width

The dependence for the mean ADC count on the gate width for one QDC channel in low and high range was determined. QDC channel 2 was chosen for the low range and QDC channel 3 for the high range channel. Both channels correspond to the same QDC input. The results for all QDC are displayed below. The dependence was found to be linear as expected for all QDC and both ranges and stated in the user manual. A non zero value for gate widths with 0 s can be observed when interpolating the data points. This might be caused by the pedestal current I_{ped} of the QDC. It is needed for the current-to-current converter of the QDC to operate in a linear regime and allow for small positive input values [47]. This pedestal current is then integrated by a capacitor and gives the ADC count values.

QDC 1

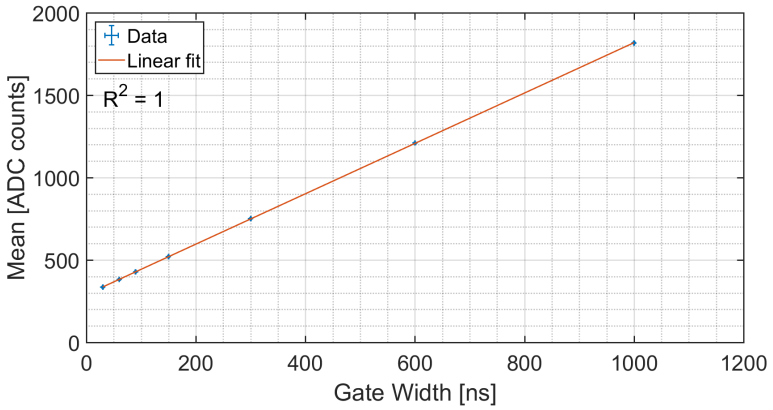

Figure D.9: Dependence of the noise mean value on the gate width for one channel of QDC 1 in low range.

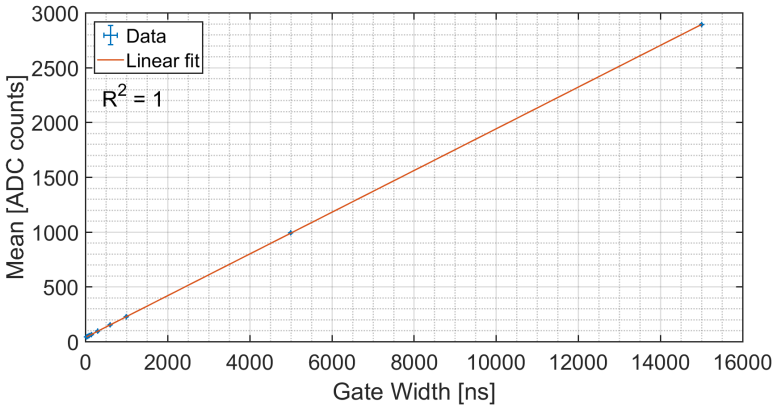

Figure D.10: Dependence of the noise mean value on the gate width for one channel of QDC 1 in high range.

QDC 2

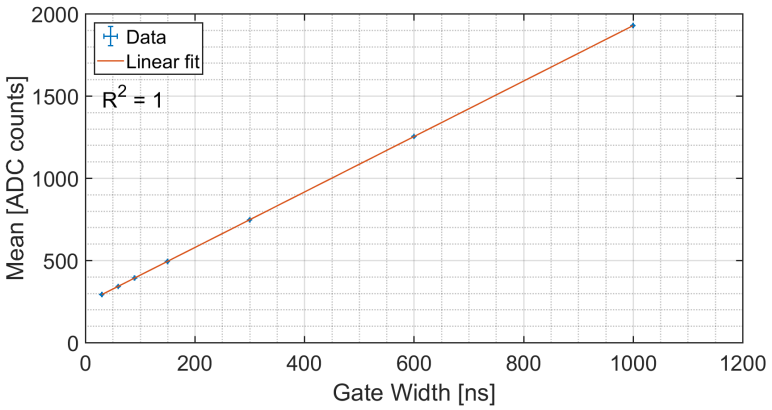

Figure D.11: Dependence of the noise mean value on the gate width for one channel of QDC 2 in low range.

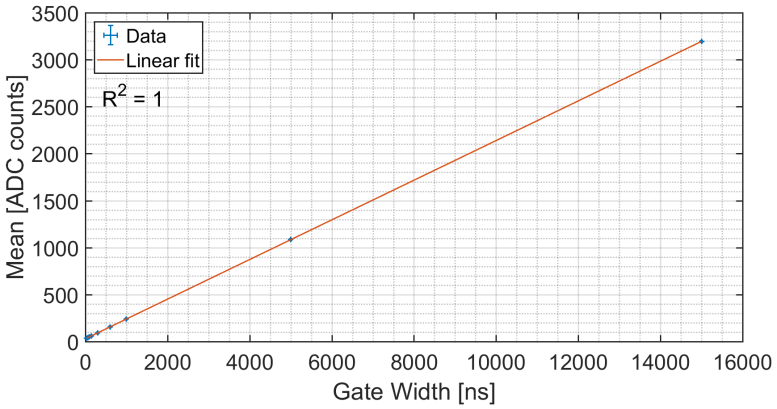

Figure D.12: Dependence of the noise mean value on the gate width for one channel of QDC 2 in high range.

QDC 3

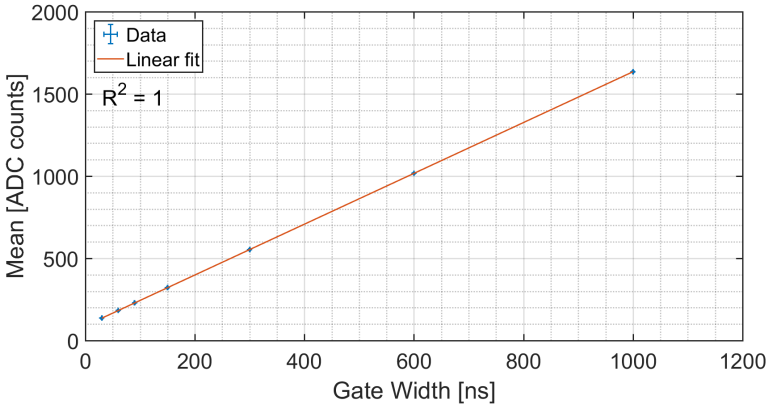

Figure D.13: Dependence of the noise mean value on the gate width for one channel of QDC 3 in low range.

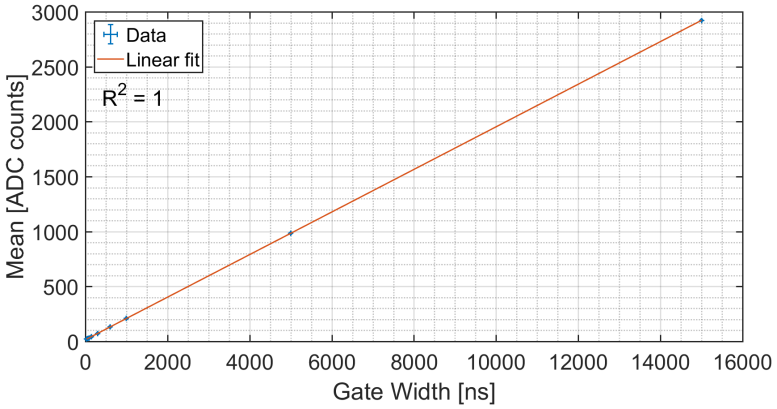

Figure D.14: Dependence of the noise mean value on the gate width for one channel of QDC 3 in high range.

QDC 4

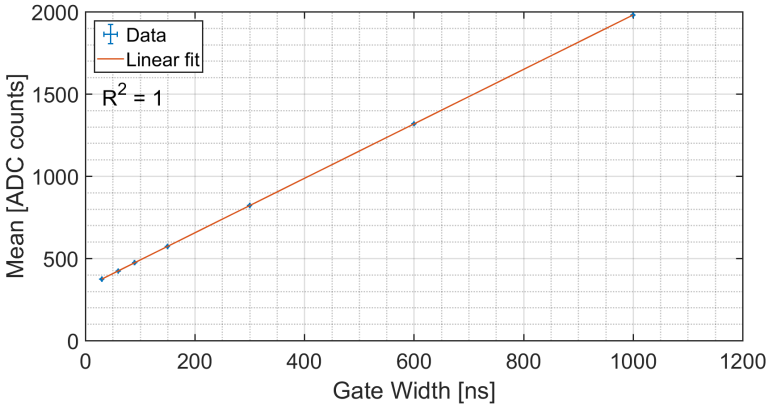

Figure D.15: Dependence of the noise mean value on the gate width for one channel of QDC 4 in low range.

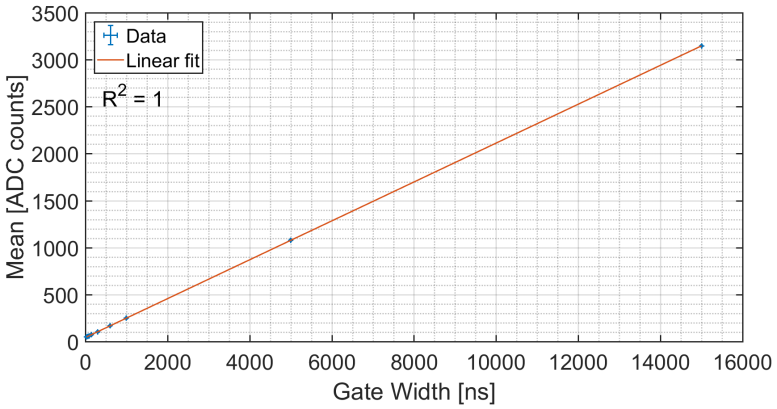

Figure D.16: Dependence of the noise mean value on the gate width for one channel of QDC 4 in high range.

Noise Spread

The spread of the acquired noise was determined with a Gaussian fit. The standard deviation of the Gaussian distribution in dependence on the gate width for one QDC channel in low and high range is displayed. QDC channel 2 was chosen for the low range and QDC channel 3 for the high range channel. Both channels correspond to the same QDC input. For QDC 1, higher values in low and high range can be seen (Figure D.17 and Figure D.18 respectively). A slight increase in the spread for larger gate width can be observed for all QDCs. The typical RMS noise value stated in the CAEN user manual is 0.7 counts for the low range and 1.5 counts for the high range.

QDC 1

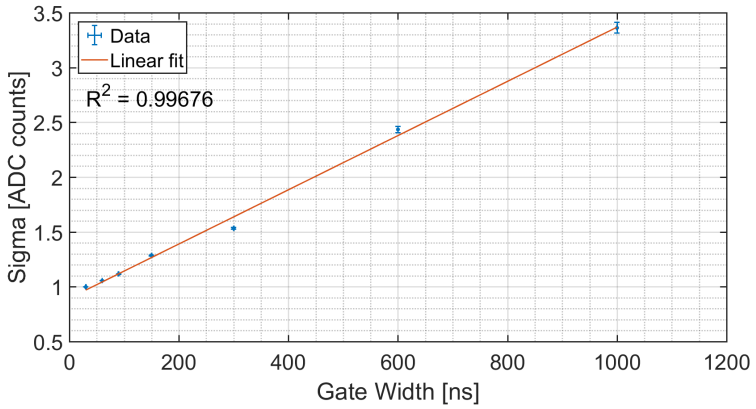

Figure D.17: Dependence of the noise sigma value on the gate width for one channel of QDC 1 in low range.

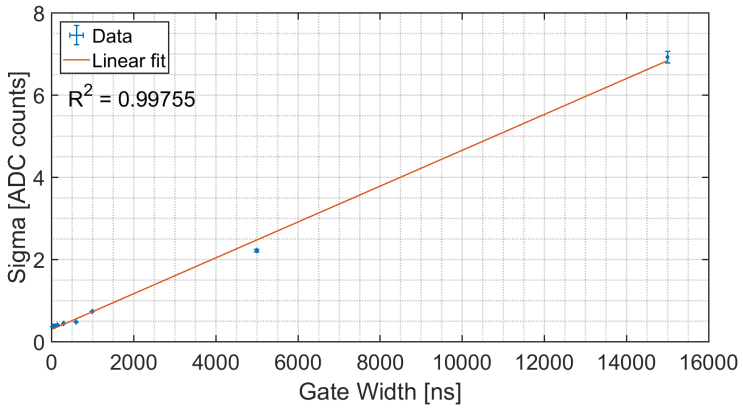

Figure D.18: Dependence of the noise sigma value on the gate width for one channel of QDC 1 in high range.

QDC 2

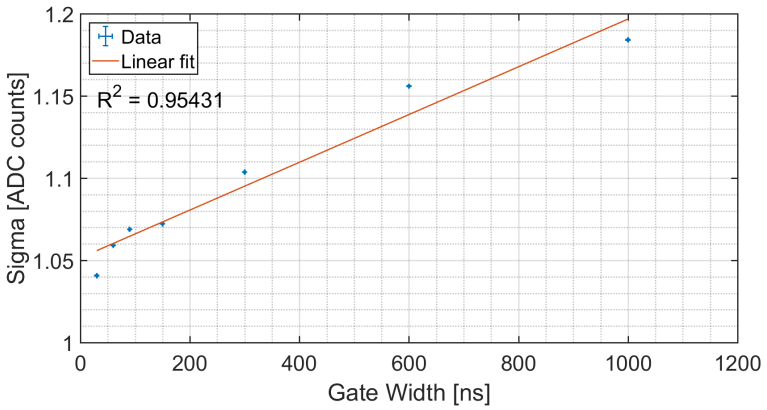

Figure D.19: Dependence of the noise sigma value on the gate width for one channel of QDC 2 in low range.

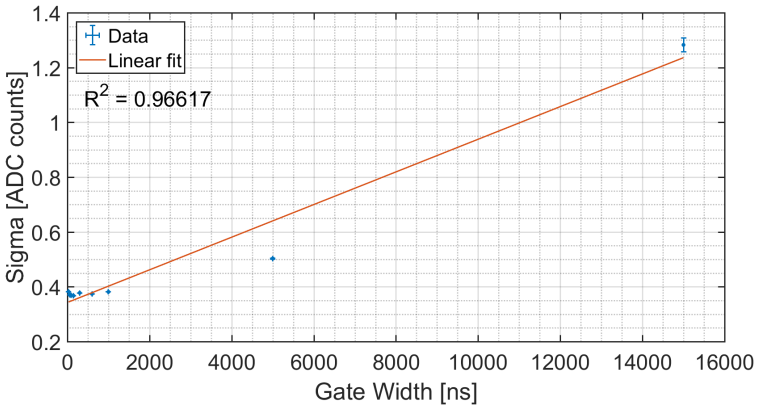

Figure D.20: Dependence of the noise sigma value on the gate width for one channel of QDC 2 in high range.

QDC 3

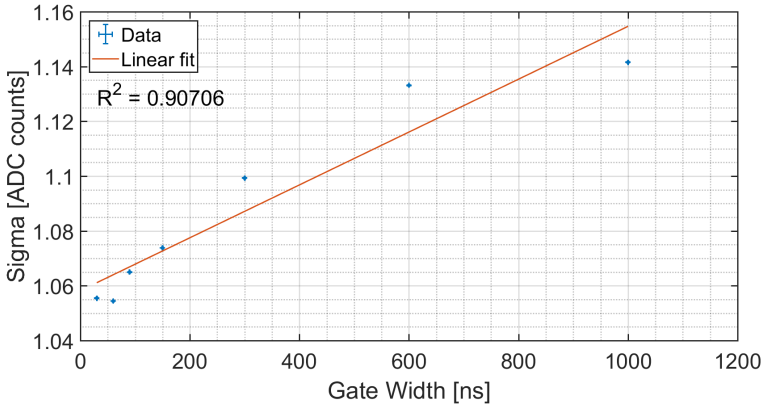

Figure D.21: Dependence of the noise sigma value on the gate width for one channel of QDC 3 in low range.

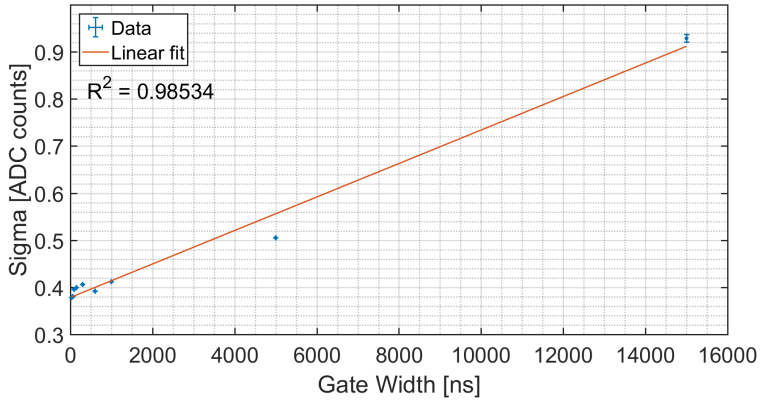

Figure D.22: Dependence of the noise sigma value on the gate width for one channel of QDC 3 in high range.

QDC 4

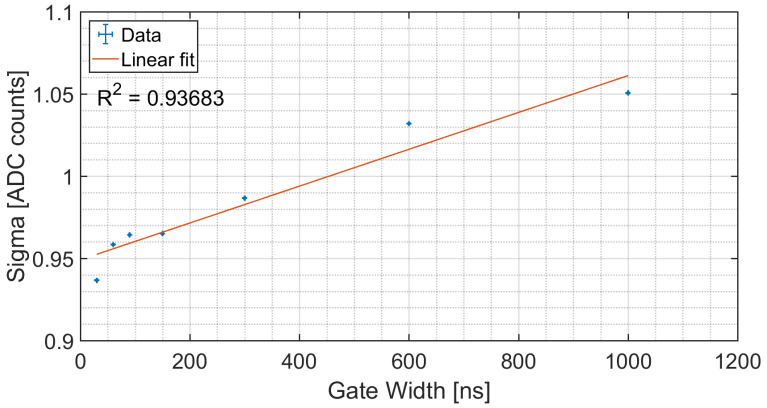

Figure D.23: Dependence of the noise sigma value on the gate width for one channel of QDC 4 in low range.

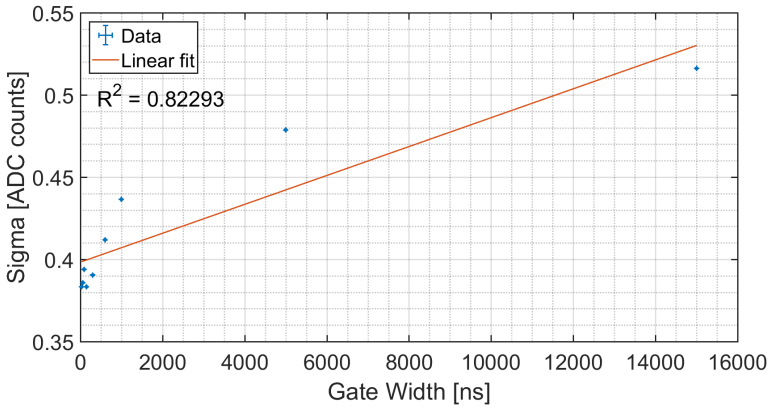

Figure D.24: Dependence of the noise sigma value on the gate width for one channel of QDC 4 in high range.

Appendix E

Printed Circuit Board Layout

CAM350/DFMSTREAM V 12.2 : Mon Nov 12 12:42:56 2018 - 12561-00.cam : 12561-00POS1.ger

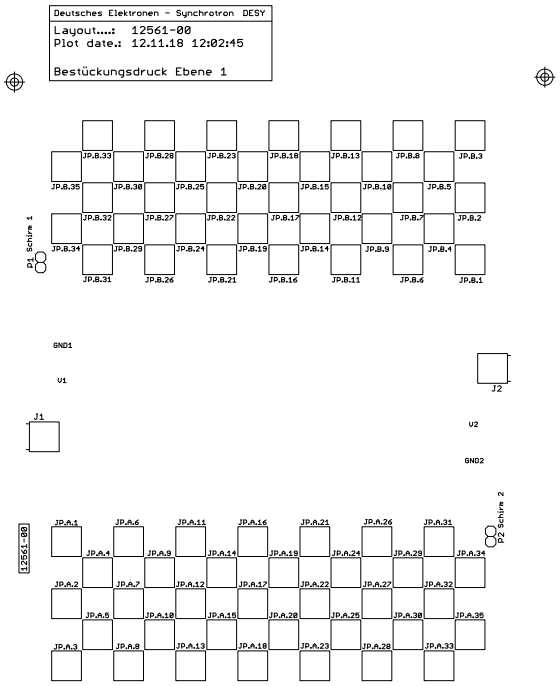

CAM350/DFMSTREAM V 12.2 : Mon Nov 12 12:42:56 2018 - 12561-00.cam : 12561-00LSM1.ger

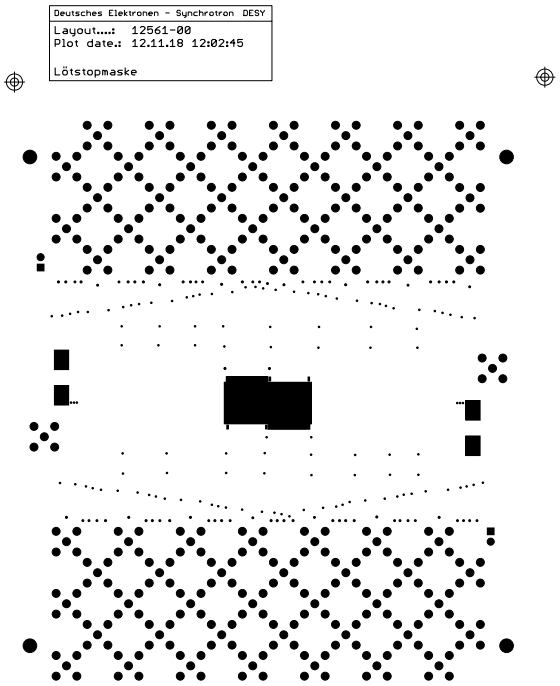

CAM350/DFMSTREAM V 12.2 : Mon Nov 12 12:42:56 2018 - 12561-00.cam : 12561-00L01T.ger

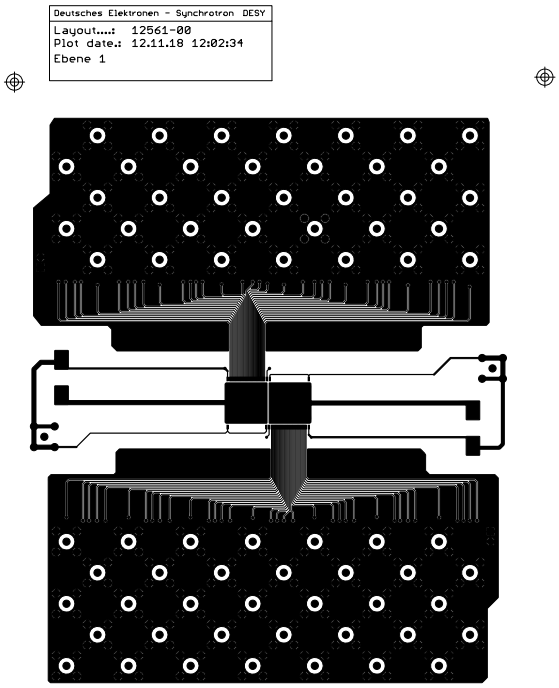

CAM350/DFMSTREAM V 12.2 : Mon Nov 12 12:42:56 2018 - 12561-00.cam : 12561-00L02B.ger

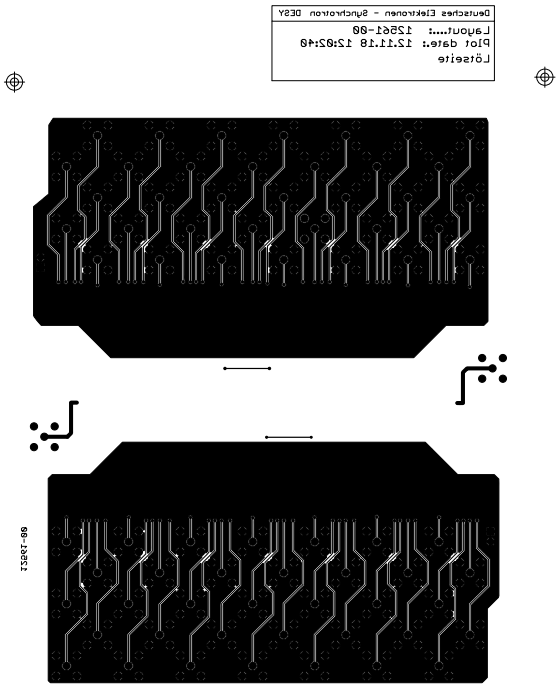

CAM350/DFMSTREAM V 12.2 : Mon Nov 12 12:42:57 2018 - 12561-00.cam : 12561-00LSM2.ger

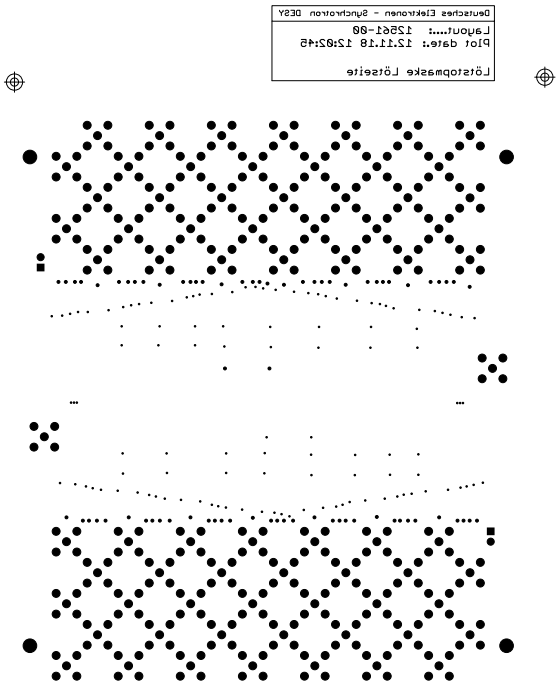

CAM350/DFMSTREAM V 12.2 : Mon Nov 12 12:42:57 2018 - 12561-00.cam : 12561-00Bohr.ger

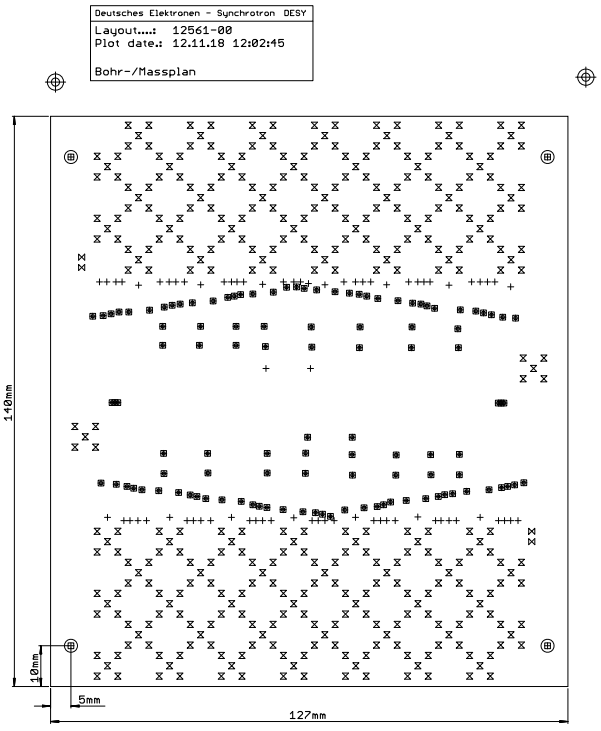

Drill/Bohr Plan					
No.	Sym	Size	Anzahl	DK	NDK
1	⊞	0.20 mm	112	112	0
2	+	0.30 mm	72	72	0
3	⧖	0.80 mm	360	360	0
4	⋈	0.90 mm	4	4	0
5	⊞	3.20 mm	4	0	4
		TOTAL =	552	548	4

Eidesstattliche Erklärung

Ich versichere, dass ich die beigefügte schriftliche Masterarbeit selbstständig angefertigt und keine anderen als die angegebenen Hilfsmittel benutzt habe. Alle Stellen, die dem Wortlaut oder dem Sinn nach anderen Werken entnommen sind, habe ich in jedem einzelnen Fall unter genauer Angabe der Quelle deutlich als Entlehnung kenntlich gemacht. Dies gilt auch für alle Informationen, die dem Internet oder anderer elektronischer Datensammlungen entnommen wurden. Ich erkläre ferner, dass die von mir angefertigte Masterarbeit in gleicher oder ähnlicher Fassung noch nicht Bestandteil einer Studien- oder Prüfungsleistung im Rahmen meines Studiums war. Die von mir eingereichte schriftliche Fassung entspricht jener auf dem elektronischen Speichermedium.

Ich bin damit einverstanden, dass die Masterarbeit veröffentlicht wird.

Ort, Datum	Unterschrift